

Efficient FEM solver for quasi-Newtonian flow  
problems with application to granular materials

Dissertation

zur Erlangung des akademischen Grades eines

Doktors der Naturwissenschaften

(Dr. rer. nat.)

Der Fakultät für Mathematik der  
Technischen Universität Dortmund

vorgelegt von

Saptarshi Mandal

im Dezember 2016

## **Dissertation**

Efficient FEM solver for quasi-Newtonian flow problems with application  
to granular materials

Fakultät für Mathematik  
Technische Universität Dortmund

Erstgutachter: Prof. Dr. Stefan Turek  
Zweitgutachter: Prof. Dr. Thomas Richter

Tag der mündlichen Prüfung: 04.07.2017

Printed with support from the German Academic Exchange Service

# Abstract

This thesis is concerned with new numerical and algorithmic tools for flows with pressure and shear dependent viscosity together with the necessary background of the generalized Navier-Stokes equations.

In general the viscosity of a material can be constant, e.g. water and this kind of fluid is called as Newtonian fluid. However the flow can be complicated for quasi-Newtonian fluid, where the viscosity can depend on some physical quantity. For example, the viscosity of Bingham fluid is a function of the shear rate. Moreover even further complications can arise when the dependencies of both shear rate and pressure occur for the viscosity as in the case of the granular materials, e.g. Poliquen model. The Navier-Stokes equations in primitive variables (velocity-pressure) are regarded as the privilege answer to incorporate these phenomena. The modification of the viscous stresses leads to generalized Navier-Stokes equations extending the range of their validity to such flow.

The resulting equations are mathematically more complex than the Navier-Stokes equations and several problems arise from the numerical point of view. Firstly, the difficulty of approximating incompressible velocity fields and secondly, poor conditioning and possible lack of differentiability of the involved nonlinear functions due to the material laws.

The difficulty related to the approximation of incompressible velocity fields is treated by applying the conforming Stokes element  $Q_2/P_1$  and the lack of differentiability is taken care of by regularization. Then the continuous Newton method as linearization technique is applied and the method consists of working directly on the variational integrals. Next the corresponding continuous Jacobian operators are derived and consequently a convergence rate of the nonlinear iterations independent of the mesh refinement is achieved. This continuous approach is advantageous: Firstly the explicit accessibility of the Jacobian allows a robust method with respect to the starting guess and secondly it avoids the delicate task of choosing the step-length which is required for divided differences approaches.

We denote the full Jacobian matrix on the discrete level by  $A$  and separate it into two parts:  $A_1$  and  $A_2$  corresponding to Fixed point and Newton method respectively. A fundamental issue for the continuous Newton method arises when the problem is not ready for it at the

initial state due to the poor condition of the 'bad-part'  $A_2$  of the Jacobian. Although the Newton method is popular for its local quadratic convergence behavior, however the solver may show unpredictable and undesirable divergent behavior if  $A_2$  is poor conditioned. This particular difficulty is handled by our Adaptive Newton method, where we introduce a characteristic function  $f(Q_n)$ , which depends solely on the relative residual change  $Q_n$  and controls the weighing parameter  $\delta_n$  for the 'bad-part'  $A_2$  resulting in the swinging back and forth of the solver between Fixed point and Newton state.

Finally the new Adaptive Newton method is validated for the Bingham fluid for the benchmark geometry Flow around cylinder and a test case of 2D Couette flow for (modified) Poliquen model having the scope of real world applications is studied to fulfill the objective need of performance.

**Key words:** Finite Element Method, Adaptive Newton Method, Nonlinear Fluids, Bingham Fluid, Granular Materials, Poliquen Model.

*Dedicated to my parents,  
who brought me to this world,  
and were my first Mathematics teachers.*



# Acknowledgements

First and foremost I would like to thank my main supervisor, Prof. Dr. Stefan Turek, for giving me an opportunity to work in Numerical mathematics as a PhD student. I express my sincere gratitude to him for his valuable guidance and persistent support on my work throughout the time of supervision.

I am also incredibly grateful to Dr. Abderrahim Ouazzi and Dr. Hogenrich Damanik for the invaluable discussions and their counselling. My special thanks go to Sven Buijssen and Peter Zajac for their help and consultations in the technical topics. Besides that my utmost gratitude goes to Robert Jendrny and Malte Schuh, especially for proofreading and for their numerous assistance on the countless trivial but important issues. I would also like to acknowledge the help provided by everyone in the LSIII group, from whom I have been directly or indirectly benefited in my research.

I am very much thankful to DAAD for the financial support.

Furthermore I am also very much grateful to all my friends here in Dortmund, who helped it to transform from an unfamiliar city to home for me and for giving me a balanced and enjoyable social life. Finally I would like to thank my family who supported me and showed much patience in quite difficult moments of my life. I hope that I will be able to fully repay their kindness and understanding.

Saptarshi Mandal



# Contents

<b>1</b>	<b>Introduction</b>	<b>1</b>
1.1	Motivation . . . . .	2
1.2	Experimental study . . . . .	4
<b>2</b>	<b>General Overview</b>	<b>7</b>
2.1	Mathematical Challenges . . . . .	8
2.2	Solver Characteristics . . . . .	8
2.3	Thesis structure . . . . .	8
<b>3</b>	<b>Modeling of granular materials</b>	<b>11</b>
3.1	Physical Background . . . . .	11
3.1.1	Mohr Coulomb criterion for friction . . . . .	11
3.1.2	Regimes of powder flow . . . . .	12
3.1.3	Flow rule . . . . .	13
3.2	Discrete model . . . . .	14
3.2.1	Spring-dashpot model . . . . .	14
3.2.2	Discrete element method . . . . .	17
3.3	Model based on Statistical Distribution . . . . .	22
3.3.1	3D granular flows down an inclined surface . . . . .	22
3.3.2	Vibrated powder and molecular analogies . . . . .	25
3.4	Continuous model . . . . .	28
3.5	Mathematical modeling of Granular materials . . . . .	30
3.5.1	Landau Approach . . . . .	30
3.5.2	Schaeffer model . . . . .	31
3.5.3	Tardos model . . . . .	32
3.5.4	Poliquen model . . . . .	33
<b>4</b>	<b>Mathematical Background</b>	<b>37</b>
4.1	Preliminaries . . . . .	37
4.1.1	Sobolev space . . . . .	37
4.1.2	Bilinear form . . . . .	38
4.1.3	Error Analysis . . . . .	39
4.1.4	Weak formulation . . . . .	40
4.1.5	Weak formulation with Deformation tensor . . . . .	41
4.1.6	Problem formulation with Generalized Navier Stokes equation . . . . .	43

4.1.7	Discrete Newton solver . . . . .	43
4.1.8	Continuous Newton solver . . . . .	44
4.2	Discretization aspect . . . . .	46
4.3	The Numerical Solver . . . . .	47
4.3.1	Phase 1 . . . . .	48
4.3.2	Phase 2 . . . . .	49
4.3.3	Phase 3 . . . . .	50
4.3.4	Phase 4 . . . . .	51
4.3.5	Conclusion . . . . .	53
<b>5</b>	<b>Numerical Validation</b>	<b>59</b>
5.1	Flow around cylinder benchmark . . . . .	59
5.1.1	Geometry . . . . .	59
5.1.2	Mesh specification . . . . .	60
5.2	Convergence Statistics . . . . .	61
5.2.1	Newtonian flow . . . . .	61
5.2.2	Shear thinning fluid . . . . .	61
5.2.3	Shear thickening fluid . . . . .	61
5.2.4	Bingham Fluid . . . . .	62
5.2.5	Conclusion . . . . .	62
5.3	Adaptive Newton solver . . . . .	63
<b>6</b>	<b>Application</b>	<b>67</b>
6.1	Geometry . . . . .	67
6.2	Mathematical formulation . . . . .	68
6.2.1	Governing Parameters . . . . .	68
6.2.2	Non-dimensionalization . . . . .	68
6.2.3	Final model . . . . .	69
6.3	Results . . . . .	69
6.3.1	Dortmund results with Umfpack and MG . . . . .	70
6.3.2	Detailed results for multigrid solver . . . . .	70
6.3.3	Freiberg statistics . . . . .	72
6.4	Visual Comparison . . . . .	72
6.4.1	Dortmund results . . . . .	73
6.4.2	Freiberg results . . . . .	75
6.5	Level Comparison . . . . .	77

6.5.1	Statistical Analysis . . . . .	77
6.5.2	Dortmund-Freiberg comparison - Part I . . . . .	79
6.5.3	Dortmund-Freiberg comparison - Part II . . . . .	81
6.6	Choice of the Regularization parameter . . . . .	83
6.6.1	Initial Study . . . . .	83
6.6.2	Detailed Study . . . . .	84
6.6.3	Visual Analysis . . . . .	84
<b>7</b>	<b>Summary and Outlook</b>	<b>89</b>
<b>8</b>	<b>Appendix</b>	<b>93</b>
8.1	Improvement of $f(Q_n)$ . . . . .	93
8.1.1	Stagnation . . . . .	93
8.1.2	Infinite Loop . . . . .	95
8.1.3	Conclusion . . . . .	96
8.2	Boundary conditions . . . . .	97
8.2.1	Wall boundary conditions . . . . .	97
8.2.2	Outflow boundary conditions . . . . .	97



# 1 Introduction

Dense granular materials are universal in nature and some common examples of this kind of materials in our daily lives are sand, rice, sugar etc. A granular media can flow like a liquid, e.g. in an hourglass, or can be transported by the wind to create dunes in the desert. Research in this area is motivated by numerous applications encountered in industrial processes, such as hopper discharge, chute flow, moving beds, sandpipe flow, etc. and also in geophysics for the description and prediction of natural hazards like landslide and rock avalanches. Depending upon the way it is handled, a granular material can behave like a solid, liquid or gas (Fig. 1).



**Figure 1:** Different behaviour of granular materials

Grains can sustain stresses and create a static pile, but can also flow like a liquid in an hourglass, or can create a gas when they are strongly agitated and sometimes these different flow regimes can coexist in a single configuration. The dynamics of granular materials under shear stresses draw a significant attention due to its applications in various technological fields. Some researchers model the phenomenon as the stress is dependent on the strain rate, while some others focus on the rate-independent response. The granular materials are treated as rigid under increasing load until the shear stress exceeds a certain threshold, and then it undergoes a transition from a solid state to a fluidized state (yield) as in Fig. 2. The physical properties and mechanisms of this transition are still not completely understood and sometimes the material remains in a multiphase state. In general, a granular medium is a collection of macroscopic particles of size varying from  $1 \mu\text{m}$  to  $100 \mu\text{m}$ . The limitation in size corresponds to a limitation in the type of interaction between

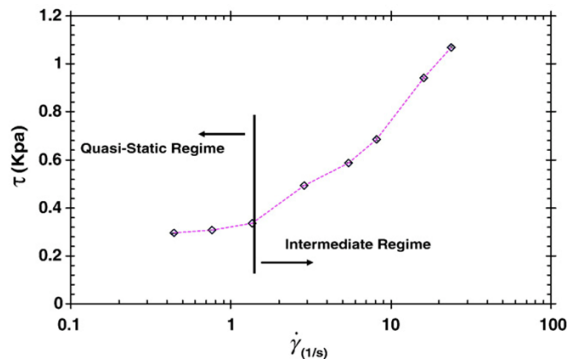


**Figure 2:** Regimes of granular materials

particles, i.e. granular materials of different size exhibit different kind of interaction forces. For example, larger particles are nonbrownian particles which interact solely by friction and collision, whereas in the case of smaller particles other forces like van-der-Waals forces are also present and even smaller size particles interact through thermal agitation.

## 1.1 Motivation

We can find numerous number of materials in our surrounding, which exhibits both the properties of solids and fluids and often termed as 'soft matter'. It is a subfield of condensed matter comprising a variety of physical states that are easily deformed by thermal stresses or thermal fluctuations. The very common examples of this kind of materials are colloids, polymers, foams, gels, granular materials and a number of biological materials. They exhibit an important common feature in that predominant physical behaviors occur at an energy scale comparable with room temperature thermal energy. From the stated examples of this kind of materials, it can be easily understood that soft matters are important in a wide range of technological applications. They may appear as detergents and cosmetics, rubbers in tires, food additives, paints, foams and adhesives, etc. Also one can find the applications of this soft matter in the fields ranging from blood particles to soil mechanics or the mechanism for landing on an extraterrestrial object. In a nutshell, as this soft matter topic is quite new and there still exists a large number of unexplained physical behaviors, this makes the consequent applications to be extremely useful and important.

Some behaviors of soft matter are very interesting, but sometimes it is very difficult to predict such interesting behaviours directly from its atomic or molecular constituents. This is often because soft matter self-organizes into mesoscopic physical structures that are much larger than the microscopic scale, and yet are much smaller than the macroscopic scale of the material. The properties and interactions of these mesoscopic structures may determine the macroscopic behavior of the material. If we take the example of gel or paste, one can observe its fluidic behaviour when it is in large quantity, while it behaves like a solid material when it comes in small quantities. Also in the case of granular materials or powders, sometimes they can jam when the flow is about to stop and unjam just before the flow starts. This jamming part is often regarded as the solid (or static) phase and the part in the motion is considered as the fluid (or dynamic) phase. The static phase is often characterized by a high degree of disorder, inhomogeneity and anisotropy, while the dynamic phase is frequently dominated by dissipative interaction forces leading to a dissipation time scale that interacts with other time scales in the system. So as it lies in the border of fluid and solid regimes, one can simulate the behaviours

of this kind of materials either from a discrete particle point of view or continuum approach. However, flowing of granular materials brings a new challenging and interesting problem to the Computational Fluid Dynamics (CFD) community: At very high concentrations and low rate of strain, a frictional stress model must be taken into account as the grains are in permanent contact. This can be done using plasticity theory in which one assumes that the material behaviour does not depend on the velocity gradient or the strain-rate. However it is in contrast to viscous Newtonian flow where stress specifically depends on the strain-rate. Furthermore, as the flowing materials do not exhibit viscosity unlike fluids, that is why a Newtonian rheology cannot describe granular flow accurately. It is assumed that the material is incompressible, cohesionless and perfectly rigid-plastic. Based on continuum theories, equations for such material have been derived which closely resemble the generalized Navier-Stokes equations where the viscosity is dependent on the pressure and shear forces or stresses. Moreover the software package Featflow [32] is designed for the continuum point of view and hence we will do the simulation of Granular materials from the continuum side and after that, we will study its macroscopic physical properties.

Many different approaches have been taken to simulate this kind of material over the past few decades. The simulation techniques can be categorized broadly into two major approaches - discrete models and continuum models. Usually the granular media are composed of a large number of particles, e.g. a cup of sugar contains around two million of grains, which is a big challenge to simulate with ideal spherical particles. That is why a continuum description is needed to simulate a system of granular media which has a relevant size to the real world. In this model, we define the averaged quantities and model the granular media as a continuum medium. If one considers gases or liquids, the presence of thermal agitation allows a proper statistical approach, by which macroscopic quantities can be derived from the microscopic ones. Sometimes the particles are too large to experience Brownian motion and the statistical average over different configurations is not possible. The system is stuck in metastable states and then it is often termed as athermal system. Another difficulty in applying statistical physics in granular media is the dissipative nature of the particle interaction. Contact interactions including friction and inelastic collisions are highly nonlinear and dissipative in nature and this dissipation at the microscopic level is an important distinction to the classical systems studied in statistical physics.

## 1.2 Experimental study

A schematic representation of a Couette device is shown in Fig. 3 with details of the sensors and the rotating cylinder. The vertical shear gap forms between the rotating cylinder and the outer wall and both its width and height can be adjusted by appropriate choice of the radius and height of the rotating cylinder. The walls of the Couette are made rough by gluing sand paper on the shearing surfaces and the roughness of the walls is chosen to match or exceed the coefficient of

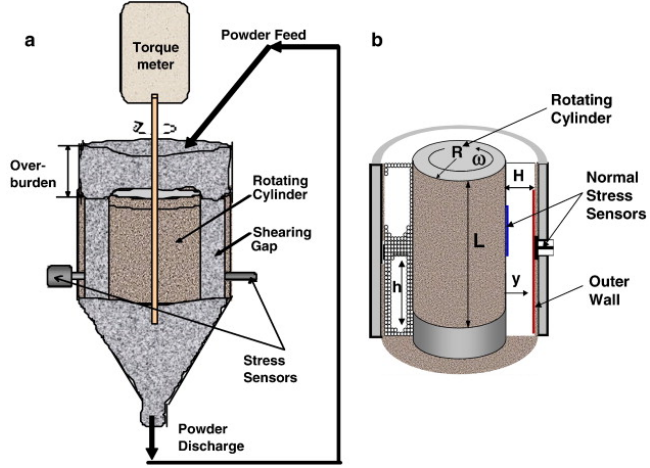


**Figure 3:** Schematic diagram of a Couette device

internal friction of the material thereby trying to assure a non-slip boundary condition. The Couette device can be operated in batch mode or in continuous mode by feeding and removing material to achieve a steady state vertical flow. The material above the rotating cylinder (denoted overburden in the figure) is stationary and only provides dead weight to the shearing layer. Experiments in the Couette device can be performed without (batch) and with axial flow (continuous), and several depths of overburdens to control the pressure in the shearing gap. Normal stresses were measured on both the outer, stationary wall as well as the inner, rotating (shearing) wall of the device as shown in the figure. Shear stresses were measured indirectly and recalculated from the torque on the rotating cylinder.

The shear stress on the rotating cylinder can be measured indirectly using the torque on the shaft exerted by the granular medium on the entire length of the cylinder. The most interesting result from the measurements is that one can calculate the ratio of the average shear to normal stresses as a function of shear rate. The normal stress shows a very interesting behavior: It is constant and lower at low shear rates (where the shear stress is

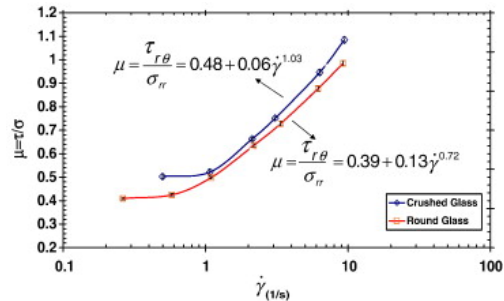


**Figure 4:** Experimental finding

also constant) and then increases abruptly and remains practically constant thereafter even though the shear stress increases continuously. The ratio of the two stresses (apparent friction coefficient) is given in Fig. 4 and the ratio exhibits a similarly interesting behavior: At very low shear rates, the ratio is constant and only slightly lower than the tangent of the friction coefficient of glass particles (about 0.5) as one would expect from quasi-static flow theory. As the dimensionless shear rate increases beyond a certain critical value, the ratio of shear stress vs. normal stress increases significantly. This behavior is mainly due to the superposition of collisions between particles on the sliding friction of surfaces so that the overall shear stress and friction coefficient also increase. Numerical simulations can also be done for different granular materials (crushed glass, round glass etc) as shown in Fig. 5 to study the respective characteristic curves (see [3]).

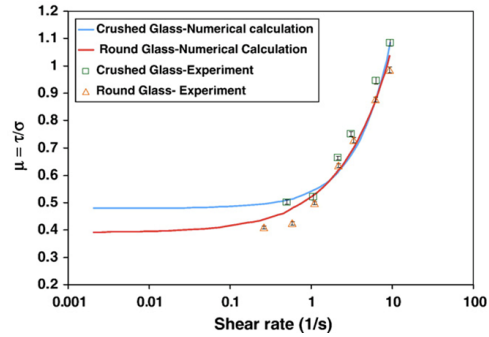


**Figure 5:** Characteristic curves



## 2 General Overview

Fluid, in many cases, is part of our life. Our body consists of 80% of fluids, a tiny single cell of plankton consists of fluids, the earth and the atmosphere consist of a large area of fluids. Fluid is everywhere and becomes a very important element in all human aspects. Thus, it is not only interesting but also very important to explore fluid with experiments, modelling and simulations. This study focuses on the simulation part of fluids and bases on FEM (Finite Element Method). Water is one of the simple fluids which is classified as Newtonian fluid where its stress depends linearly on the deformation rate. Polymer, on the other hand, is classified as non-Newtonian fluids because its stress depends nonlinearly on the deformation rate. The essence of any fluids is that the basic fluid motion is always described by a sound mathematical foundation. This is well-known as the Navier-Stokes equation which serves as the basis of many CFD applications.

Physically, the fluid is considered Newtonian when its viscosity is constant, whereas it is called quasi-Newtonian when the viscosity is a function of other physical parameters. For example, the viscosity is dependant on the shear rate for Bingham fluid and it is dependant on both shear rate and the pressure for granular materials. The flow of Newtonian fluids is categorized by the non dimensional Reynold number,  $Re$ , which tells us whether the flow is laminar, transient, or turbulent. The extreme development of computer resources in the last 10 years provides a wider possibility towards FEM methods which was hardly done 20 years ago. This is also driven by the fact that many CFD solvers used an operator splitting approach together with a low order finite element implementation which is in fact very efficient but needs an extra care when it comes into accuracy of the solution. To the contrary, the high order finite element Q2 towards fully coupled monolithic approach maintains highly accurate solutions. This element together with discontinuous P1 element for the pressure space approximation satisfies the well-known LBB (named after Ladyzhenskaya, Babuska and Brezzi) condition and is, without doubt from years of experiences, one of the preferable finite element pairs in the Stokes problem [22], [23], [24]. An example of benchmark flow around cylinder [32] shows that this element pair can obtain an accurate direct steady solution for medium  $Re$  numbers within few Newton steps.

## 2.1 Mathematical Challenges

The main mathematical problems of the generalized incompressible continuum material model can be summarized as follows.

- **Mathematical analysis:** There is a lack of research concerning the characteristics and properties of solutions for the flow of non-Newtonian fluids.
- **Singular viscosity:** The part of the stress tensor containing  $(1/|\dot{\gamma}|)$  is well defined only for nonzero values of the rate of strain tensor and for 'non-negative' pressures, which requires some regularization techniques of singular phenomena due to the nonlinear viscosity.
- **Discretization method:** It is well known that the computation of solutions to such incompressible systems requires that some care is taken in the choice of the approximating spaces in order to make the discrete problem well posed.
- **Newton multigrid solver:** For this highly nonlinear problem, coupling the pressure and the velocity, linearization using Newton's techniques is an advantageous technique and therefore efficient multigrid methods for these new types of saddle-point problems need to be developed.

## 2.2 Solver Characteristics

The Solution method to the discrete nonlinear system arising from the discretization follows Newton iteration and this technique is well accepted as the most robust iteration technique due to its quadratic convergence. The Jacobian is computed analytically by Frechet-derivative at the continuous level and the complete Jacobian  $A$  in the Saddle point problem can be thought of a combination of two operators  $A_1$  and  $A_2$  which corresponds to Fixed point and full Newton method separately. We also introduce a parameter  $\delta_n$  balancing the Fixed point and full Newton iteration. However the study shows that over-contribution from the operator  $A_2$  can be harmful for the convergence behavior sometimes and hence the value of  $\delta_n$  should be remained under control. So essentially new in this study is the implementation of  $\delta_n$  and to provide an adaptive way to control this parameter to have a balance between the Fixed point and full Newton method. Since this is also an extension of the 2D Navier-Stokes solver that is used in our chair, step by step validation through benchmarking is also part of the study.

## 2.3 Thesis structure

This thesis is structured as follows: The first two chapters have been used for the introduction to the granular materials and why it is important to study them. After giving a general

overview in the current chapter, we will present different approaches to study granular materials, namely Discrete models, Statistical approaches and Continuous models in chapter 3. The most emphasized continuous model, Poliquen model will also be introduced and discussed in detail in this chapter. Next we will present the mathematical background including Weak formulation, Error analysis, the classical Newton solver and the new Adaptive Newton solver in chapter 4. Then in chapter 5, step-by-step validation of the code with respect to the Flow around cylinder problem will be done. Then a prototype application for the Couette geometry will be examined in Chapter 6 and the results of the convergence behavior will be represented alongwith visual support. Ultimately the study will be completed by summarizing and giving an outlook for future research and additionally some extra results is appended in the Appendix section 8.



### 3 Modeling of granular materials

In this chapter, we will describe some mathematical models for granular media with different kind of approaches. We denote the physical properties as follows: We take a finite system of granular materials where each particle has mass  $m_i$  and velocity  $v_i$ . For simplicity of calculations we will assume that each particle is of spherical shape with radius  $R_i$  with the position vector  $r_i$ . Any pair of two particles  $P_i$  and  $P_j$  will have atmost one contact point with  $F_{ij}$  being the contact force,  $n_{ij}$  being the normal unit vector and  $t_{ij}$  being the unit vector in the tangential plane. There are total  $N$  number of particles in the system and the whole system has the volume  $V$ . In case of a system of homogeneous particles, we assume the diameter of each particle as  $d$ . We denote the volume fraction as  $\varphi$  and the total number of contacts as  $N_c$ . Macroscopically  $\rho$  is the density,  $\rho_s$  is the gross density and  $\eta$  is the viscosity of the system. We also define  $p$  as the pressure and  $u$  as the velocity at any given point in the system. The stress tensor, the stress deviator tensor and the shear strain are denoted by  $T$ ,  $\sigma$ , and  $\gamma$ , whereas the normal stress and the shear stress on a particular plane are denoted by  $\sigma_n$  and  $\tau$ . We also denote two important physical properties corresponding to the modeling of granular materials -  $\mu(I)$  as the friction coefficient and  $I$  as the inertial number.

#### 3.1 Physical Background

##### 3.1.1 Mohr Coulomb criterion for friction

The Mohr theory suggests that the shear stress on a failure reaches some unique function of normal stress,  $\tau = f(\sigma)$ , where  $\tau$  is the shear stress and  $\sigma$  is the normal stress. Coulomb found that for frictional motion the yield shear stress can be expressed as a combination of a normal stress dependent component and a stress independent component. While the normal stress dependent component is connected with the internal angle of friction  $\phi$ , the former seems to be related to the intrinsic cohesion and is denoted by the symbol  $c$ . Then, the Coulomb equation reads:

$$\tau = \sigma \tan \phi + c, \quad (3.1)$$

where  $\phi$  and  $c$  are the material constants defined as the angle of internal friction and the cohesive strength respectively: A material is called non-cohesive if  $c = 0$ . Eq. 3.1 represents the simple law of friction of two solids sliding on each other with the shear force proportional to the normal force where  $\mu = \tan \phi$  is the friction coefficient. A similar condition also exists at the interface between the granular material and the walls of the container: Here only the angle

of internal friction is replaced by the angle of wall friction  $\phi_W$ . The angle satisfies  $\phi_W < \phi$  since the wall is usually less rough than a powder layer which is mainly due to the void fraction near the wall.

### 3.1.2 Regimes of powder flow

Similar to fluid flow, where several characteristic numbers, like Froude number, Reynolds number, etc. can be used to characterize the qualitative flow behavior, the various powder regimes can be represented as a function of a dimensionless shear rate  $\gamma^{o*} = \gamma^o [d_p/g]^{1/2}$  which contains a gravitational term  $g$  and a particle size  $d_p$ . Based on such a characterization, one has the following three different regimes.

- **Quasi-static regime:** This regime is valid when the flow is slow enough so that any movement between two static states can be neglected. In this case the static equilibrium equation can be applied. With this approach only stress and condition of the onset of flow can be computed, while no flow field can be predicted which circumscribes the range of applications of this approach. There is a large number of analytical and numerical solutions to this case and an important number of literature devoted to this regime, see for instance [14],[16].
- **Slow and frictional regime:** In this regime the frictional forces between particles are predominant, so the inertial effect is added to the static equations as well as the consideration of continuity beside a yield condition. The first model invoking a flow rule was introduced by Schaeffer (1987) [17]. This regime is very important since it can be used for modeling a wide range of practical phenomena and industrial applications. However, for the serious challenges which arise in this regime, for instance ill-posed partial differential equations and the prediction of stress fluctuations, there is still a lack of fundamental research so that dealing with these problems requires a multidisciplinary treatment. Our contribution has the goal of supporting this part by modern numerical methods which will be described in the subsequent sections.
- **Intermediate and rapid granular regimes:** For the intermediate regime, in addition to inter-particle friction energy, collision energy is also important. For the rapid regime, the short particle-particle contacts are important while frictional forces are neglected and this regime is often described via kinetic models (see [18] for more details).

### 3.1.3 Flow rule

- **Venant Principle:** The Saint Venant principle of solid mechanics says that stresses cause deformations preferentially in the same direction. This leads to the co-axiality flow rule condition which states that the principal directions of the stress and rate of deformation are parallel and neglects the rotation of a material element during deformation. In two-dimensional Cartesian coordinates, this condition takes the form, for example:

$$\frac{T_{ii} - T_{jj}}{T_{ij}} = \frac{2(\frac{\partial u_1}{\partial x} - \frac{\partial u_2}{\partial y})}{\frac{\partial u_1}{\partial x} + \frac{\partial u_2}{\partial y}} .$$

This was postulated by Schaeffer [17] for the deformation of granular material. However, since the deformation of the granular material requires that the stresses in different directions must be different, Schaeffer claimed that "the response of the material to such unequal stresses should be to contract in the directions of greater stress and to expand in the directions of smaller stress". This reflects the requirement that the eigenvectors of stress tensor and strain rate are aligned and it quantitatively links the deviatoric stress and the strain rate tensor by the formula  $\sigma = \lambda \dot{\gamma}$ .

- **Plastic deformation:** The deformation of a granular material is considered to be plastic in the sense that, if after deformation the shearing stress is reduced, the material would not show any tendency to return to its original state. Plastic deformation was already proposed by E. C. Bingham, in 1922, in the context of non-Newtonian fluids, and in which the rheological behavior is governed by the following equation in modified state introduced by Oldroyd:

$$T = -pI + \left( \frac{\mu_0}{\|\dot{\gamma}\|} + \mu \right) \dot{\gamma} \quad (\mu_0 > 0, \mu > 0) .$$

- **Dilatancy:** A simple manifestation of this phenomenon occurs when one leaves dry footprints while walking along a wet beach: The deformed sand dilates, therefore space between grains increases, allowing for upper water to invade the sand. As a consequence, footsteps get dry and water goes down. This is the phenomenon of dilatancy which was explained by Reynolds in 1885, and demonstrated experimentally: A glass tube attached to a balloon showed that the amount of excess water decreased when the sand was deformed, thus showing that deformation increases the space between grains. Dilatancy is important in the dynamics of granular material, introducing a stick-slip instability at low velocity (see [19]), and it occurs because each grain needs more space in the flowing

state than at rest. Then, the flow theory of plasticity must be applied to the constitutive modeling for describing the deformation process of a granular material.

## 3.2 Discrete model

### 3.2.1 Spring-dashpot model

Here we assume that the inertial effects associated with the individual particle interactions are negligible in this model and the stress is largely independent of deformation rate. We take all the particles to be spherical and they interact via contact forces. Two spherical particles with position vectors  $r_i, r_j$  and radii  $R_i, R_j$  experience a force

$$F_{ij} = F_{n_{ij}} + F_{t_{ij}},$$

when  $\delta_{ij} = R_i + R_j - |r_i - r_j| > 0$ ,

where  $n_{ij} = \frac{r_i - r_j}{|r_i - r_j|}$  is the normal unit vector

and  $t_{ij}$  is a unit vector in the tangential plane.

The normal and tangential components of the interaction force acting on a particle  $i$  for the Hookean contact model are:

$$F_{n_{ij}} = k_n \delta_{ij} n_{ij} - \gamma_n m^* v_{n_{ij}},$$

$$F_{t_{ij}} = -k_t v_{t_{ij}} - \gamma_t m^* v_{t_{ij}},$$

where  $k_{n,t}$  and  $\gamma_{n,t}$  are the spring elastic and the viscous damping constants,  $v_{n_{ij}}$  and  $v_{t_{ij}}$  are the normal and tangential component of particle relative velocity and  $m^* = m_i m_j / (m_i + m_j)$  is the effective mass of the two particle system satisfying  $F_{ji} = -F_{ij}$ . The tangential force can be computed from the elastic shear displacement,  $v_{t_{ij}}$  and its rate is given by:

$$\frac{dv_{t_{ij}}}{dt} = v_{t_{ij}} - \frac{(v_{t_{ij}} \cdot v_{ij}) r_{ij}}{r_{ij}^2}.$$

The last term arises from the rigid-body rotation around the contact point and ensures that  $v_{t_{ij}}$  always lies in the local tangent plane of contact. As the shear displacement increases, the tangential force reaches the limit imposed by a static yield criterion,  $|F_{t_{ij}}| \leq \mu' |F_{n_{ij}}|$ , characterized by a local particle friction coefficient,  $\mu'$ . The tangential force is then set to the limit value by truncating the magnitude of  $v_{t_{ij}}$ .

This spring-dashpot model is very similar to the Hertzian model, where the contact forces are defined as:

$$\begin{aligned} F_{nHz_{ij}} &= \sqrt{\delta_{ij} R^*} (k_{nHz} \delta_{ij} n_{ij} - \gamma_n m^* v_{n_{ij}}), \\ F_{tHz_{ij}} &= \sqrt{\delta_{ij} R^*} (-k_{tHz} v_{t_{ij}} - \gamma_t m^* v_{t_{ij}}), \end{aligned}$$

where  $R^* = R_i R_j / (R_i + R_j)$  is the effective radius. The normal and tangential elastic constants in the Hertzian model are related to the particle material properties as:

$$\begin{aligned} k_{nHz} &= \frac{3}{4} E^*, & \text{where } E^* &= \left( \frac{1 - \nu_i^2}{E_i} + \frac{1 - \nu_j^2}{E_j} \right)^{-1} \\ k_{tHz} &= 8G^*, & \text{where } G^* &= \left( \frac{2 - \nu_i}{G_i} + \frac{2 - \nu_j}{G_j} \right)^{-1} \end{aligned}$$

with  $E_{i,j}, \nu_{i,j}$  and  $G_{i,j}$  denoting particle Young's modulus, Poisson ratio and shear modulus respectively. The value of the linear spring elastic constant is chosen to be large enough to minimize particle overlap, yet not so large as to require an unreasonably small simulation time step.

In the Hookean model, we set

$$\begin{aligned} k_t &= \frac{2}{7} k_n, \quad \gamma_t = \frac{1}{2} \gamma_n, \\ e &= \exp\left(-\gamma_n \pi \sqrt{\frac{m^* - \gamma_n^2}{4k_n}}\right) \end{aligned}$$

and  $\gamma_n$  is chosen to yield  $e = 0.7$  for the normal restitution coefficient. The model does not incorporate the effect of gravity and simple shear flow is induced via the Lees-Edwards boundary conditions. The  $x$ -,  $y$ - and  $z$ -directions refer to the flow, neutral (vorticity) and gradient directions respectively. The macroscopic rate of deformation tensor  $\dot{\gamma}_m$  at the steady state is expressed as:

$$\dot{\gamma}_m = \frac{1}{2} \dot{\gamma} (e_{(x)} e_{(z)} + e_{(z)} e_{(x)}),$$

where  $e_{(x)}$  and  $e_{(z)}$  are unit vectors in  $x$  and  $z$  directions and  $\dot{\gamma}$  is the shear rate. Homogeneous stress and strain can be extracted from this type of flows, which facilitates the constitutive

modeling. The macroscopic stress is calculated as:

$$\sigma = \frac{1}{V} \sum_i \left[ \sum_{j \neq i} \frac{1}{2} r_{ij} F_{ij} + m_i (v'_i)(v'_i) \right],$$

where  $v'_i$  is the fluctuating velocity of a particle relative to its mean streaming velocity in the shear flow. The average coordination number is defined as the mean contacts per particle in the contact network,  $Z = 2N_c/N$ , where  $N_c$  is the total number of contacts (with non-zero contact forces) and  $N$  is the total number of particles in the contact network. When the coordination number is equal to a critical value  $Z_c$ , the granular assembly is at an isostatic state and the number of degrees of freedom is matched by the number of constraints between particles. The particles with zero (floaters) or one contact (rattlers) can be neglected as they do not participate in the contact network and  $Z_2$  is used to distinguish from the model where the floaters and rattlers are not neglected. The unit contact normal vector pointing from centre to centre of two spherical particles in contact is denoted by  $n$  and the fabric tensor is defined as the symmetric traceless second rank tensor

$$A = \frac{1}{N_c} \sum_{\alpha=1}^{N_c} n^\alpha n^\alpha - \frac{1}{3} I_3,$$

where  $I_3$  is the three dimensional unit tensor. The structural anisotropy can be easily related to the shear component of the fabric tensor  $A_{xz}$ . Next we demonstrate a simple model which can capture the dynamic shear results for the microstructural quantities. We define:

$$\begin{aligned} \dot{\gamma}_{md} &= \dot{\gamma}_m - \frac{1}{3} \text{tr}(\dot{\gamma}_m) I \\ \text{and } \sigma &= pI - p\eta \frac{\dot{\gamma}_{md}}{|\dot{\gamma}_m|}, \end{aligned}$$

where  $\dot{\gamma}_{md}$  is the deviatoric strain rate tensor and  $\eta$  is a scalar macroscopic friction coefficient in the solid regime (equivalent to viscosity in the fluid regime).  $p$  and  $\eta$  are expressed in terms of  $Z_2$  and  $A$  as:

$$\begin{aligned} \frac{pd}{k} &= (a_1 + a_2|A|)(Z_2 - Z_c)^\alpha, \\ \eta &= b_1 + b_2 A : \hat{S}, \end{aligned}$$

where  $a_1$  and  $a_2$  are material parameters and  $\alpha = 2$ . The micromechanical equation involving

elasticity and pressure can be written as:

$$\sigma \approx = \frac{3\phi Z}{2\pi d^3} \bar{r} \left( k_n \bar{\delta}_n \frac{1}{N_c} \sum_i \sum_{j \neq i} nn - k_t \bar{\delta}_t \frac{1}{N_c} \sum_i \sum_{j \neq i} nt \right),$$

where  $\bar{r}$ ,  $\bar{\delta}_n$ ,  $\bar{\delta}_t$  are mean quantities. We define  $W$  as the spin tensor and  $\dot{A}$  denotes its material derivative and the evolution equation for fabric is expressed as:

$$\begin{aligned} W &= \frac{1}{2}(\nabla v - \nabla v^T) \\ A^* &= c_1 S + c_2 |D|A + c_3 (A : S)A \\ &= \dot{A} + A \cdot W + W \cdot A . \end{aligned}$$

### 3.2.2 Discrete element method

The Discrete Element Method (DEM) has been adopted as an analysis tool in many fields dealing with granular matter such as process and pharmaceutical industries [15]. DEM is closely related to Molecular Dynamics (MD) and also called as soft particle Molecular Dynamics sometimes. The principle of both methods can be summarized as finding the trajectories of particles obeying principles of classical mechanics by solving Newton's equation of motion. However as the name suggests, MD is mainly used to study thermodynamic properties of ensembles of atoms and molecules, DEM on the other hand is generally used to simulate the motion of macroscopic particles. Consequently the interactions between particles are usually dissipative in DEM, whereas the forces are conservative i.e. derived from a potential in MD.

If particles are large enough, long range interactions such as van-der-Waals forces are negligible. In this case particles interact only when they are in close contact. At this point they start deforming due to the forces exerted on to each other. In real granular materials particles have complicated shapes and their deformation and forces acting on them can be very complex. To reduce the computational cost, particles are typically modeled as spheres or disks in DEM and it is assumed that they are in contact when they overlap. Furthermore the contact forces are computed as a function of the overlap.

**Micro formulation:** Here first the normal collision of two spherical particles is viewed as the linear spring-dashpot contact force model and the overlap of two particles with diameters  $d_i, d_j$  and position vectors  $r_i, r_j$  is defined as:

$$\delta = \max\left(0, \frac{1}{2}(d_i - d_j) - (r_i - r_j) \cdot n_{ij}\right),$$

where  $n_{ij}$  is the normal unit vector parallel to the line connecting their centers. The relative speed and acceleration can be expressed as:

$$\begin{aligned}\dot{\delta} &= -(v_i - v_j) \cdot n_{ij} = -v_{ij} \cdot n_{ij}, \\ \ddot{\delta} &= -(a_i - a_j) \cdot n_{ij} = -(f_i/m_i - f_j/m_j) \cdot n_{ij} = -\frac{1}{m_{ij}} f_i \cdot n_{ij} = -\frac{f_i}{m_{ij}},\end{aligned}$$

where  $m_{ij} = \frac{m_i m_j}{m_i + m_j}$  is the effective mass and  $f_i = -f_j$  is the contact force acting on the particles. According to the spring-dashpot model:

$$f_i = -m_{ij} \ddot{\delta} = k\delta + \gamma \dot{\delta},$$

where  $k$  is the linear spring constant and  $\gamma$  is the viscous damping coefficient. Regarding this equation and using the following substitutions for the natural frequency  $\omega_0 = \sqrt{k/m_{ij}}$  and the viscous dissipation  $\eta = \frac{\gamma}{2m_{ij}}$ , we obtain the ordinary differential equation of the harmonic oscillator:

$$\omega_0^2 \delta + 2\eta \dot{\delta} + \ddot{\delta} = 0.$$

With the initial condition  $\delta(0) = 0$  and  $\dot{\delta} = \nu_0$ , the solution is given as:

$$\delta(t) = \frac{\nu_0}{\omega} \exp(-\eta t) \sin(\omega t),$$

where  $\omega = \sqrt{\omega_0^2 - \eta^2}$  is the oscillation frequency of the damped system. The duration of a contact can be defined in two ways. The first criterion is expressed by  $\delta(t_c^\delta) = 0$  and then  $t_c$  corresponds to the half-period of the oscillator

$$t_c^\delta = \frac{\pi}{\omega}.$$

Another way is to assume that the contact ends when the force is zero i.e.  $f(t_c^f) = 0$ . Then  $t_c^f$  can be obtained as:

$$t_c^f = \frac{1}{\omega} \left( \pi - \arctan \frac{2\eta\omega}{\omega^2 - \eta^2} \right) .$$

Finally using one of the  $t_c$  described above, we can obtain the restitution coefficient with  $r = -\frac{\nu(t_c)}{\nu_0}$  and this gives  $r = \exp(-\eta t_c^\delta)$  for  $t_c^\delta$ . The contact duration and the coefficient of restitution for the bouncing of a particle on a wall can be computed following the same procedure and assuming  $m_{wall} = \infty$ . Linear elastic and viscous tangential contact forces are modeled in a similar way

$$f^t = -k^t \delta^t - \gamma^t v_{ij}^t,$$

with the spring stiffness  $k^t$ , viscous dissipation  $\gamma^t$  and tangential displacement  $\delta^t$  and the tangential velocity at contact

$$v_{ij}^t = v_{ij} - (v_{ij} \cdot n_{ij})n_{ij} - \Omega_i \times L_{ij} + \Omega_j \times L_{ji},$$

where  $\Omega_j$  is the angular velocity of particle  $i$  and  $L_{ij} = -((d_i - \delta)/2)n_{ij}$  is the branch vector from the center of particle  $i$  to the contact point. The tangential spring length is calculated by integrating

$$\frac{d\delta^t}{dt} = v_{ij}^t - \frac{(\delta^t \cdot n_{ij})n_{ij}}{|r_i - r_j|}$$

starting from the time of contact. The second term is needed to rotate the spring so that it is always perpendicular to the contact normal  $n_{ij}$ .

Contact friction is described by the Coulomb friction model where  $\mu$  is the coefficient of friction which limits the tangential contact forces such that  $|f^t| \leq \mu|f^n|$  with  $f^n$  being the normal contact force. Particles slide past each other if  $|f^t| = \mu|f^n|$  and are stuck otherwise. If  $|f^t| > \mu|f^n|$ , the tangential displacement is adjusted to satisfy Coulomb criterion. After force calculation, the next step of DEM is the integration of the equations of motion and it can be achieved by using any numerical integration scheme:

$$m_i a_i = f_i \text{ and } I_i \frac{d\Omega_i}{dt} = q_i,$$

where  $I_i$  is the moment of inertia and  $f_i$  and  $q_i$  are the total force and torque acting on the particle respectively.

**Micro-Macro transition:** DEM allows a very detailed description of granular materials including contact forces and exact position of the particles. However the amount of data generated during a DEM simulation is huge and in order to compare it to macroscopic experiments or theories, smoothing and averaging are necessary. Here some averaging procedures are presented, which are used to obtain macroscopic tensorial quantities such as the fabric tensor and the stress for granular materials.

- **Averaging formalism**

The general rule to obtain any average quantity  $Q$  in an area  $V$  is defined as:

$$Q = \frac{1}{V} \sum_{p \in V} w_V^p V^p Q^p, \quad (3.2)$$

where  $V^p$  is the volume of the particle and  $w_V^p$  is the weight of the contribution to the average and  $Q^p$  is the pre-averaged particle quantity

$$Q^p = \sum_{c=1}^{C^p} Q^c$$

with  $Q^c$  the local quantity at the contact and  $C^p$  the number of contacts of the particle. The simplest example of averaging is the solid volume fraction of a particle assembly obtained with  $Q^p = 1$ :

$$v = \frac{1}{V} \sum_{p \in V} w_V^p V^p .$$

From this the average density can be easily computed by assigning the weight to the particle densities  $w_V^p = \rho_p$ .

- **Fabric Tensor**

The fabric is a tensorial quantity which is used to characterize the internal structure of an assembly of grains. For a single particle its definition is given as:

$$F^p = \sum_{c=1}^{C^p} n^c \otimes n^c,$$

where  $n^c$  is the unit vector pointing outwards in the direction of the contact. An equivalent definition is given in terms of the branch vectors connecting the center of the particle

to the contact points

$$F^p = \frac{1}{a^2} \sum_{c=1}^{C^p} L^{pc} \otimes L^{pc},$$

where  $a$  is the particle radius assuming that it is spherical. The average fabric is computed as:

$$F = \langle F^p \rangle = \frac{1}{V} \sum_{p \in V} w_V^p V^p \sum_{c=1}^{C^p} n^c \otimes n^c .$$

Note that  $tr(F^p)$  is equal to the number of contacts of the particle  $C^p$ . In a regular lattice arrangement assuming that  $w_V^p = 1/\forall p$ ,  $tr(F)$  is exactly equal to  $Cv$  i.e. the coordination number times the volume fraction.

- **Stress**

The average stress of a body inside a volume  $V$  is defined by:

$$\bar{\sigma} = \frac{1}{V} \int_V \sigma dV .$$

Using the static equilibrium condition  $\nabla \cdot \sigma = 0$  and the divergence theorem it can be shown that:

$$\bar{\sigma} = \frac{1}{V} \int_{\partial V} (x \otimes \sigma) \cdot n dV,$$

where  $x$  is the position vector and  $n$  is the outward normal vector. Therefore the average stress inside a particle which is in contact with other particles can be expressed as:

$$\sigma^p = \frac{1}{V^p} \sum_{c=1}^{C^p} L^{pc} \otimes L^{pc} .$$

Here we have assumed that the contact forces  $f^c$  are equal to point loads such that  $\sigma^c \cdot n = f^c$  where  $\sigma^c$  is the stress tensor at the contact point. Now following the formalism expressed in Eq. 3.2, the average stress tensor in a particle assembly can be written as:

$$\sigma = \langle \sigma^p \rangle = \frac{1}{V} \sum_{p \in V} w_V^p \sum_{c=1}^{C^p} L^c \otimes L^c .$$

If the weights  $w_V^p$  are ignored, the average stress can also be expressed as a sum over all contacts inside the assembly. Since  $f^c = f^{pq} = -f^{qp}$  where  $f^{pq}$  and  $f^{qp}$  are the forces exerted by particles  $q$  and  $p$  on to each other respectively, it is possible to write:

$$\sigma = \frac{1}{V} \sum_{c \in V} L^c \otimes f^c .$$

### 3.3 Model based on Statistical Distribution

#### 3.3.1 3D granular flows down an inclined surface

The macroscopic fields in this model involve density, velocity, granular temperature, as well as strain-rate, stress and fabric tensors. Due to the plane strain flow, each tensor can be expressed in an inherently anisotropic form with only four objective, coordinate frame invariant variables [7]. For example, the stress can be decomposed as

1. the isotropic pressure
2. the anisotropy of the deviatoric stress
3. the anisotropic stress in the principal direction
4. the anisotropic stress in the orientation of its eigensystem

In this model, it is assumed that each particle's mass is located at the center. The particles are soft so that the collisions are not instantaneous, but not too soft so that the contact area can be replaced by a contact point. Furthermore, the particles are convex so that each particle pair has a single point of contact. Flow particles are labeled from 1 to  $N$ , while the boundary particles are labeled from  $N + 1$  to  $N + N_b$ . We take the material to be homogeneous, each particle has mass  $m_i = m$ . From statistical mechanics, the microscopic (point) mass density of the flow,  $\rho^{mic}$ , at a point  $r$  at time  $t$  is defined by:

$$\rho^{mic}(r, t) = \sum_{i=1}^n m \delta(r - r_i(t)),$$

where  $\delta(r)$  is the Dirac-delta distribution. The macroscopic mass density field can be extracted by convoluting the microscopic mass density with a coarse-graining function  $W(r)$  (which can be chosen arbitrarily) yielding

$$\begin{aligned}\rho(r, t) &= \sum_{i=1}^n m \int_{R^3} \delta(r' - r_i(t)) W(r - r') dr' \\ &= \sum_{i=1}^n m W(r - r_i(t)) .\end{aligned}$$

One example of  $W(r)$  can be Lucy function and it has the advantages of producing twice differentiable fields and having compact support:

$$W(r) = \frac{105}{16\pi c^3} \left( -3 \left( \frac{r}{c} \right)^4 + 8 \left( \frac{r}{c} \right)^3 - 6 \left( \frac{r}{c} \right)^2 + 1 \right),$$

for  $r := |r| < c$ , 0 else

with  $c$  being the range and  $w = c/2$  being the half-width, or standard deviation. We define the volume function  $\nu$ , coarse-grained momentum density vector  $j$  and the macroscopic velocity field  $u$  as:

$$\begin{aligned}\nu(r, t) &= \frac{\rho(r, t)}{\rho_p} = \sum_{i=1}^N \mathcal{V} W(r - r_i(t)), \\ j(r, t) &= \sum_{i=1}^N m v_i W(r - r_i(t)), \\ u(r, t) &= \frac{j(r, t)}{\rho(r, t)}\end{aligned}$$

with  $\mathcal{V} = \frac{\pi}{6} d^3$  the particle volume and  $v_i$  the velocity of particle  $i$ . Now the momentum balance equation takes the form:

$$\frac{\partial j}{\partial t} = -\nabla \cdot [\rho u u] - \nabla \cdot \sigma + F_b + \rho g,$$

where  $uu$  denotes the tensor product of two velocity vectors and  $\sigma$  denotes the macroscopic stress tensor. It can be divided into its kinetic and contact contributions as:

$$\begin{aligned}\sigma &= \sigma^k + \sigma^c, \\ \text{where } \sigma^k &= \sum_{i=1}^N m v'_i v'_i W(r - r_i(t))\end{aligned}$$

$$\text{and } \sigma^c = \sum_{i=1}^N \sum_{j=i+1}^N F_{ij} r_{ij} \int_0^1 W(r - r_i + sr_{ij}) ds \\ + \sum_{i=1}^N \sum_{k=N+1}^{N+N_b} F_{ik} a_{ik} \int_0^1 W(r - r_i + sa_{ik}) ds$$

with interaction forces  $F_{ij} = -F_{ji}$ , branch vectors  $r_{ij} = r_i - r_j$  and contact-to-center vectors  $a_{ik} = r_i - c_{ik}$ , where  $c_{ik}$  denotes the contact point between the fluid particle  $i$  and the wall particle  $k$ . The fluctuation velocity  $v'_i$  of particle  $i$  and the pressure are defined by:

$$v'_i(r, t) = v_i(t) - u(r, t), \\ p(r, t) = \frac{1}{3} \text{tr}(\sigma(r, t)) .$$

The boundary interaction force density,  $F_b$ , is applied by the base to the flow and has nonzero values only near the basal surface. It can be introduced into continuum models as a boundary condition for the stress. The expressions will look like:

$$F_b = \sum_{i=1}^N \sum_{k=N+1}^{N+N_b} f_{ik} W(r - c_{ik}), \\ \sigma_{iz}(z = b) = \int_R F_{bi}(z) dz, \quad \text{for } i = x, y, z .$$

The so called granular temperature is a measure of the squared fluctuation velocities, that can be obtained by scaling the kinetic fluctuation energy density:

$$T_g = \frac{\text{tr}(\sigma^k)}{3\rho} .$$

The fabric tensor, which is an approximate macroscopic measure of the contact orientation distribution, is defined by:

$$F = \sum_{i=1}^N \sum_{j=1, j \neq i}^N \mathcal{V} n_{ij} n_{ij} \int_0^1 W(r - r_i + sr_{ij}) ds \\ + \sum_{i=1}^N \sum_{k=N+1}^{N+N_b} \mathcal{V} n_{ik} n_{ik} \int_0^1 W(r - r_i + sa_{ik}) ds$$

with the contact normal unit vector  $n_{ij} = \frac{r_{ij}}{|r_{ij}|}$ . The trace of the fabric is its isotropic invariant

and it is proportional to the contact number density. This leads to the coordination number

$$Z = \frac{\text{tr}(F)}{\nu} .$$

### 3.3.2 Vibrated powder and molecular analogies

In this model, a Brownian motion at a macroscopic scale is created by a vibrating cell and it has been seen that the dense-phased vibrated powders exhibit rheological behaviour archetypal of non-Newtonian viscoelastic fluids [8]. The evolution of steady state viscosity has been accurately expressed as a function of the shear rate, the frictional stress, the granular pressure, the mass of the sample, the vibration frequency, the vibration energy, the intergranular contact network meanlife and the free volume distribution. In the case of monodispersed spherical particles, the system is a suspension of unconnected particles below the random loose packing fraction  $\phi_{rlp} = 0.56$  and the momentum transport is collisional as in a gas. Between  $\phi_{rlp}$  and the random close packing fraction  $\phi_{rcp} = 0.64$ , the stress transmission is through intergranular contacts. As a consequence, the collisional part of momentum transport can generally be neglected in dense granular media and the samples behave rather like a liquid or a solid, depending on the circumstances. The intergranular contacts form a bimodal heterogeneous network constituted by a strong contact network (SCN) carrying stresses larger than the average stress and a weak contact network (WCN) carrying stresses lower than the average stress. Experimental studies show that only a small number of grains belong to the strong network and hence, solid-like and liquid-like states coexist in the system. So the stationary dense granular flows can be described by a nonlocal constitutive law accounting for the existence of transient clusters, when the medium is near the random close packing fraction. The flowing system is depicted as depicted as a temporary network of solid chains (SCN) immersed in an assembly of mobile particles (WCN) acting like an isotropic interstitial fluid. As a consequence, the stress tensor is written as a sum of three contributions: A frictional term derived from the Coulomb's law, a viscous term and a nonlocal term. The macroscopic nature of granular materials, coupled with the existence of the contact network and the resulting long-range interactions implies that their transport properties mainly depend upon the spatial arrangement of the grains resulting from the sample conditioning. So in order to determine any significant physical characteristic of a powder, one needs to obtain an average value that takes into account a representative set of spatial configurations. A system is ergodic only if it can explore all the accessible configurations during the measurement time, e.g, Brownian motion in the case of molecular system. The powders also show vertical vibrations, which generate granular agitation that have been shown to be (macro-)Brownian. The granular agitation can be quantified through the fluc-

tuating part of the average kinetic energy of the grains in terms of a granular temperature  $T_g$ , which can be viewed as the control parameter of the random kinetics of the grains. The transport properties depend strongly on their density since grains need adjacent empty spaces large enough to rearrange themselves. The required space is the free volume  $V_f$  of the system, defined as:

$$V_f = N\bar{V}_f = V - V_p - V_i = V - V_0 = V_p\left(\frac{1}{\varphi} - \frac{1}{\varphi_m}\right) = V\left(1 - \frac{\varphi}{\varphi_m}\right),$$

where  $N$  is the total number of particles,  $\bar{V}_f$  is the average free volume per free particle,  $V$  is the total volume,  $V_p$  the volume of particles,  $V_i$  the interstitial volume,  $\varphi = V_p/V$  the packing volume fraction and  $\varphi_m = V_p/(V - V_f)$  the maximum packing volume fraction. Common observation of a sand pile evidences that the sample behaves as a Hookean solid, until the tangential force  $F_t$  does not exceed a critical force  $F_c$ . In such a situation,  $F_t$  is given by:

$$F_t = F_e = k_e x \quad \text{with } x < x_c,$$

where  $F_e$  is the elastic force and  $k_e$  is the elastic constant. The granular pressure  $p$  on a surface  $\Delta S$  is related to the normal force  $F_n$  exerted on a grain by:

$$p = \bar{N}dF_n,$$

where  $\bar{d}$  is the thickness of one layer of grains,  $\bar{N} = N/V$  is the average number of grains per unit volume,  $N$  is the total number of grains and  $V$  is the total volume of the sample. The work  $W$  done by  $F_e$  when the grain moves from  $x = 0$  to  $x = x_c$  is equal to the work done against the granular pressure  $p$ , to create the corresponding volume  $v = v_c$  or equivalently against  $F_n$  to displace the adjacent grains on a characteristic length  $l_c$ . So we can write:

$$W = \frac{1}{2}k_e x_c^2 = pv_c = F_n l_c,$$

$$k_e = \frac{2v_c}{x_c^2} p = \frac{2l_c}{x_c^2} F_n = \frac{2l_c}{x_c^2} \frac{p}{\bar{N}\bar{d}} \quad \text{with } v_c = \frac{l_c}{\bar{N}\bar{d}}.$$

The intergranular connections are broken beyond  $x_c$ , resulting in a plastic irreversible deformation leading to a stick-slip process. In this configuration, the relative displacement  $x$  can be linked to the macroscopic shear strain  $\gamma$  and shear rate  $\dot{\gamma}$  in the steady-state regime through

$$\gamma = \frac{x}{d} = \dot{\gamma}t,$$

$$\gamma_c = \frac{x_c}{d} = \dot{\gamma}t_c,$$

where  $d$  is the distance between two adjacent layers of grains and  $t_c$  the critical time. The vibrations are considered to be sinusoidal and the energy  $E_v$  is calculated as that of the harmonic oscillator owning the same mass  $m$  having vibration frequency  $f$  and amplitude  $A$ ,

$$E_v = \frac{1}{2}m(2\pi f)^2 A^2 .$$

When a sample is submitted to vibrations, the related reorganization frequency  $f_b$  is equal to the vibration frequency of the cell  $f$ , modulated by the probability  $p(v_f < v_f^*)$  that a given grain has a free volume  $v_f$  greater than a characteristic free volume  $v_f^*$  beyond which spatial arrangement of neighbouring contacts becomes possible. Assuming a Boltzmann distribution of the free volume, we can write:

$$f_b = fp(v_f > v_f^*) = f \int_{v_f^*}^{\text{inf}} \rho(v_f)dv_f = f \exp(-\xi v_f^*/\bar{v}_f) .$$

Both reorganization processes, induced by shear and vibrations, are independent from each other and hence we write the total reorganization frequency  $\lambda^{-1}$  as:

$$\lambda^{-1} = \frac{\dot{\gamma}}{\gamma_c} + f_b .$$

$\lambda$  can also be seen as the mean lifetime of intergranular contacts, when the sample is under shear and vibrations. Now we can express the impulse per grain  $\iota$ , the shear stress  $\tau$  and the steady-state viscosity  $\eta$  as:

$$\iota = \int_0^\lambda F_e(t)dt = \int_0^\lambda k_e d \dot{\gamma} t dt = \frac{1}{2} k_e d \dot{\gamma} \lambda^2,$$

$$\tau = \iota \frac{\bar{N} \Delta x \Delta y \Delta z}{\lambda \Delta x \Delta z} = \frac{1}{2} \bar{N} k_e \bar{d}^2 \dot{\gamma} \lambda, \quad \text{with } G = \frac{1}{2} \bar{N} k_e \bar{d}^2 = \frac{l_c d}{x_c^2} p = \frac{\mu_c}{\gamma_c} p,$$

$$\eta = \frac{\tau}{\dot{\gamma}} = \frac{G}{f_b + \frac{\dot{\gamma}}{\gamma_c}} = \frac{\eta_0}{1 + \frac{\dot{\gamma}}{\gamma_c f_b}} = \frac{\tau_c}{\gamma_c f_b + \dot{\gamma}}, \quad \text{with } \tau_c = G \gamma_c = \eta_0 \gamma_c f_b = \eta_0 \dot{\gamma}_c = \mu_c p,$$

where  $\lambda$  is the average lifetime,  $\Delta y = \bar{d}$  the separation between two adjacent layers and  $\mu_c = l_c/x_c$  and  $\gamma_c = x_c/\bar{d}$  are two characteristic parameters.

Here we can see:

1. if  $\dot{\gamma} \ll \dot{\gamma}_c = \gamma_c f_b$ ,  $\eta \rightarrow \eta_0$ : the Brownian motion becomes more efficient than the shear, the viscosity becomes independent of shear rate and consequently the regime is Newtonian.
2. if  $\dot{\gamma} \gg \dot{\gamma}_c = \gamma_c f_b$ ,  $\tau \rightarrow \tau_c$ : the Brownian motion becomes negligible and the stress becomes independent of the shear rate. As  $\tau_c$  is also proportional to the pressure, we can write:

$$\tau_c = \mu_c p = \mu_c \sigma_n,$$

which is nothing but the Coulomb law, resulting the corresponding regime to be Coulmbian. Moreover, as this frictional stress also depend on  $\eta_0$  and the viscosity itself is proportional to the pressure, the effect of the pressure on the viscosity has to be taken into account as a first-order parameter.

For more details on how the viscosity depends on the vibrations in terms of frequency and energy, one can look up for the Vogel-Fulcher-Tammann equation.

### 3.4 Continuous model

As stated earlier that any kind of flow-problem can be modeled mathematically very precisely by the Navier-Stokes equation, it is one of the most common and important equations in continuum mechanics. We apply the law of conservation of mass and momentum on a small element in a control volume and with the help of Reynolds transport theorem, we get the following form of the Navier-Stokes equation:

$$\begin{aligned} \rho \frac{Du}{Dt} &= \nabla \cdot T + f && \text{in } \Omega \\ \text{with } \nabla \cdot u &= 0 && \text{in } \Omega, \end{aligned}$$

where  $\rho$  and  $u$  are the density and the velocity of the fluid medium in the continuous level,  $\frac{D}{Dt}$  represents the material derivative,  $T$  is the Cauchy stress tensor and  $f$  is the external force present in the domain  $\Omega$  of the system. Now if we express the Cauchy stress tensor in terms of the deviatoric stress tensor  $\sigma$  and the pressure  $p$  and furthermore the deviatoric stress tensor

$\sigma$  in terms of viscosity  $\eta$  and the rate of deformation tensor  $\dot{\gamma}$  as:

$$T = \sigma - pI$$

$$\text{and } \sigma = 2\eta\dot{\gamma},$$

the generalized Navier-Stokes equation takes the form:

$$\rho \frac{Du}{Dt} = -\nabla p + \nabla \cdot (2\eta(|\dot{\gamma}|, p)\dot{\gamma}) + f \quad \text{in } \Omega,$$

$$\text{with } \nabla \cdot u = 0 \quad \text{in } \Omega,$$

where the viscosity  $\eta$  can be constant or a function of the shear rate  $|\dot{\gamma}|$  and the pressure  $p$ . For example,

$$\eta(|\dot{\gamma}|, p) = \eta_0, \quad \text{for Newtonian fluid,} \quad (3.3)$$

$$= \eta_0 |\dot{\gamma}|^{(m-2)}, \quad \text{for Power law,} \quad (3.4)$$

$$= \eta_0 + \frac{\sqrt{2}}{2} \frac{\tau_0}{|\dot{\gamma}|}, \quad \text{for Bingham fluid,} \quad (3.5)$$

$$= \frac{\sqrt{2}}{2} p \frac{\sin \phi}{|\dot{\gamma}|}, \quad \text{for Schaeffer model,} \quad (3.6)$$

$$= \frac{\sqrt{2}}{2} p \left( \frac{\sin \phi}{|\dot{\gamma}|} + b \cos \phi |\dot{\gamma}|^{(n-1)} \right), \quad \text{for Tardos model,} \quad (3.7)$$

$$= \frac{\sqrt{2}}{2} \left( \frac{\alpha p}{|\dot{\gamma}|} + \frac{\beta dp}{\delta \sqrt{\frac{p}{\rho}} + |\dot{\gamma}| d} \right), \quad \text{for Poliquen model.} \quad (3.8)$$

Here  $\eta_0$  is a constant for the Newtonian fluid. The power index in the power law model is represented by  $m$  and  $\tau_0$  represents the yield stress of the particular Bingham fluid. For the subsequent Schaeffer, Tardos and the Poliquen model, the viscosity is dependent on the shear rate  $|\dot{\gamma}|$  and the pressure  $p$ ,  $\phi$  is the angle of internal friction of the material and  $b$ ,  $n$ ,  $\alpha$ ,  $\beta$ ,  $d$ ,  $\delta$  are experimental constants. The shear rate is expressed as  $\dot{\gamma} = \frac{1}{2}(\nabla u + (\nabla u)^T)$  and its magnitude is defined as  $|\dot{\gamma}|^2 = tr[(\dot{\gamma})^2] = \dot{\gamma} : \dot{\gamma}$ . Since sometimes the shear rate also appears in the denominator, we replace  $|\dot{\gamma}|$  by  $\sqrt{|\dot{\gamma}|^2 + \epsilon^2}$  to avoid singularity with  $\epsilon$  being a typical (small) regularization parameter. The advantage of this generalized Navier-Stokes equation is that we can formulate almost every kind of most common fluid flows (e.g. Newtonian, Power law, etc.) and we can also get a similar formulation to study the physical properties granular materials (e.g. Poliquen model).

## 3.5 Mathematical modeling of Granular materials

### 3.5.1 Landau Approach

This model is based on the Landau theory of phase transitions. It is assumed that the shear stresses in a partially fluidized granular matter are composed of two parts: The dynamic part proportional to the shear strain rate and the static part, which is strain-independent. The relative magnitude of the static shear stress is controlled by the order parameter (OP), which varies from 0 in the liquid phase to 1 in the solid phase. The OP can be related to the local entropy of the granular material and OP dynamics is coupled to the hydrodynamic equation for the granular flow. The continuum description of granular flows can be described by the momentum conservation equation:

$$\rho \frac{Du_i}{Dt} = \frac{\partial \sigma_{ij}}{\partial x_j} + \rho g_i, \quad j = 1, 2, 3$$

$$\text{with } \nabla \cdot u = 0,$$

where  $u_i$  are the components of the velocity,  $g$  is gravity and  $\frac{D}{Dt} = \partial_t + u_i \partial_{x_i}$  denotes the material derivative. On the boundary, we assume no-slip conditions  $u_i = 0$  on solid walls and kinematic boundary condition  $\frac{D\xi}{Dt} = u_n$  on free surfaces, where  $\xi$  is the displacement of the free surface and  $u_n$  is the component of velocity normal to the surface. In the static regimes, the shear stresses are determined by the applied forces, whereas in fast and dilute granular flows the shear stresses are proportional to shear strain rates and the transition from one state to another is governed by the Mohr-Coulomb criterion. We can write the stress tensor as a sum of the hydrodynamic part proportional to the flow strain rate  $\dot{\gamma}_{ij}$ , and the strain-independent part  $\sigma_{ij}^s$ . It is assumed that diagonal elements of the tensor  $\sigma_{ij}^s$  coincide with the corresponding components of the 'true' static stress tensor  $\sigma_{ii}^0$  for the immobile grain configuration in the same geometry and the shear stresses are reduced by the value of the order parameter  $\kappa$  characterizing the phase state of granular matter. So we write the stress tensor in the form:

$$\sigma_{ij} = \sigma_{ij}^s + \eta \left( \frac{\partial u_i}{\partial x_j} + \frac{\partial u_j}{\partial x_i} \right),$$

where  $\sigma_{ij}^s = \rho \sigma_{ij}^0$  for  $i \neq j$  and  $\sigma_{ii}^s = \sigma_{ii}^0$ . In a static state,  $\kappa = 1$ ,  $\sigma_{ij} = \sigma_{ij}^0$ ,  $v_i = 0$ , whereas in a fully fluidized state  $\kappa = 0$  and the shear stresses are simply proportional to the strain rates as in ordinary fluids. To have an equation for the order parameter  $\kappa$ , we adopt the standard Landau form for the free-energy-type functional  $\mathcal{F} \sim \int dr [D|\nabla\kappa|^2 + f(\kappa, \phi)]$ , which includes a local potential energy and diffusive spatial coupling. We apply pure dissipative dynamics for

the order parameter  $\kappa$ ,

$$\frac{D\kappa}{Dt} = -\frac{\delta\mathcal{F}}{\delta\kappa} .$$

The potential energy density  $f(\kappa, \phi)$  should have extrema at  $\kappa = 0$  and  $\kappa = 1$  corresponding to uniform solid and liquid phases. Without loss of generality, we write the equation for  $\kappa$  as:

$$\tau' \frac{D\kappa}{Dt} = l^2 \nabla^2 \kappa - \kappa(1 - \kappa)F(\kappa, \psi),$$

where  $\tau'$  and  $l$  are the characteristic time and length, and  $\psi = \max|\sigma_{mn}^0/\sigma_{nn}^0|$ , the maximum is sought over all possible orthogonal directions  $n$  and  $m$  in the bulk of the granular material. The simplest form of  $F(\kappa, \psi)$  which satisfies the microscopic constraints is

$$F(\kappa, \psi) = -\kappa + \frac{\psi^2 - \psi_0^2}{\psi_1^2 - \psi_0^2},$$

where the values of  $\psi_0$  and  $\psi_1$  depend on the microscopic properties of the granular material. We use a square of  $\psi$  to avoid nonanalytical behaviour at  $\sigma_{xz}^0 = 0$ . Rescaling  $t \rightarrow t/\tau$  and  $x_i \rightarrow x_i/l$  leads to

$$\frac{D\kappa}{Dt} = \nabla^2 \kappa - \kappa(1 - \kappa)(\kappa - \delta) .$$

### 3.5.2 Schaeffer model

For a powder, a constitutive equation was first introduced by Schaeffer [17] which has to obey the yield condition  $\|\sigma\| = \sqrt{2}p \sin \phi$  and the flow rule  $\sigma = \lambda \dot{\gamma}$  respectively with  $\lambda \geq 0$ . In fact, the flow rule is based on a yield criterion for granular materials of von Mises type, which is basically derived from a law of sliding friction applied to the individual particles. Specifically in terms of the principal stresses  $S_i$ , this condition is written as:

$$\sum_{i=1}^3 (S_i - p)^2 \leq k^2 p^2 \quad p = \frac{1}{3} \text{tr} T,$$

where  $k = \sqrt{2} \sin \phi$  is a characteristic constant of the material and  $S_i$  are the eigenvectors of  $T_{ij}$ . For a material that deforms plastically, equality must hold

$$\sum_{i=1}^3 (S_i - p)^2 = k^2 p^2 .$$

Under plain strain  $p = \frac{1}{2}(S_1 + S_2)$ , we may consider a strictly 2D-yield condition:

$$(S_1 - p)^2 + (S_2 - p)^2 = 2p^2 \sin^2 \phi .$$

A constitutive equation between stress and strain was proposed for slow powder by Schaeffer [17]. This equation obeys the von Mises yield condition and the described flow rule:

$$T = -pI + \sqrt{2}p \sin \phi \frac{\dot{\gamma}}{|\dot{\gamma}|} .$$

In fact, the flow rule is assumed to have the form  $T = -pI + \lambda \dot{\gamma}$ , where  $\lambda$  is a coefficient. To satisfy the yield condition of the given flow rule in terms of von Mises, i.e.  $\|\sigma\| = \sqrt{2}p \sin \phi$ , then there must hold:

$$\lambda = \frac{\sqrt{2}p \sin \phi}{|\dot{\gamma}|} .$$

Next we deduct the deviatoric stress and then use this correlation to obtain finally the viscosity formulation as:

$$\begin{aligned} \sigma &= \frac{\sqrt{2}p \sin \phi}{|\dot{\gamma}|} \dot{\gamma}, \\ \eta &= \frac{\sigma}{2\dot{\gamma}} = \frac{\sqrt{2}}{2} \frac{p \sin \phi}{|\dot{\gamma}|} . \end{aligned}$$

### 3.5.3 Tardos model

There is theoretical evidence that in the intermediate regime, where the flow is fast enough but still dense, the friction coefficient (the ratio of shear to normal stress) increases from its constant value. While friction during very slow motion is only a function of the character of the surface and the normal load, at higher shearing rates, it becomes a function of the rate itself and increases as the rate of shearing increases. An experimental yield condition can be obtained from the experiments in the Couette device for the case when the powder transitions from the quasi-static to the intermediate regime of the flow [17],

$$\frac{\tau}{\sigma} = a + b|\dot{\gamma}|^n,$$

where  $\tau$  and  $\sigma$  are the shear and the normal stresses and  $a$ ,  $b$  and  $n$  are coefficients characterized by the experimental curve. The notation for the modulus of the shear rate  $|\dot{\gamma}|$  is used to designate that only its magnitude is of relevance and not its direction. The experimental value of the coefficient  $a$  falls in the majority of cases between  $\sin \phi$  and  $\tan \phi$  and we make a slight

generalization here by replacing it by  $\tan \phi$  to obtain:

$$\frac{\tau}{\sigma} = \tan \phi + b|\dot{\gamma}|^n,$$

where  $\phi$  is the angle of internal friction of the material. This equation has a great advantage that it reduces to the Coulomb yield condition at zero shearing. An equivalent representation of the Coulomb yield condition  $\tau = \sigma \tan \phi + c$  can be obtained from the characteristic Mohr circle, by replacing  $\sigma$  by  $p$  and  $\tau / \tan \phi$  by  $q / \sin \phi$  in the form prescribed by R. M. Nedderman [14]:

$$q = p \sin \phi + c \cos \phi,$$

where  $q$  is half of the difference between the principal stresses and  $c$  is referred to as cohesion. The deviatoric part of the constitutive equation for flow of a dry powder in the quasi-static regime is:

$$\sigma = \frac{\sqrt{2}p \sin \phi}{|\dot{\gamma}|} \dot{\gamma} = \frac{\sqrt{2}q}{|\dot{\gamma}|} \dot{\gamma},$$

where  $\dot{\gamma}$  is the rate of deformation tensor,  $|\dot{\gamma}|$  is its magnitude. We replace  $q$  by  $c = b|\dot{\gamma}|^n$  to obtain:

$$\sigma = \sqrt{2}p (\sin \phi + b \cos \phi |\dot{\gamma}|^n) \frac{\dot{\gamma}}{|\dot{\gamma}|}.$$

This is the constitutive equation that includes the behavior at very low and higher shear rates characteristic of the intermediate regime of powder flow. The first term in the right hand side of the above equation corresponds to the plastic deformation (frictional or solid-like behavior), while the second term corresponds to the viscous behavior (liquid-like) of the granular material. The effective viscosity is calculated by:

$$\eta = \frac{\sigma}{2\dot{\gamma}} = \frac{\sqrt{2}}{2} p \left( \frac{\sin \phi}{|\dot{\gamma}|} + b \cos \phi |\dot{\gamma}|^{(n-1)} \right).$$

### 3.5.4 Poliquen model

In this model, the rheology assumes that the granular material behaves like an incompressible fluid with a visco-plastic constitutive law [1]. For rigid particles in the large systems, the system is controlled by Inertial field  $I$ , which is a single dimensionless parameter and defined

by:

$$I = \frac{|\dot{\gamma}|d}{\sqrt{p/\rho}} .$$

It is important to note that the macroscopic friction coefficient  $\mu(I)$  does not depend on the microscopic properties of the grains in the range of inertial number corresponding to the dense flow regime. Changing the coefficient of restitution of the grains or the inter-particle friction coefficient, does not change the macroscopic friction. The inertial field can be interpreted as the ratio between two time scales - a microscopic time scale  $\frac{d}{\sqrt{p/\rho}}$ , which represents the time required for a particle to fall in a hole of size  $d$  under pressure  $p$ , and which gives the typical timescale of rearrangements and a macroscopic timescale  $\frac{1}{\dot{\gamma}}$  coming from the mean deformation. Also small  $I$  corresponds to a quasi-static regime in the sense that macroscopic deformation is slow as compared to microscopic rearrangements, whereas large values of  $I$  correspond to rapid flows. It could be seen that to switch from quasi-static to inertial regime, one can either increase the shear rate or decrease the pressure. Fitting the experiments and numerical simulations, it is possible to propose analytical expressions for the friction law and volume fraction law, which can be then used to study other configurations. An example of phenomenological expressions are:

$$\mu(I) = \mu_s + \frac{\mu_2 - \mu_s}{1 + \frac{I_0}{I}},$$

where  $\mu_s$ ,  $\mu_2$  and  $I_0$  are the material dependent parameters. Here as we consider that the shear stress tensor is colinear to the shear rate tensor and the flow is incompressible, i.e. we neglect the variation of volume fraction and assume that the pressure is isotropic in nature. Then we can write the stress tensor in terms of effective viscosity as:

$$\sigma = \frac{\sqrt{2}\mu(I)p}{|\dot{\gamma}|}\dot{\gamma},$$

where  $|\dot{\gamma}|$  being the modulus shear rate tensor. Now we combine all the expressions for inertial number, frictional coefficient and the effective viscosity and we get following expression:

$$\begin{aligned}
\sigma &= \frac{\sqrt{2}\mu(I)p}{|\dot{\gamma}|} \dot{\gamma} \\
&= \sqrt{2} \left( \mu_s + \frac{\mu_2 - \mu_s}{1 + \frac{I_0}{I}} \right) \frac{p\dot{\gamma}}{|\dot{\gamma}|} \\
&= \sqrt{2} \left( \alpha + \frac{\beta I}{I + I_0} \right) \frac{p\dot{\gamma}}{|\dot{\gamma}|} && \text{where } \alpha = \mu_s, \beta = \mu_2 - \mu_s \\
&= \sqrt{2} \left( \alpha + \frac{\beta \frac{|\dot{\gamma}|d}{\sqrt{p/\rho}}}{\frac{|\dot{\gamma}|d}{\sqrt{p/\rho}} + \delta} \right) \frac{p\dot{\gamma}}{|\dot{\gamma}|} && \text{where } \delta = I_0 \\
&= \sqrt{2} \left( \frac{\alpha p}{|\dot{\gamma}|} + \frac{\beta dp}{|\dot{\gamma}|d + \delta\sqrt{p/\rho}} \right) \dot{\gamma} .
\end{aligned}$$

Within this description, the granular liquid is described as an incompressible non-Newtonian fluid with an effective viscosity

$$\eta_{eff} = \frac{\sqrt{2}}{2} \left( \frac{\alpha p}{|\dot{\gamma}|} + \frac{\beta dp}{|\dot{\gamma}|d + \delta\sqrt{p/\rho}} \right) .$$

This general described formulation can be used to investigate different type of configurations for the flow of granular media. For example, we aim to study the velocity distribution in a 2D couette flow, which is presented in Section 6. So the governing equation for this model takes the form:

$$\begin{aligned}
-\nabla \cdot \left[ \sqrt{2} \left( \frac{\alpha p}{|\dot{\gamma}|} + \frac{\beta dp}{|\dot{\gamma}|d + \delta\sqrt{p/\rho}} \right) \dot{\gamma} \right] + u \cdot \nabla u + \nabla p &= 0 && \text{in } \Omega \\
\text{with } \nabla \cdot u &= 0 && \text{in } \Omega
\end{aligned}$$



## 4 Mathematical Background

### 4.1 Preliminaries

#### 4.1.1 Sobolev space

Let  $\Omega$  denote an open subset of  $\mathbb{R}^N$  with boundary  $\Gamma$ . We define  $D(\Omega)$  to be the linear space of infinitely differentiable functions with compact support on  $\Omega$ . Then we set

$$D(\bar{\Omega}) = \phi|_{\Omega}; \quad \phi \in D(\mathbb{R}^N)$$

or equivalently, if  $\Theta$  denotes any open subset of  $\mathbb{R}^N$  such that  $\bar{\Omega} \subset \Theta$ ,

$$D(\bar{\Omega}) = \phi|_{\Omega}; \quad \phi \in D(\Theta) .$$

Now let  $D'(\Omega)$  denote the dual space of  $D(\Omega)$ , often called the space of distributions on  $\Omega$ . We denote the duality pairing between  $D'(\Omega)$  and  $D(\Omega)$  by  $\langle \cdot, \cdot \rangle$  and we remark that when  $f$  is a locally integrable function, then  $f$  can be identified with a distribution by:

$$\langle f, \phi \rangle = \int_{\Omega} f(x)\phi(x)dx \quad \forall \phi \in D(\Omega) .$$

Now we can define the derivatives of distributions. Let  $\alpha = (\alpha_1, \alpha_2, \dots, \alpha_N) \in \mathbb{N}^N$  and set

$$|\alpha| = \sum_{i=1}^N \alpha_i .$$

For  $u$  in  $D'(\Omega)$ , we define  $\partial^{\alpha}u$  in  $D'(\Omega)$  by:

$$\langle \partial^{\alpha}u, \phi \rangle = (-1)^{|\alpha|} \langle u, \partial^{\alpha}\phi \rangle \quad \forall \phi \in D(\Omega) .$$

If  $u$  is  $|\alpha|$  times differentiable,  $\partial^{\alpha}u$  coincides with the usual notion of derivative

$$\partial^{\alpha}u = \frac{\partial^{|\alpha|}u}{\partial x_1^{\alpha_1} \dots \partial x_N^{\alpha_N}} .$$

For each integer  $m \geq 0$  and real  $p$  with  $1 \leq p \leq \infty$ , we define the Sobolev space:

$$W^{m,p}(\Omega) = \{v \in L^p(\Omega); \partial^{\alpha}v \in L^p(\Omega) \quad \forall |\alpha| \leq m\},$$

which is a Banach space with the norm

$$\|u\|_{m,p,\Omega} = \left( \sum_{|\alpha| \leq m} \int_{\Omega} |\partial^{\alpha} u(x)|^p dx \right)^{1/p}, \quad p < \infty$$

or

$$\|u\|_{m,\infty,\Omega} = \max_{|\alpha| \leq m} \left( \text{ess sup}_{x \in \Omega} |\partial^{\alpha} u(x)| \right), \quad p = \infty.$$

We also provide  $W^{m,p}(\Omega)$  with the following seminorm

$$|u|_{m,p,\Omega} = \left( \sum_{|\alpha|=m} \int_{\Omega} |\partial^{\alpha} u(x)|^p dx \right)^{1/p}, \quad p < \infty$$

and we make the above modification when  $p = \infty$ . If  $u$  belongs to  $W^{m,p}(\Theta)$  for every measurable, compact proper subset  $\Theta$  of  $\Omega$ , we say that  $u$  is locally in  $W^{m,p}(\Omega)$  and write:

$$u \in W_{loc}^{m,p}(\Omega).$$

When  $p = 2$ ,  $W^{m,2}(\Omega)$  is usually denoted by  $H^m(\Omega)$  and if there is no ambiguity, we drop the subscript  $p = 2$  when referring to its norm and seminorm.  $H^m(\Omega)$  is a Hilbert space for the scalar product

$$(u, v)_{m,\Omega} = \sum_{|\alpha| \leq m} \int_{\Omega} \partial^{\alpha} u(x) \partial^{\alpha} v(x) dx.$$

In particular, we write the scalar product of  $L^2(\Omega)$  with no subscript at all and we also define the subspace  $H_0^m(\Omega)$  to be all functions in the Sobolev space  $W^{m,2}(\Omega)$ , whose trace is zero.

#### 4.1.2 Bilinear form

Let us define the bilinear form using the Poisson equation in a convex polygonal domain  $\Omega$  [34]

$$\begin{aligned} -\Delta u &= f, \\ u|_{\partial\Omega} &= 0, \end{aligned}$$

where  $f \in L_2(\Omega)$ . For  $u \in H_0^1(\Omega) \cap H^2(\Omega)$ ,

$$\|u\|_2 \leq C_{\Omega} \|f\|_0,$$

where  $\|\cdot\|_2 := \|\cdot\|_{H^2(\Omega)}$  and  $\|\cdot\|_0 := \|\cdot\|_{L^2(\Omega)}$  .

To derive the weak formulation, first consider a test function  $v \in H_0^1(\Omega)$  and then multiply the above equation with  $v$  and integrate by parts to obtain the problem:

Find  $u \in H_0^1(\Omega)$  such that:

$$a(u, v) = F(v) \quad \forall v \in H_0^1(\Omega), \text{ where}$$

$$a(u, v) = \int_{\Omega} \nabla u \nabla v dx, \quad F(v) = \int_{\Omega} f v dx .$$

Let  $\mathcal{T}_h$  be a triangulation of the domain  $\Omega$  and  $V_h$  be the space of approximations, then the approximate problem reads:

Find  $u_h \in V_h(\Omega)$  such that

$$a_h(u_h, v) = F(v) \quad \forall v \in V_h, \text{ where}$$

$$a_h(u, v) = \sum_{T \in \mathcal{T}_h} \int_T \nabla u \nabla v dx \quad \forall u, v \in V_h .$$

#### 4.1.3 Error Analysis

In order to obtain a conforming finite element approximation, let us introduce a finite dimensional subspace  $V_h^c \subseteq H_0^1(\Omega)$  [35]

$$V_h^c = \{v \in L_2(\Omega) : v|_T \in P_1(T), \forall T \in \mathcal{T}_h, v \text{ is continuous at the}$$

$$\text{vertices of } \mathcal{T}_h \text{ and } v = 0 \text{ at the vertices along } \partial\Omega\}$$

and define the norm  $\|v\|_1 = (a(v, v))^{\frac{1}{2}} = |v|_{H^1(\Omega)}$ . It follows from  $V_h^c \subseteq H_0^1(\Omega)$  that if  $a_h(u, v) = a(u, v) \quad \forall u, v \in V_h^c$ , then

$$\|u - u_h\|_1 = \min_{v \in V_h} \|u - v\|_1 .$$

With the linear interpolation operator  $\pi_h$  and for  $u \in H^2(\Omega)$  the error estimate holds:

$$\|u - u_h\|_1 \leq \|u - \pi_h u\|_1 \leq Ch \|u\|_2 .$$

#### 4.1.4 Weak formulation

We express the Cauchy stress tensor  $T$  as:

$$T = 2\eta\dot{\gamma} - pI,$$

$$\text{where } \dot{\gamma} = \frac{1}{2} [\nabla u + (\nabla u)^T] .$$

So the Navier Stokes equation takes the form:

$$\begin{aligned} \rho \frac{Du}{Dt} &= \nabla \cdot (2\eta\dot{\gamma} - pI) + f \\ &= \nabla \cdot \left( 2\eta \frac{1}{2} (\nabla u + (\nabla u)^T) - pI \right) + f \\ &= \eta \nabla^2 u + \eta \nabla \cdot (\nabla u)^T - \nabla p + f \\ &= \eta \nabla^2 u + \eta \nabla (\nabla \cdot u) - \nabla p + f \\ &= \eta \nabla^2 u - \nabla p + f . \end{aligned}$$

Here we use the condition  $\nabla \cdot u = 0$  for incompressible flow.

From the Navier Stokes equation, we take the stationary form as:

$$u \cdot \nabla u = \eta \nabla^2 u - \nabla p + f .$$

So now we have the following system of equations in strong form:

$$\begin{aligned} u \cdot \nabla u - \eta \nabla^2 u + \nabla p &= f \\ \text{and } \nabla \cdot u &= 0, \end{aligned}$$

where the unknown variables are  $u \in C^2$  and  $p \in C^1$ . But we derive the weak formulation so that the solution space can be relaxed. We take  $v \in H_0^1$  and multiply with the first equation and by integrating over the whole domain, we get:

$$\int_{\Omega} (u \cdot \nabla u) v d\Omega - \eta \int_{\Omega} \nabla^2 u v d\Omega + \int_{\Omega} \nabla p v d\Omega = \int_{\Omega} f v d\Omega$$

$$\text{Or, } \int_{\Omega} (u \cdot \nabla u) v d\Omega - \eta \left( \int_{d\Omega} \nabla u v d\tau - \int_{\Omega} \nabla u \nabla v d\Omega \right) + \left( \int_{d\Omega} p v d\tau - \int_{\Omega} p \nabla \cdot v d\Omega \right) = \int_{\Omega} f v d\Omega$$

$$\text{Or, } \int_{\Omega} (u \cdot \nabla u) v d\Omega + \eta \int_{\Omega} \nabla u \nabla v d\Omega - \int_{\Omega} p \nabla \cdot v d\Omega = \int_{\Omega} f v d\Omega .$$

Similarly we take  $q \in L^2$  and multiply with the second equation and by integrating the whole domain, we get:

$$\int_{\Omega} \nabla \cdot u q d\Omega = 0 .$$

Now we define bilinear forms as:

$$\begin{aligned} A(u, v) &= \int_{\Omega} (u \cdot \nabla u) v d\Omega + \eta \int_{\Omega} \nabla u \nabla v d\Omega \\ B(p, v) &= - \int_{\Omega} p \nabla \cdot v d\Omega \\ l(v) &= \int_{\Omega} f v d\Omega . \end{aligned}$$

So we get the system of weak formulation as:

$$\begin{aligned} A(u, v) + B(p, v) &= l(v) \\ B^T(q, v) &= 0 . \end{aligned}$$

Now we can write the complete algorithm of the approximate linearized problem in following algebraic system: Compute u and p by solving

$$\begin{pmatrix} A & B \\ B^T & 0 \end{pmatrix} \times \begin{pmatrix} u \\ p \end{pmatrix} = \begin{pmatrix} Res_u \\ Res_p \end{pmatrix}$$

#### 4.1.5 Weak formulation with Deformation tensor

Let us again take the stationary form of Navier-Stokes equation for Newtonian fluid as:

$$\begin{aligned} u \cdot \nabla u &= 2\eta \nabla \cdot \dot{\gamma} - \nabla p + f \\ \text{Or, } u \cdot \nabla u - 2\eta \nabla \cdot D(u) + \nabla p &= f, \quad \text{where } D(u) = \dot{\gamma} = \frac{1}{2} [\nabla u + (\nabla u)^T] . \end{aligned}$$

If we take a test function v and integrate after multiplying the above equation with v, we get the weak formation:

$$\int_{\Omega} (u \cdot \nabla u) v d\Omega + 2\eta \int_{\Omega} D(u) : \nabla v d\Omega + \int_{\Omega} (u \cdot \nabla u) v d\Omega - \int_{\Omega} p \nabla \cdot v d\Omega = \int_{\Omega} f v d\Omega .$$

Now we write:

$$\begin{aligned}\nabla v &= \frac{1}{2} [\nabla v + (\nabla v)^T] + \frac{1}{2} [\nabla v - (\nabla v)^T] \\ &= D(v) + \frac{1}{2} [\nabla v - (\nabla v)^T] .\end{aligned}$$

Then we show:

$$\begin{aligned}D(u) : [\nabla v - (\nabla v)^T] &= \text{tr} \left( \begin{array}{cc} 2 \frac{\partial u_1}{\partial x} & \frac{\partial u_1}{\partial y} + \frac{\partial v_2}{\partial x} \\ \frac{\partial u_1}{\partial y} + \frac{\partial v_2}{\partial x} & \frac{\partial v_2}{\partial y} \end{array} \right) \times \left( \begin{array}{cc} 0 & \frac{\partial v_1}{\partial y} - \frac{\partial v_2}{\partial x} \\ \frac{\partial v_2}{\partial x} - \frac{\partial v_1}{\partial y} & 0 \end{array} \right) \\ &= \left( \frac{\partial u_1}{\partial y} + \frac{\partial v_2}{\partial x} \right) \left( \frac{\partial v_2}{\partial x} - \frac{\partial v_1}{\partial y} \right) + \left( \frac{\partial u_1}{\partial y} + \frac{\partial v_2}{\partial x} \right) \left( \frac{\partial v_1}{\partial y} - \frac{\partial v_2}{\partial x} \right) \\ &= 0 .\end{aligned}$$

So,

$$\begin{aligned}2\eta \int_{\Omega} D(u) : \nabla v d\Omega &= 2\eta \int_{\Omega} D(u) : \left( D(v) + \frac{1}{2} [\nabla v - (\nabla v)^T] \right) d\Omega \\ &= 2\eta \int_{\Omega} D(u) : D(v) d\Omega + 2\eta \int_{\Omega} D(u) : \frac{1}{2} [\nabla v - (\nabla v)^T] d\Omega \\ &= 2\eta \int_{\Omega} D(u) : D(v) d\Omega + \eta \int_{\Omega} D(u) : [\nabla v - (\nabla v)^T] d\Omega \\ &= 2\eta \int_{\Omega} D(u) : D(v) d\Omega .\end{aligned}$$

Therefore we get the same weak formulation also with the deformation tensor as:

$$\begin{pmatrix} A & B \\ B^T & 0 \end{pmatrix} \times \begin{pmatrix} u \\ p \end{pmatrix} = \begin{pmatrix} Res_u \\ Res_p \end{pmatrix}$$

$$\begin{aligned}\text{where } A(u, v) &= \int_{\Omega} (u \cdot \nabla u) v d\Omega + 2\eta \int_{\Omega} D(u) : D(v) d\Omega \\ B(p, v) &= - \int_{\Omega} p \nabla \cdot v d\Omega \\ l(v) &= \int_{\Omega} f v d\Omega .\end{aligned}$$

#### 4.1.6 Problem formulation with Generalized Navier Stokes equation

Let us consider the stationary generalized Navier-Stokes problem in a bounded domain  $\Omega \subset R^2$ . If we restrict the set  $V$  of test functions to be divergence-free and take the constitutive laws into account, the (stationary) equations lead to: Find  $u \in V$  such that

$$\int_{\Omega} 2\eta(|\dot{\gamma}|, p)D(u) : D(v)dx + \int_{\Omega} (u \cdot \nabla u)v dx = \int_{\Omega} f v dx, \quad \forall v \in V .$$

It is straightforward to penalize the constraint  $\nabla \cdot u = 0$  to derive the equivalent mixed formulation: Find  $(u, p) \in X \times M$  such that

$$\begin{aligned} \int_{\Omega} 2\eta(|\dot{\gamma}|, p)D(u) : D(v)dx + \int_{\Omega} (u \cdot \nabla u)v dx + \int_{\Omega} p \operatorname{div} v dx &= \int_{\Omega} f v dx, \quad \forall v \in X; \\ \text{with } \int_{\Omega} q \operatorname{div} u dx &= 0, \quad \forall q \in M \end{aligned}$$

with spaces  $X = H_0^1(\Omega)$  and  $M = L^2(\Omega)$  for the Newtonian case. In general these spaces depend on the function  $\eta$ . Also, the related Stokes problems has to be considered, which means that the convective term  $\int_{\Omega} (u \cdot \nabla u)v dx$  has to be omitted. For the following analysis, let us introduce the bilinear forms:

$$\begin{aligned} \langle L(w, q)u, v \rangle &= \int_{\Omega} 2\eta(|\dot{\gamma}|(w), q)D(u) : D(v)dx; \\ \langle N(w)u, v \rangle &= \int_{\Omega} (w \cdot \nabla u)v dx; \\ \langle Bq, v \rangle &= \int_{\Omega} q \operatorname{div} v dx . \end{aligned}$$

Then we can rewrite the generalized flow problem in the compact form: Find  $(u, p) \in X \times M$  such that

$$\begin{aligned} \langle L(u, p)u, v \rangle + \langle N(u)u, v \rangle + \langle Bp, v \rangle &= \int_{\Omega} f v dx, \quad \forall v \in X; \\ \langle Bq, u \rangle &= 0, \quad \forall q \in M . \end{aligned}$$

#### 4.1.7 Discrete Newton solver

There is a well known solver technique named Discrete Newton solver as an alternative of its continuous version and here we give a short description about that. After applying the discretization method to the above system where the approximations belong to the finite dimensional spaces 4.10 and 4.11, a system for the residual of nonlinear algebraic equations is

obtained:

$$Res(x) = 0,$$

where  $x$  represents the vector of the coefficients corresponding to the unknowns  $(u_h, p_h)$ . To solve this system, let us apply a Newton method with damping which results in iterations of the form:

$$x^{n+1} = x^n - w^n \left[ \frac{\partial Res(x^n)}{\partial x} \right]^{-1} Res(x^n) .$$

This iteration is repeated until a certain conditions on the quality of the solution are met, which means a certain norm of the residual  $\|Res(x^n)\|$  is small enough. The damping parameter  $w^n \in (0, 1)$  is chosen such that

$$Res(x^{n+1}) \cdot x^{n+1} \leq Res(x^n) \cdot x^n .$$

The damping greatly improves the robustness of the Newton iteration in the case when the current approximation  $x^n$  is not close enough to the final solution since the Newton method without damping is not guaranteed to converge. The Jacobian matrix  $\left[ \frac{\partial Res(x^n)}{\partial x} \right]$  can be approximated using central finite differences as:

$$\left[ \frac{\partial Res(x^n)}{\partial x} \right]_{ij} = \frac{Res_i(x^n + \epsilon e_j) - Res_i(x^n - \epsilon e_j)}{2\epsilon},$$

where the vector  $e_j = (\delta_{ij})$  and  $\delta_{ij}$  is the standard Kronecker symbol. The parameter  $\epsilon$  can be fixed or can be modified according to some norm of the solution  $\|x^n\|$  or the norm of the update in the previous step  $\|x^n - x^{n-1}\|$ .

#### 4.1.8 Continuous Newton solver

The nonlinearity in the problem can be handled by a continuous Newton solver on the continuous level. Let  $(u^l, p^l)$  be the initial state for the diffusive term, then the continuous Newton method consists of finding  $(u, p) \in V \times M$  such that

$$\begin{aligned} \int_{\Omega} 2\eta(|\dot{\gamma}|(u^l), p^l) D(u) : D(v) dx + \int_{\Omega} 2\partial_1 \eta(|\dot{\gamma}|(u^l), p^l) [D(u^l) : D(u)] [D(u^l) : D(v)] dx \\ + \int_{\Omega} 2\partial_2 \eta(|\dot{\gamma}|(u^l), p^l) [D(u^l) : D(v)] p dx \\ = \int_{\Omega} f v dx - \int_{\Omega} 2\eta(|\dot{\gamma}|(u^l), p^l) D(u^l) : D(v) dx, \forall v \in V, \end{aligned}$$

where  $V$  is a divergence free velocity field and  $\partial_i \eta(\cdot, \cdot); i = 1, 2$  is the partial derivative of  $\eta$  related to the first and second variables respectively. To see this, set  $X = D(u^l), x = D(u), Y = p^l, y = p, F(x, y) = \eta(\frac{1}{2}|x|^2, y)x$  and  $f(t) = F(X + tx, Y + ty)$  so that

$$\begin{aligned}\partial_{x_j} F_i(x, y) &= \partial_{x_j} \eta(\frac{1}{2}|x|^2, y)x_j x_i + \eta(\frac{1}{2}|x|^2, y)\delta_{ij} \\ \partial_y F_i(x, y) &= \partial_y \eta(\frac{1}{2}|x|^2, y)x_i,\end{aligned}$$

where  $\delta_{ij}$  stands for the standard Kronecker symbol. Having

$$\begin{aligned}f'_i(t) &= \sum_j \partial_{x_j} F_i(X + tx, Y + ty)x_j + \partial_y F_i(X + tx, Y + ty)y \\ &= \eta(\frac{1}{2}|X + tx|^2, Y + ty)x_i + \partial_1 \eta(\frac{1}{2}|X + tx|^2, Y + ty)(X + tx, x)(X_i + tx_i) \\ &\quad + \partial_2 \eta(\frac{1}{2}|X + tx|^2, Y + ty)y(X_i + tx_i)\end{aligned}$$

and then decreasing  $t$  towards zero, we obtain the Frechet derivative:

$$\begin{aligned}\nabla \cdot [2\eta(|\dot{\gamma}|(u^l), p^l)D(u) + 2\partial_1 \eta(|\dot{\gamma}|(u^l), p^l)(D(u^l) : D(u))D(u^l) \\ + 2\partial_2 \eta(|\dot{\gamma}|(u^l), p^l)pD(u^l)] .\end{aligned}$$

Finally, the resulting auxiliary subproblems in each Newton step consist of finding  $(u, p) \in X \times M$  as the solutions of the linear systems:

$$\begin{aligned}L(u^l, p^l)u + \delta_d L^*(u^l, p^l)u + Bp + \delta_p B^*(u^l, p^l)p &= Res_u(u^l, p^l) \\ B^T u &= Res_p(u^l, p^l),\end{aligned}$$

where  $Res_u(\cdot, \cdot)$  and  $Res_p(\cdot, \cdot)$  corresponds the nonlinear residual terms for the momentum and continuity equations. The operators  $L^*(u^l, p^l)$  and  $B^*(u^l, p^l)$  are defined as follows:

$$\begin{aligned}\langle L^*(u^l, p^l)u, v \rangle &= \int_{\Omega} 2\partial_1 \eta(|\dot{\gamma}|(u^l), p^l)[D(u^l) : D(u)][D(u^l) : D(v)]dx; \\ \langle B^*(u^l, p^l)v, p \rangle &= \int_{\Omega} 2\partial_2 \eta(|\dot{\gamma}|(u^l), p^l)[D(u^l) : D(v)]pdx .\end{aligned}$$

Similarly, the corresponding Newton linearization applied to the convective term  $\langle N(u)u, v \rangle$  leads to the additional bilinear form:

$$\langle N(u^l)u, v \rangle + \delta_c \langle N^*(u^l)u, v \rangle \quad \forall v \in X,$$

where  $\langle N^*(u^l)u, v \rangle = \int_{\Omega} (u \cdot \nabla u^l) v dx \quad \forall v \in X$  .

Finally we can write the complete algorithm of the approximate linearized problem in following algebraic system: Compute  $u$  and  $p$  by solving

$$\begin{pmatrix} A & \tilde{B} \\ B^T & 0 \end{pmatrix} \times \begin{pmatrix} u \\ p \end{pmatrix} = \begin{pmatrix} Res_u \\ Res_p \end{pmatrix} \quad (4.9)$$

$$\text{where } Au = [(L + \delta_d L^*)(u^l, p^l) + (\tilde{N} + \delta_c N^*)(u^l)]u,$$

$$\tilde{B}p = [B + \delta_p B^*(u^l, p^l)]p .$$

Remarks: The full Newton method is performed for  $\delta_d = 1, \delta_c = 1$  and  $\delta_p = 1$ , while the Fixed point method corresponds to  $\delta_d = 0, \delta_c = 0$  and  $\delta_p = 0$ .

## 4.2 Discretization aspect

The finite element pair  $Q_2/P_1$ , being potentially of 3rd order accuracy due to the biquadratic polynomials for velocity and the linear pressure approximation, is one of the most popular discretization techniques in the CFD community. Though special nonconforming FEM elements like  $\tilde{Q}_1/Q_0$  Stokes element have been developed which provide an optimal approximation error of one order less; such linear finite elements seem to require much more degrees of freedom to satisfy a prescribed accuracy than compared with the quadratic  $Q_2/P_1$  ansatz, while they show a much superior behavior at the same time with respect to the efficiency of the involved solvers.

We discretize our continuous problem by the standard Galerkin finite element method, hereby approximating the domain  $\Omega$  by a domain  $\Omega_h$  with piecewise linear boundary which is equipped with a quadrilateral mesh  $\mathcal{T}_h$ . On this mesh, we define the finite dimensional spaces  $V_h$  and  $P_h$  for the velocity and the the pressure approximation as:

$$V_h = \{v_h \in H_0^1(\Omega_h)^2, \quad v_h|_T \in Q_2(T)^2 \quad \forall T \in \mathcal{T}_h, v_h = 0 \text{ on } \partial\Omega_h\}, \quad (4.10)$$

$$P_h = \{p_h \in L^2(\Omega_h), \quad p_h|_T \in P_1(T) \quad \forall T \in \mathcal{T}_h\} . \quad (4.11)$$

By  $Q_2(T)$  we denote the standard biquadratic space on the quadrilateral  $T$  which, when transformed by the bilinear transformation to the reference quadrilateral  $T_{ref} = (-1, 1)^2$ , is defined by:

$$Q_2(T_{ref}) = \text{span}\{1, x, y, xy, x^2, y^2, x^2y, xy^2, x^2y^2\}$$

with the 9 local degrees of freedom located at the vertices, midpoints of the edges and in the center of the quadrilateral. The space  $P_1(T)$  consists of linear functions defined on the reference element by:

$$P_1(T_{ref}) = \text{span}\{1, x, y\}$$

with the function value and both partial derivatives in the center of the quadrilateral as its 3 local degrees of freedom. Recently, we modified the ansatz via using a non-parametric version for  $P_1(T)$  working without transformation to the reference element.

### 4.3 The Numerical Solver

As it has been specified earlier that the choice of the characteristic function  $f(Q_n)$  for the increment of the weighing parameter  $\delta^i \in [0, 1]$ ,  $\delta^i = \delta^d, \delta^c, \delta^p$  of the discretization matrices is based on simple and preliminary numerical experiments, the motivation and the evolution of this particular function will be now discussed in details in this chapter. In this context we would like to mention that the results, which are presented here, are for the simulations of the Navier Stokes equation on the level 2 for the regularized Bingham fluid Eq. 3.3 with the physical parameters  $\eta_0 = 1E - 3$ ,  $\epsilon = 0.01$  in the Flow around cylinder geometry Fig. 5.1 with the tolerance limit of  $1E - 12$ . The associated geometry and the benchmarking results will be presented in details in Section 5.

Initially we start with a pure Fixed Point solver, which is slow and a pure Newton solver, which can be unstable. So we try to figure out whether it is possible to build a mixed Newton solver with the advantages of both the Fixed point and Newton solver. To be more specific, at this moment such a solver is desirable, which is not as slow as the Fixed Point solver and also not unstable like the pure Newton solver. So we want to make an adaptive version of Newton solver, which starts from the Fixed Point state and changes ultimately to pure (full) Newton state in an adaptive way. In the transient (mixed) state, it changes itself from (more) Fixed Point to (more) Newton if faster convergence is possible and conversely it changes from (more)

Newton to (more) Fixed Point if it finds itself unstable. Or in other words, we start with an initial  $\delta^i$ , which is zero or small non-zero (typically  $\leq 0.5$ ), and after some transient values it finally takes a steady value of 1.

#### 4.3.1 Phase 1

As we have no idea how to modulate the transient states in the beginning, we start with only two states - namely Fixed Point and pure Newton states. We are aware from our initial experiments that our configuration for the Bingham fluid is still stable for  $\delta_i = 0.5$  and we incorporate a module based on a parameter named as convergence radius  $\varepsilon$ , which can be prescribed any desired value. We start the solver with partial Fixed Point state with  $\delta^i = 0.5$  and as soon as the residual becomes less than  $\varepsilon$ , it converts itself to pure Newton states with  $\delta^i = 1.0$ . So  $\delta_i$  takes the value initially 0.5 and finally 1.0 and the change happens only one time and at one direction.

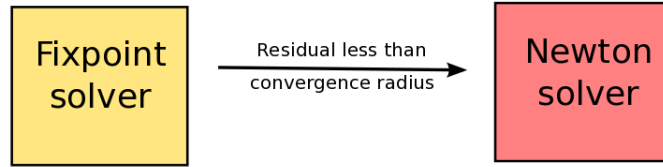


**Figure 6:** Initial strategy of the Adaptive Newton solver

For a successful convergent result we represent the solver statistics as 'a+b', where there are 'a' number of partial Fixed Point sweeps and 'b' number of full Newton sweeps. The simulation is done on level 2 with the tolerance limit of  $1E - 12$  and the other physical parameters are taken as:  $\eta_0 = 1E - 3$ ,  $\epsilon = 0.01$ .

$\varepsilon$	$\tau_0 = 0.001$	$\tau_0 = 0.01$	$\tau_0 = 0.1$	$\tau_0 = 0.5$	$\tau_0 = 1.0$
1E-1	osci	osci	osci	osci	23+6
1E-2	osci	osci	22+5	24+5	24+6
1E-3	osci	15+5	23+5	29+3	37+4
1E-4	6+5	16+4	45+4	83+3	103+3
1E-5	9+4	28+3	79+3	142+2	170+2
1E-6	14+3	44+2	112+2	201+2	239+2

**Table 1:** Number of partial and full Newton iterations for Bingham fluid

**Remarks:**

1. We can clearly see that the problem becomes harder with the increase of yield stress  $\tau_0$ , as the number of nonlinear iterations are more for a higher yield stress.
2. For a fixed  $\tau_0$ , there is a threshold value of the convergence radius  $\varepsilon$  and if the conversion from the partial Fixed Point to full Newton takes place with the residual value more than this threshold value, the solver will always fail to converge (or it oscillates in other words).
3. It is expected that if the conversion takes place at two different values  $\varepsilon_1$  and  $\varepsilon_2$  with  $\varepsilon_1 > \varepsilon_2$ , the later will always take more number of iterations to converge, as the Fixed Point is slow and the solver is in this state for more time.

**4.3.2 Phase 2**

Next we try to improve our solver by allowing  $\delta^i$  to have also more intermediate values. We start with an initial  $\delta_{initial}^i$  value and if the  $Q_n = (Res_{new}/Res_{old})$  is less than 1, we multiply  $\delta^i$  with an increment factor and if the  $Q_n$  is more than 1, we multiply  $\delta^i$  with an decrement factor. We stop the increment when  $\delta^i$  reaches 1.

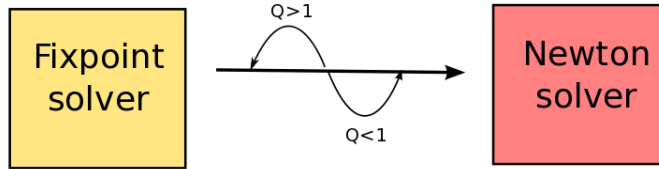


**Figure 7:** Intermediate strategy of the Adaptive Newton solver

Here we do not stick to a particular  $\delta_{initial}^i$ , as we can take any prescribed value. However we fix the maximum initial value to be 0.6. We experiment with several pairs of the increment and decrement factor and here we present the scenario, where they are 1.2 and 0.8 respectively. So mathematically

$$\frac{\delta_{n+1}}{\delta_n} = \begin{cases} 1.2 & \text{if } Q_n < 1.0 \\ 0.8 & \text{if } Q_n \geq 1.0 \end{cases} .$$

$\delta_{initial}^i$	$\tau_0 = 0.001$	$\tau_0 = 0.01$	$\tau_0 = 0.1$	$\tau_0 = 0.5$	$\tau_0 = 1.0$
0.1	15	21	osci	21	20
0.2	13	osci	osci	20	21
0.3	12	23	osci	32	18
0.4	12	osci	25	77	osci
0.5	11	14	osci	19	19
0.6	11	osci	21	98	95

**Table 2:** Nonlinear iterations of the intermediate Adaptive Newton solver for Bingham fluid

**Remarks:**

1. Definitely the behavior of the solver improves for the harder problems (high  $\tau_0$ ).
2. There are some cases where it fails to converge. However given the characteristic of the strategy, it is difficult to pinpoint the exact reason.

**4.3.3 Phase 3**

Now we prefer to smoothen the factor and hence we came up with the idea of expressing the factor as a (almost)-piecewise continuous function. Here also we try several combinations of different functions and show the results with a particular piecewise continuous function. As the  $Q_n$  can take the values between  $(0, \infty)$ , the particular domain is divided into 3 subdomains -  $(0, 0.8)$ ,  $(0.8, 1)$  and  $(1, \infty)$  and instinctively we can say that the function will be mostly decreasing in nature. As the small value of  $\delta_n$  means that the

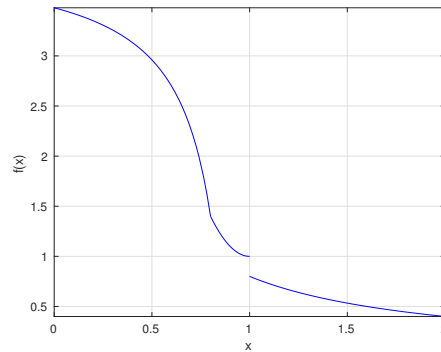


**Figure 8:** Visualization of Phase 3

solver is going in the right direction, we keep a range of high value of  $(3.48, 1.4)$  in the first interval with a hyperbolic function. Next when  $\delta_n$  is close to 1, that means that the convergence rate is not so good and we use a slow decreasing quadratic function for the range  $[1.4, 1)$  in the second interval. Now as  $Q_n > 1$  means that the solver is going in the wrong direction, we use a rapidly decreasing hyperbolic function in the third interval. We had to leave the continuity around the point 1, as we wanted to make it strongly decreasing on the right side and it has to be more than 1 on the left side, because  $Q_n < 1$  means that the solver is going in the right

direction. Mathematically it is expressed as:

$$\frac{\delta_{n+1}}{\delta_n} = \begin{cases} 4 + \frac{0.52}{(Q_n-1)} & \text{if } Q_n < 0.8 \\ 1 + 10(Q_n - 1)^2 & \text{if } 0.8 \leq Q_n < 1.0 \\ \frac{0.8}{Q_n} & \text{if } 1.0 \leq Q_n . \end{cases}$$

$\delta_{initial}^i$	$\tau_0 = 0.001$	$\tau_0 = 0.01$	$\tau_0 = 0.1$	$\tau_0 = 0.5$	$\tau_0 = 1.0$
0.1	11	21	57	40	39
0.2	11	17	40	34	34
0.3	10	22	36	34	33
0.4	osci	19	35	33	30
0.5	16	20	33	19	32
0.6	20	24	32	32	31

**Table 3:** Nonlinear iterations of the pre-Adaptive Newton solver for Bingham fluid

**Remarks:**

1. Clearly we can see that this variant of the solver is much more stable compared to the previous versions, as the number of iterations have decreased by a big margin overall.
2. It also encourages us to find a continuous version of the increment/decrement factor, so that it would be more elegant.

**4.3.4 Phase 4**

As stated previously, this is the final version of our Adaptive Newton solver and the solver swings back and forth between the Fixed point state and the Newton state continuously implicitly in this variant. The third version showed the possible shape of the function and it comes out that the function of the family  $f(x) = d + \frac{a}{b+\exp(cx)}$  shows significant saturation on the left side and rapid decrement on the right side of the interval. We want to restrict the lowest value by 0.2 and so  $d = 0.2$ . It also means that when the

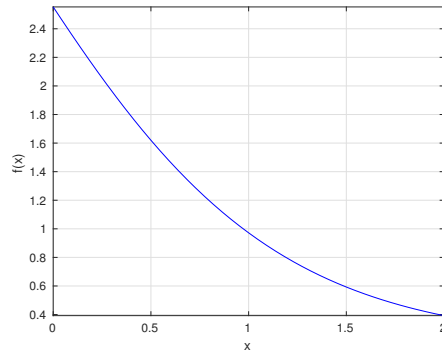


**Figure 9:** Visualization of Phase 4

solver shows no convergence (or is unstable in words),  $\delta_n$  is reset to 0.2. After a few experiments we come up with the restrictions  $f(0) = 2.5, f(0.8) = 1.2$  and  $f(1) = 0.97$  and the values of  $a, b$  and  $c$  are obtained from them after rounding off as in this particular set  $a = 4, b = 0.7, c = 1.5$  and  $d = 0.2$ . The function  $f(x)$  is expressed in the below:

$$\frac{\delta_{n+1}}{\delta_n} = f(Q_n) = 0.2 + \frac{4}{0.7 + \exp(1.5Q_n)}, \quad (4.12)$$

$$\text{where } Q_n = \frac{\|Res_n\|}{\|Res_{n-1}\|}. \quad (4.13)$$

Now we present the convergence statistics and we can see that for all the different choices of  $\delta_{initial}^i$  and  $\tau_0$ , we are able to get convergent behaviour of our solver.

$\delta_{initial}^i$	$\tau_0 = 0.001$	$\tau_0 = 0.01$	$\tau_0 = 0.1$	$\tau_0 = 0.5$	$\tau_0 = 1.0$
0.1	11	23	33	30	31
0.2	10	18	28	26	27
0.3	09	18	24	23	23
0.4	10	16	24	19	20
0.5	30	16	18	19	19
0.6	15	16	20	19	20
0.7	18	18	26	20	23
0.8	50	15	26	19	18
0.9	61	16	18	21	18
1.0	46	15	18	22	21

**Table 4:** Nonlinear iterations of the Adaptive Newton solver for Bingham fluid

Hence we can infer that we have been successful to implement the Adaptive Newton solver and next we present an example of the convergence behavior of one particular instance, namely  $\delta_{initial}^i = 0.2$  and  $\tau_0 = 0.5$ .

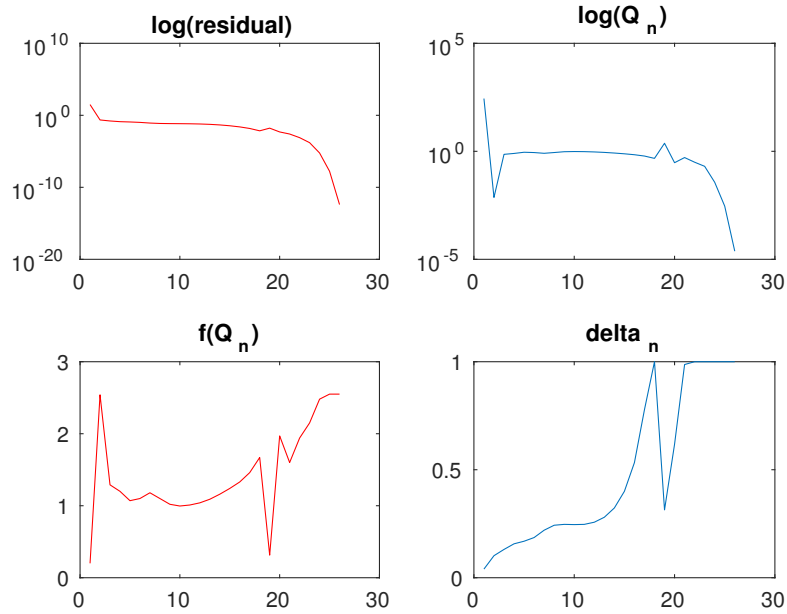


**Figure 10:** Convergence statistics of the Adaptive Newton solver for Bingham fluid with  $\tau_0 = 0.5$

We can see in Fig. 10 that the residual shows a slow but steady convergence for the first 18 nonlinear iterations due to the fact that  $\delta_n$  is very small in the beginning and  $Q_n$  also remains close to 1. Next at the 19<sup>th</sup> step,  $\delta_n$  becomes 1 for the first time. However the solver shows a bad behavior as the Jacobian is not yet ready to be used for the Full Newton solver and we can see an increase in the residual, which results in the decrement of  $\delta_n$ . However as  $Q_n$  remains less than 1,  $\delta_n$  slowly increases and become 1 again at the 22<sup>nd</sup> step. From this moment the solver stays in the Full Newton state, as it shows good convergence behavior and we can also see a rapid decrement in the residual value, resulting in to be converged in 26 iterations.

#### 4.3.5 Conclusion

If we closely look at the solver statistics for the different phases and compare them qualitatively, we can clearly see that our solver has evolved to be more stable compared to its previous version. It means that the final version of our Adaptive Newton solver is able to produce a convergent result for a large range of  $\delta_{initial}^i$  and  $\tau_0$ , whereas the first couple of versions failed to produce a convergent result for several pairs of  $\delta_{initial}^i$  and  $\tau_0$ .

Also if we compare the different phases quantitatively, it clearly shows that for the convergent

result with a particular pair of  $\delta_{initial}^i$  and  $\tau_0$ ; the number of nonlinear iterations to solve the system, i.e, the solver statistics, improves too upon the introduction of continuous function for the increment/decrement factor. Hence we can comprehensively conclude that the final version of our continuous Newton solver is both qualitatively and quantitatively more superior than its predecessors and so it is the best variant possible to be made. However we would like to mention in this context that the particular continuous function  $f(Q_n)$  is not unique and it is possible to define it in other several ways. For example, the subsequent results presented for Phase 2 in this section is computed with a different  $f(Q_n)$ :

$$\frac{\delta_{n+1}}{\delta_n} = \begin{cases} 1.1 & \text{if } Q_n < 0.5 \\ 1.05 & \text{if } 0.5 \leq Q_n < 1.0 \\ 0.8 & \text{if } 1.0 \leq Q_n . \end{cases}$$

We take the Bingham fluid with a particular yield stress  $\tau_0 = 0.5$  and regularization parameter  $\epsilon = 0.01$  in the Flow around cylinder benchmark and compare the convergence behavior for different phases of the Adaptive Newton method.

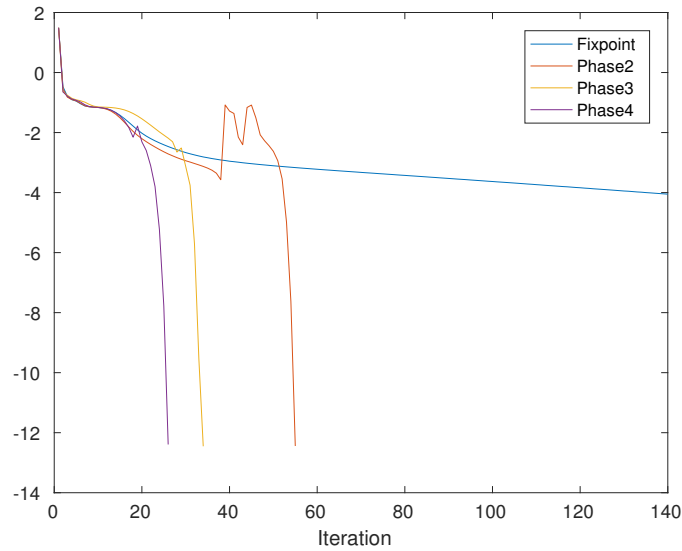


**Figure 11:** The residual convergence for the three phases of the Adaptive Newton method

We can see in Fig. 11 that the Fixed point method takes a large number (901) of iterations to get a convergent result; whereas the different phases of the Adaptive Newton solver (i.e, Phase 2, Phase 3 and Phase 4) take 55, 34 and 26 iterations respectively. Next we show the

corresponding residual improvement  $Q_n$  and the extent of Newton solver  $\delta_n$  for each version of the Adaptive Newton solver.

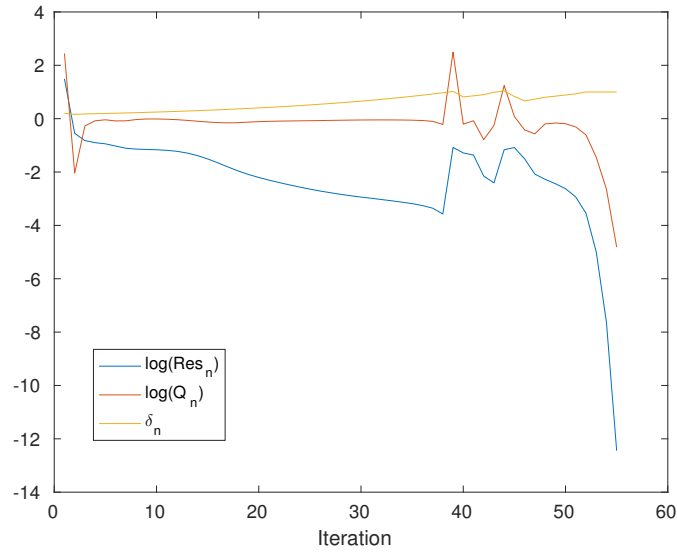


**Figure 12:** The residual  $Res_n$ , the increment  $Q_n$  and the corresponding  $\delta_n$  for Phase 2 of the Adaptive Newton method

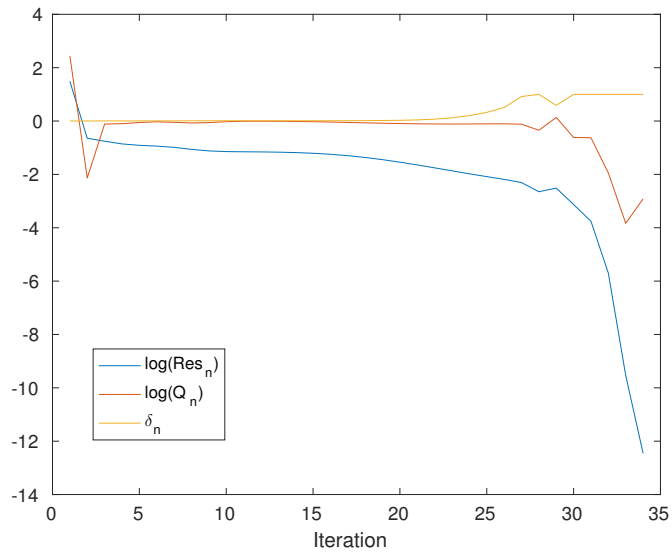


**Figure 13:** The residual  $Res_n$ , the increment  $Q_n$  and the corresponding  $\delta_n$  for Phase 3 of the Adaptive Newton method

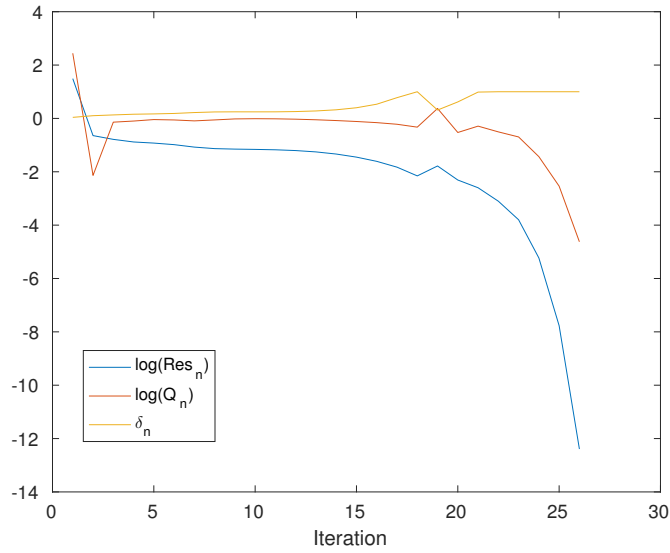


**Figure 14:** The residual  $Res_n$ , the increment  $Q_n$  and the corresponding  $\delta_n$  for Phase 4 of the Adaptive Newton method

Fig. 12-14 show similar behavior in the sense that the residual is slow but steady in the beginning, then it goes up and down for a few intermediate iterations and finally it converges rapidly at the end. When the residual increases, the  $\delta_n$  indeed decreases first and then it increases again to reach the Full Newton state. When  $\delta_n$  remains as 1 in the final iterations, the residual shows quadratic convergence as expected from a Full Newton solver. Hence we can conclude that our Adaptive Newton solver shows the characteristic as discussed in the algorithm and can handle the problems, which cannot be solved by the direct use of Full Newton solver.





## 5 Numerical Validation

This chapter is dedicated to the validation of the code [33], which is a very crucial part of the thesis. First, the well-known benchmark of Flow around cylinder [32] is described and then tests with different fluids are performed step by step towards the final target of solving quasi-Newtonian flow problems. The validation shows also the quality of the high order finite element space  $(Q_2/P_1)$  with a strong Newton solver. The benchmark is without doubt very interesting for the research and important as well for the industrial purposes.

### 5.1 Flow around cylinder benchmark

Flow around a cylinder is a popular benchmark for the evaluation of numerical algorithms for incompressible Navier-Stokes equations in the laminar case. It was developed in 1995 as part of the high-priority research program "Flow simulation on high-performance computers" funded by the German Research Association (DFG).

#### 5.1.1 Geometry

Here we take a cylinder and put it in a rectangular channel at a fixed position. Now we let a fluid with a specific density flow from one of the narrow boundaries. The other boundaries are being kept generally as 'do nothing' boundary condition. Then we calculate the drag and the lift, the body-force experienced by the cylinder due to the flow of the fluid. For the simplicity purpose, we will stick to the 2D version of it, where it is considered as a circle placed in a laminar channel.

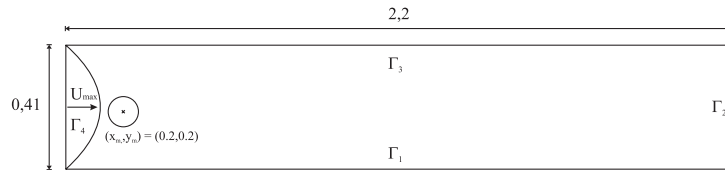


**Figure 15:** Geometry for the 'flow around cylinder' configuration

The geometry of the benchmark consists of a simple channel of length 2.2 and height 0.41. At  $(x, y) = (0.2, 0.2)$  a cylinder with diameter  $L = 0.1$  is placed. The left wall is set to a parabolic inflow profile with maximum inflow velocity  $U = 0.3$ , which can be prescribed as:

$$(u_1, u_2) = \left( \frac{4Uy(0.41 - y)}{0.41^2}, 0 \right) \quad \forall (x, y) \in [0] \times [0, 0.41] .$$

It is prescribed as Dirichlet-0 boundary conditions on the upper and lower wall and the cylinder with  $(u_1, u_2) = (0, 0)$  and the boundary conditions on the right wall is 'do nothing' boundary conditions. We can calculate the Reynolds number, Drag coefficient and the Lift coefficient for this benchmark setup as:

$$Re = \frac{U_{mean}L}{\eta} = 20, \quad C_D = \frac{2F_D}{\rho U_{mean}^2 L}, \quad C_L = \frac{2F_L}{\rho U_{mean}^2 L} .$$

$F_D$  and  $F_L$  are defined by:

$$F_D = \int_S \left( \rho \eta \frac{\partial u_t}{\partial \bar{n}} n_y - p n_x \right) dS, \quad F_L = - \int_S \left( \rho \eta \frac{\partial u_t}{\partial \bar{n}} n_x + p n_y \right) dS,$$

where  $S$  is the surface of the cylinder and  $\bar{n}$  is the normal vector of  $S$ .

### 5.1.2 Mesh specification

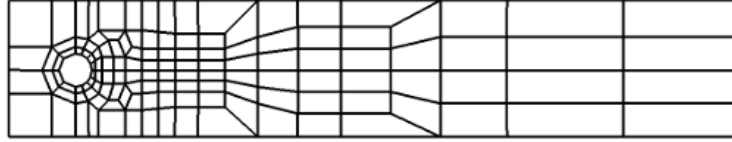


**Figure 16:** Coarse grid (level 1) for the 'flow around cylinder' configuration

We take the mesh presented above as the coarse mesh and refine it for the subsequent levels. The element statistics is presented in the table, where NEL, NVT and NMP represent the number of elements, vertices and mid points and Unknowns represents the total number of unknowns for  $Q_2/P_1$  discretization.

Level	NEL	NVT	NMP	Unknowns
L1	130	156	286	1533
L2	520	572	1092	5927
L3	2080	2184	4264	23295
L4	8320	8528	16848	92351
L5	33280	33696	66976	367743

**Table 5:** Element statistics for the bench1 mesh

## 5.2 Convergence Statistics

Now we let different kind of fluids flow in the geometry (Fig. 15) with the specified boundary conditions and here we present the convergence statistics.

### 5.2.1 Newtonian flow

First we let a Newtonian fluid flow with viscosity  $\eta = \eta_0 = 0.001$  ( $Re=20$ ) and the reference value of Drag and Lift values for it are found to be 5.579535 and 1.061894E-02 respectively [30].

Level	Drag		Lift		Solver Statistics	
	Fixed Point	Newton	Fixed Point	Newton	Fixed Point	Newton
3	5.572228E+00	5.572234E+00	1.060067E-02	1.059862E-02	11/3	3/2
4	5.577628E+00	5.577649E+00	1.061565E-02	1.061018E-02	10/2	3/1
5	5.579065E+00	5.579143E+00	1.061781E-02	1.063458E-02	9/2	2/1

**Table 6:** Numerical results of full Newton solver for Newtonian fluid

### 5.2.2 Shear thinning fluid

Then we simulate the results for a shear thinning fluid, where the viscosity is represented as:  $\eta = \eta_0(|\dot{\gamma}|^2 + \epsilon)^{\frac{m}{2}-1}$ , where  $\eta_0 = 10^{-3}$ ,  $\epsilon = 0.1$ ,  $m = 1.5$ . The reference value of Drag and Lift values for this model are 3.27833 and -0.01332 respectively [30].

Level	Drag		Lift		Solver Statistics	
	Fixed Point	Newton	Fixed Point	Newton	Fixed Point	Newton
3	3.229269E+00	3.229259E+00	-1.313980E-02	-1.314073E-02	32/3	4/2
4	3.266370E+00	3.266363E+00	-1.334047E-02	-1.334371E-02	29/3	3/2
5	3.275334E+00	3.275314E+00	-1.330595E-02	-1.331410E-02	26/3	3/2

**Table 7:** Numerical results of full Newton solver for shear thinning fluid

### 5.2.3 Shear thickening fluid

Next we let a shear thickening fluid flow, where the viscosity takes the form:  $\eta = \eta_0(|\dot{\gamma}|^2 + \epsilon)^{\frac{m}{2}-1}$ , where  $\eta_0 = 10^{-3}$ ,  $\epsilon = 0.1$ ,  $m = 3$ . The reference value of Drag and Lift values for this model are 13.8271 and 0.3529 respectively [30].

Level	Drag		Lift		Solver Statistics	
	Fixed Point	Newton	Fixed Point	Newton	Fixed Point	Newton
3	1.386694E+01	1.386694E+01	3.518391E-01	3.518386E-01	14/7	3/2
4	1.383631E+01	1.383630E+01	3.515629E-01	3.515616E-01	13/5	3/1
5	1.382972E+01	1.382967E+01	3.526886E-01	3.526851E-01	12/4	3/1

**Table 8:** Numerical results of full Newton solver for shear thickening fluid

### 5.2.4 Bingham Fluid

Lastly we consider the case of the Bingham fluid, which is conceived of as the simplest model used to describe the viscoplastic fluid behavior. The constitutive law is characterized by a flow curve which is a straight line having an intercept  $\tau_0$  on the shear stress axis. We take the regularized viscosity models to approximate the viscosity to be a smooth and differential function. The reference value of Drag and Lift values for this model are 3.499933E3 and 3.094673E1 respectively [31]. The viscosity is represented as:  $\eta = \eta_0 + \frac{\sqrt{2}}{2}\tau_0(|\dot{\gamma}|^2 + \epsilon)^{-\frac{1}{2}}$ , where  $\eta_0 = 1, \epsilon = 0.01, \tau_0 = 0.5$ .

Level	Drag		Lift		Solver Statistics	
	Fixed Point	Newton	Fixed Point	Newton	Fixed Point	Newton
3	3.492406E+03	3.492406E+03	3.152649E+01	3.152649E+01	17/2	4/2
4	3.497411E+03	3.497411E+03	3.153195E+01	3.153195E+01	17/2	3/2
5	3.499157E+03	3.499157E+03	3.158351E+01	3.158351E+01	16/2	2/3

**Table 9:** Numerical results of full Newton solver for Bingham fluid

### 5.2.5 Conclusion

We can see in Tables 6-9 that the calculated Drag and Lift values match with their respective reference values for 4 different fluids and they tend to show convergence behavior on successive refinements. Also from the point of view of the solvers, we can say that the Full Newton solver is much faster compared to the Fixed point solver and hence one can use Full Newton method for these kind of fluids in the Flow around cylinder benchmark problem.

### 5.3 Adaptive Newton solver

Next we have try to solve the Bingham fluid with the parameter  $\eta = 1E - 3$  instead of  $\eta = 1$ , but suprisingly we come across a peculiar difficulty. Our studies show that the current problem is solvable with the Fixed point slover, which is linear in behaviour; but whenever we want to have a 'pure' Newton solver to make it faster, which is quadratic in behaviour (locally); unfortunately the solver failed to converge. So we develop an adaptive version of the Newton method based on the direct calculation of the Jacobian and the explicit accessibility to the Jacobian allows the adaptive treatment of it. Firstly a robust Newton method is made with respect to the initial guess and then an efficient linear solver is applied due to selective strategy of the nonsingular part of the Jacobian. We use the weighing parameter  $\delta_n$  in order to balance the operators  $A_1$  (corresponding to the typical fixed point approach) and  $A_2$ , both being part of the complete Jacobian  $A$  in Eq. 4.9:

$$A = A_1 + \delta_n A_2 . \quad (5.14)$$

In the present note, we concentrate on the choice of the optimal weighing parameter  $\delta_n$  balancing the fixed point and the full Newton iteration. We set the standard tolerance limit as  $1E - 8$  and we take the classical flow around cylinder benchmark and perform corresponding simulations for Bingham flow. First, we take a very small yield stress parameter,  $\tau_0 = 10^{-4}$ , and apply the Fixed point ( $\delta_n = 0$ ) and classical Newton ( $\delta_n = 1$ ) methods. Both the Newton and the fixed point methods easily converges towards the solution and moreover, the Newton method overcomes the fixed point method, as expected, due to the moderate nonlinearity. To highlight the insufficiency of the globally damped Newton to simulate Bingham flow problems, we further increase the yield stress. Now, the Newton method can only converge with a strong damping parameter  $\omega_n$  as the yield stress increases, for instance  $\omega_n = 0.1$  for  $\tau_0 = 10^{-2}$ , and no convergence at all can be obtained for higher yield stress,  $\tau_0 \geq 10^{-1}$ . Instead, the fixed point method can converge for all cases, however being very slow and not being robust w.r.t. mesh level and/or yield stress.

	$\tau_0 = 1E - 4$		$\tau_0 = 1E - 3$		$\tau_0 = 1E - 2$		$\tau_0 = 1E - 1$	$\tau_0 = 1$
Level	FP	Newton	FP	Newton	FP	Newton	FP	FP
2	21	3	67	99	212	210	490	1032
3	24	5	84	95	308	200	728	2135
4	20	5	98	90	408	190	1375	3444

**Table 10:** The number of NL iterations for Bingham flow for increasing yield stress

Clearly, with increasing yield stress (Table 10), it is hard if not impossible to solve the corresponding flow problems with the globally damped Newton. Therefore, in the next step, we take a static  $\delta_n$ , i.e.  $\delta_n = \delta_0$  for  $n \geq 1$ . The balancing parameter  $\delta_n$  is taken as a constant increasing from 0 to 1. Next we present the numbers of nonlinear iterations for Bingham flow with different values for the yield stress.

Level	$\tau_0 = 1E - 2$				$\tau_0 = 1E - 1$			
	$\delta_0 = 0.1$	$\delta_0 = 0.25$	$\delta_0 = 0.5$	$\delta_0 = 0.6$	$\delta_0 = 0.1$	$\delta_0 = 0.25$	$\delta_0 = 0.5$	$\delta_0 = 0.6$
2	236	198	135	110	551	461	311	251
3	352	295	199	160	848	708	475	382
4	455	380	256	206	1455	1214	813	653

**Table 11:** The number of NL iterations for Bingham flow for increasing yield stress

From the results in Table 11, it is clear that increasing the contribution from the operator  $A_2$  improves the convergence behavior, but this contribution needs to remain under control. To do so, we go for a dynamic change of  $\delta_n$  w.r.t. the residual changes. From the numerical experiment it can be noticed that the dynamic changes of the residual give a precious information about the singularity of the Jacobian. Indeed, the larger relative changes in the residual with the operator  $A_1$  reflect the ‘singularity’ of the operator  $A_2$ . In this case, the parameter  $\delta_n$  should have a small relative change and remain small. Moreover, when the relative changes in the residual are close to zero, this indicates that the operator  $A_2$  has the nicest properties and  $\delta_n$  can be increased accordingly and maintained close to 1.

We recall the previously defined characteristic function  $f(Q_n)$  in Eq. 4.13 and point out again that the choice of  $f(Q_n)$  is derived so far based on simple and preliminary numerical experiments only. We check the robustness of the dynamic changes of  $\delta_n$ , as the numbers of nonlinear iterations for Bingham flow for a wide range of yield stress values and different starting weighing parameters  $\delta_0$  for the Jacobian in Table 12.

$\delta_0$	$\tau_0 = 1E - 2$						
	0.001	0.01	0.1	0.5	1.0	2.0	5.0
0.0	10	15	20	19	19	20	20
0.3	10	16	20	19	19	20	20
0.7	18	18	22	22	20	18	18
1.0	46	14	19	21	21	22	22

**Table 12:** The number of NL iterations for Bingham flow for wide range of yield stress

Since the convergence typically gets harder with smaller values for the regularization parameter  $\epsilon$ , we check the robustness of the dynamic changes of  $\delta_n$  for decreasing  $\epsilon$  and a wide range of yield stress values. Next we show the numbers of nonlinear iterations for Bingham flow using continuation strategies w.r.t.  $\epsilon$  as well as w.r.t.  $\tau_0$  in Table 13.

		$\tau_0$						
	$\epsilon$	0.001	0.01	0.1	0.5	1.0	2.0	5.0
Continuation w.r.t. $\epsilon$	1E-2	10	15	20	19	19	20	20
	1E-3	11	11	12	17	16	15	15
	1E-4	15	13	18	16	15	26	15
	1E-5	16	10	22	22	17	15	17
Continuation w.r.t. $\tau_0$	1E-2	10	14	19	12	8	7	7
	1E-3	14	20	26	15	8	8	8
	1E-4	21	26	34	23	10	17	8
	1E-5	22	45	41	29	11	10	10

**Table 13:** The number of NL iterations for Bingham flow for wide range of yield stress



## 6 Application

The range of practical real world problems which involve granular materials is growing and since the considered problems become more complex and experimentally more expensive, one is particularly interested in the development of new and more powerful computational methods for solving these problems numerically. In this section we show that our Adaptive Newton strategy based on FEM techniques is well suited to address the illustrated type of nonlinear powder problems and lead to comparative results with related experiments. We consider the following configuration, powder flow in a Couette device as shown in Fig. 17.

### 6.1 Geometry

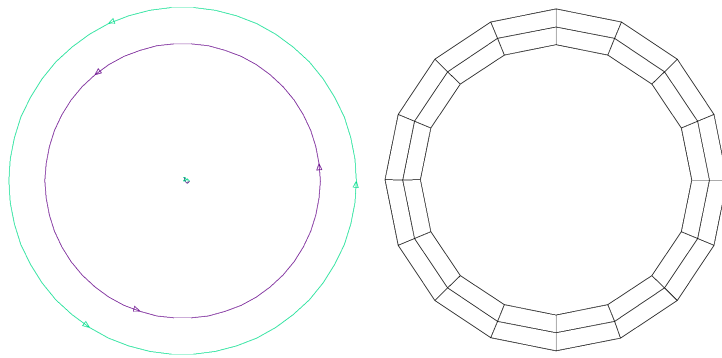


**Figure 17:** Geometry and used mesh (level 1) for Couette flow

Here we want to study the flow of granular materials in the 2D version of a couette configuration and we use a hydrostatic pressure parameter  $P$  instead of pressure  $p$  in the Poliquen model 3.3. We assume that  $P$  has a constant value on the whole domain and hence we claim that a (modified) Poliquen model 6.15 is used as the viscosity formulation. We take the circular channel between two concentric circles of radii 19 mm and 24 mm as the computational domain and use the 'no-slip' boundary condition on the perimeters of both the circles. The inner circle is rotated at 10 rpm, while the outer one is kept at rest. Next we present the complete model formulation, which is used for solving this benchmark problem.

## 6.2 Mathematical formulation

We take the generalized Navier Stokes equation as:

$$\begin{aligned} \rho \frac{Du}{Dt} &= -\nabla p + \nabla \cdot \sigma && \text{in } \Omega \\ \text{with } \nabla \cdot u &= 0 && \text{in } \Omega, \end{aligned}$$

where  $\rho$ ,  $u$  and  $p$  are the density, velocity and pressure of the fluid medium on the continuous level,  $\frac{D}{Dt}$  represents the material derivative and  $\sigma$  is the stress tensor in the domain  $\Omega$ . Now we express  $\sigma = 2\eta\dot{\gamma}$ , where  $\eta$  is the viscosity and  $\dot{\gamma} = \frac{1}{2}(\nabla u + \nabla u^T)$  is the shear rate. Then, the NS equation reads as:

$$\rho \frac{Du}{Dt} = -\nabla p + \nabla \cdot (2\eta\dot{\gamma}), \quad \nabla \cdot u = 0 \quad \text{in } \Omega .$$

### 6.2.1 Governing Parameters

In our model,  $\eta$  is expressed as:

$$\eta = \frac{\sqrt{2}}{2} \tau_0 \left( \frac{\alpha}{|\dot{\gamma}|} + \frac{\beta d}{\delta \sqrt{\frac{P}{\rho} + |\dot{\gamma}|d}} \right) P . \quad (6.15)$$

Additionally, we introduce a regularization parameter (here:  $\epsilon = 0.01$ ) in the denominator as  $\sqrt{|\dot{\gamma}|^2 + \epsilon^2}$ . Now we set:

$$\begin{aligned} \alpha &= 0.15, & \beta &= 0.27, & \delta &= 0.06, \\ P &= 1487Nm^{-2}, & d &= 0.001m, & \rho &= 1500kgm^{-3}, \\ r_1 &= 0.019m, & r_2 &= 0.024m . \end{aligned}$$

We put  $\tau_0 = \sqrt{2}$  to make the initial factor as unity. Moreover, the velocity of the inner couette is prescribed as 10 rpm, which is changed to the SI unit by the following conversion:

$$|u| = 10rpm = \frac{1}{6}rps = \frac{2\pi r_1}{6}m/s = \frac{2\pi 0.019}{6}m/s = 0.019886667m/s .$$

### 6.2.2 Non-dimensionalization

Next, we convert the parameters into dimensionless quantities. One way to reach the non-dimensionalization is to set the given  $\rho$  as unity. So, we change our mass unit in such a way that the effective  $\rho$  becomes unity. Among the other parameters, only P contains the mass

unit and so it is also changed to  $1487/1500 = 0.99133$ . Finally, the new modified parameters are:

$$\begin{aligned} \alpha &= 0.15, & \beta &= 0.27, & \delta &= 0.06, \\ P &= 0.99133, & d &= 0.001, & \rho &= 1, \\ r_1 &= 0.019, & r_2 &= 0.024 . \end{aligned}$$

### 6.2.3 Final model

After putting all the numerical values of the parameters described in the previous section, we can write our final model of the NS equation and the corresponding viscosity formulation as:

$$\begin{aligned} \frac{Du}{Dt} &= -\nabla p + \nabla \cdot (2\eta\dot{\gamma}), \quad \nabla \cdot u = 0 && \text{in } \Omega \\ \text{where } \eta &= \left( \frac{0.1487}{\sqrt{|\dot{\gamma}|^2 + \epsilon^2}} + \frac{0.26766}{59.7394 + \sqrt{|\dot{\gamma}|^2 + \epsilon^2}} \right), \\ \dot{\gamma} &= \frac{1}{2}(\nabla u + \nabla u^T), \quad |\dot{\gamma}| = \sqrt{\dot{\gamma} : \dot{\gamma}} = \sqrt{\text{tr}(\dot{\gamma}^2)} \quad \text{and } \epsilon = 0.01 . \end{aligned}$$

As (Dirichlet) boundary conditions the tangential velocity components are prescribed with  $|u| = 0.019886667$  on the perimeter of the inner circle and  $|u| = 0$  (no slip) on the perimeter of the outer circle.

## 6.3 Results

We use the above discussed model in our Finite element software Featflow [32] and in the Finite volume software Openfoam in Freiberg. While solving the problem in Featflow, we take a different characteristic function  $f(Q_n)$  in contrast to the one mentioned in [27]. We express the new function as:

$$f(Q_n) = 0.2 + \frac{17.694}{8.83 + \exp(2.608Q_n)} .$$

The reason of choosing this particular  $f(Q_n)$  can be found in section 8 and next we present the comparisons between the Dortmund and Freiberg results.

### 6.3.1 Dortmund results with Umfpack and MG

Level	NEL	NVT	NMT	Unknowns	NL	CPU/UMF	NL/MG	CPU/MG	NL/MG	CPU/MG
					$\epsilon = 1E - 2$		$\epsilon = 1E - 2$		$\epsilon = 1E - 3$	
L1	32	48	80	415						
L2	128	160	288	1535	20	1	21/1	1.5	37/1	2.85
L3	512	576	1088	5887	21	11	22/3	15	32/2	42
L4	2048	2176	4224	23039	17	102	15/1	25	22/1	65
L5	8192	8448	16640	91135	15	2958	16/2	154	24/1	319
L6	32768	33280	66048	362495	20	67163	21/2	1012	21/1	1425
L7	131072	132096	263168	1445887	13	545700	25/2	5483	23/2	7866

**Table 14:** Statistics for the Dortmund results

As the number of nonlinear iterations are mostly around 20-25, we can say that the solver shows a stable behavior. When we solve the problem with Umfpack, we can see a steady increase in the CPU time for each level. However when we use the multigrid solver, there is a significant improvement for CPU time for the finer meshes. So we can conclude that the multigrid method takes more time in the coarser mesh. However when we want to solve the problem more accurately, multigrid method seem superior compared to Umfpack method starting from level 4.

### 6.3.2 Detailed results for multigrid solver

Here we represent the detailed results of the Multigrid solver with the regularization parameter  $\epsilon = 1E-2$  and  $1E-3$ . The number of smoothing steps is 15 and maximum number of iterations for a multigrid cycle is taken as 10. In this context we would like to mention that it is also possible to solve the problem with 7 smoothing steps for  $\epsilon = 1E - 2$ . However as  $\epsilon = 1E - 3$  makes the problem harder, it needs 15 smoothing steps for this case and so the number of smoothing steps is taken as 15 to have a relevant comparison between two regularization parameters.

Level	MG gain $1E-1$				MG gain $1E-2$			
	$\epsilon = 1E-2$		$\epsilon = 1E-3$		$\epsilon = 1E-2$		$\epsilon = 1E-3$	
	NL/MG	CPU/MG	NL/MG	CPU/MG	NL/MG	CPU/MG	NL/MG	CPU/MG
L1	10	0.2			10	0.2		
L2	20/1	2	34/1	3.5	20/1	2	33/1	3.5
L3	21/1	12	32/2.5	43	21/1.5	14	32/3	43
L4	15/1	40	22/1	69	16/1	44	29/2	115
L5	16/1	215	24/1	323	16/2	244	27/1.5	426
L6	21/1.5	1476	21/1.5	1363	20/2	1481	21/2	2029
L7	24/1.5	7671	23/1.5	8176	23/1.5	6353	28/2	11534

**Table 15:** Convergence statistics for multigrid gain  $1E-1$  and  $1E-2$

Level	MG gain $1E-3$				MG gain $1E-4$			
	$\epsilon = 1E-2$		$\epsilon = 1E-3$		$\epsilon = 1E-2$		$\epsilon = 1E-3$	
	NL/MG	CPU/MG	NL/MG	CPU/MG	NL/MG	CPU/MG	NL/MG	CPU/MG
L1	10	0.2						
L2	20/1.5	4	33/1	3.8	20/1.5	4.3	33/2	4.7
L3	21/2	27	32/3.5	48	21/2.5	38	32/4	56
L4	17/2	133	20/2	100	17/3	163	55/3.5	387
L5	15/2	440	26/2.5	686	15/3	923	26/4	922
L6	20/2	3612	21/3	2904	20/3.5	5348	21/5	3841
L7	23/2	14411	28/3	12692	23/3	26817	28/4	17881

**Table 16:** Convergence statistics for multigrid gain  $1E-3$  and  $1E-4$

Overall it shows a good convergence behavior in Table 15 and 16, as the number of nonlinear iterations are not too high. If we fix  $\epsilon$  and vary the multigrid gain, the number of nonlinear iterations remains same and the average number of linear iterations increases as expected. On the other hand, we can see that the number of nonlinear iterations for a fixed multigrid gain and different  $\epsilon$  remains similar, especially for the finer meshes. However if we consider the CPU time, then we can see that keeping a low multigrid gain is preferable as it takes less time to complete the simulation and counter-intuitively it takes less time for a smaller  $\epsilon$  with a small multigrid gain ( $1E-3$  and  $1E-4$ ) on the refined levels (level 6 and 7).

### 6.3.3 Freiberg statistics

relative mesh size	cells	Unknowns	CPU time
2	900	2700	5.6
1	3600	10800	53
0.5	14400	43200	1195
0.25	57600	172800	16252
0.125	230400	691200	213700

**Table 17:** Statistics for the Freiberg results

The convergence behavior of the Freiberg results shows a similar steady increase in the CPU time for different meshes compared to the Umfpack results of Featflow. However as the multigrid method shows much superior behavior for CPU time on the finer meshes, we conclude that use of multigrid method is preferable, when we want to have more accurate results.

## 6.4 Visual Comparison

After the comparison between the CPU time of the Dortmund and Freiberg results, next we present the respective profiles of the different physical quantities, namely the velocity magnitude  $|u|$ , the modulus of the shear rate  $|\dot{\gamma}|$  and the viscosity  $\eta$ . Due to the geometrical set up and the induced boundary conditions the results show the radial symmetry as expected. Hence instead of studying the whole domain, we make a cutline of length 0.005 between the points (0.019, 0) and (0.024, 0) and plot 3 different physical quantities on the cutline on Fig. 18-21. In order to maintain the clarity and to be able to read data easily, we plot only the 3 finest levels on a particular picture.

The physical quantities for both simulations are shown on the normal scales (Fig. 18 and 20) respectively. Firstly we can see that the cutlines converge to their finest simulation respectively for both the simulations, which assures that the solution on each level has the correct convergence trend. As both  $|u|$  and  $|\dot{\gamma}|$  are very close to 0 on the right half of the domain, we also present the respective quantities in the log scales (Fig. 19 and 21). Since the leftmost point of the cutline is set to have a non-zero speed and the rightmost point is kept at rest, we can see a monotonically decreasing profile for  $|u|$  as expected and  $|\dot{\gamma}|$  shows the same tendency too. Moreover as the viscosity is inversely proportional to  $|\dot{\gamma}|$ , it shows an increasing profile as anticipated. Hence we conclude that both Dortmund and Freiberg simulations are able to capture the correct tendencies of the physical quantities for the 2D Couette flow simulation.

### 6.4.1 Dortmund results

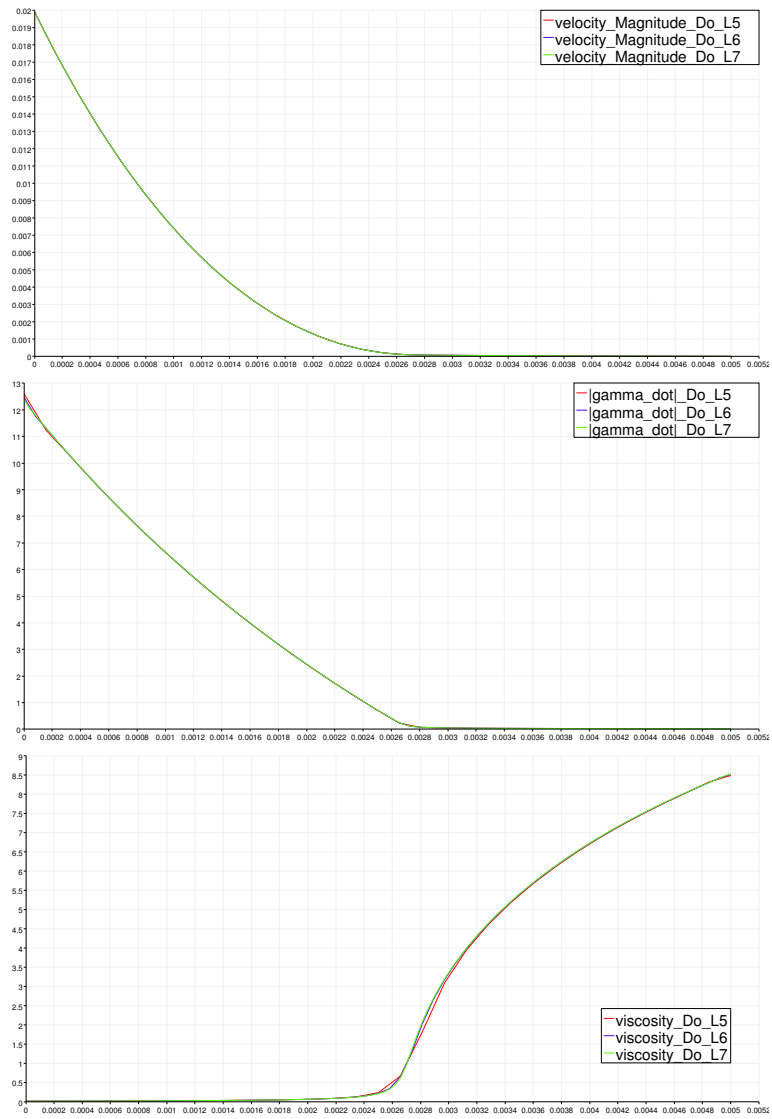


Figure 18: Normal scale

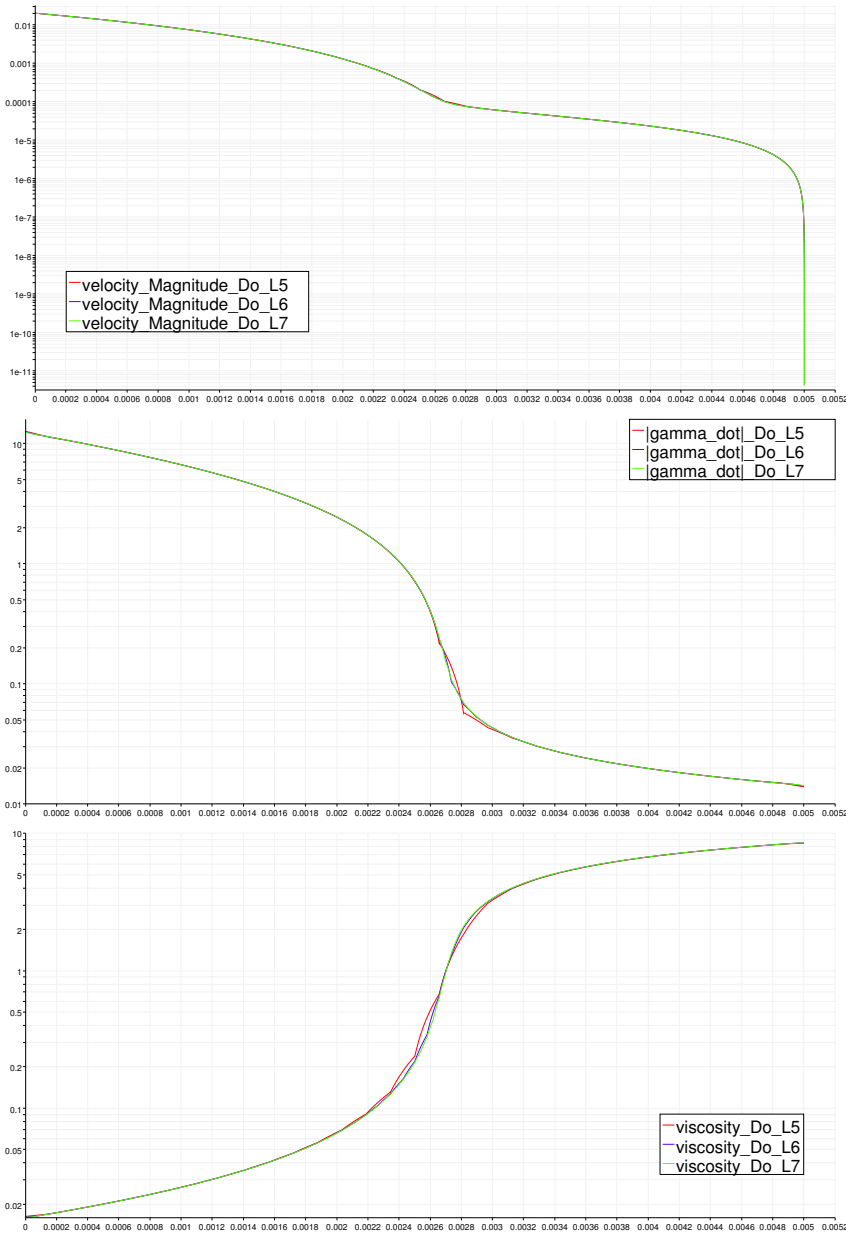


Figure 19: Log scale

## 6.4.2 Freiberg results

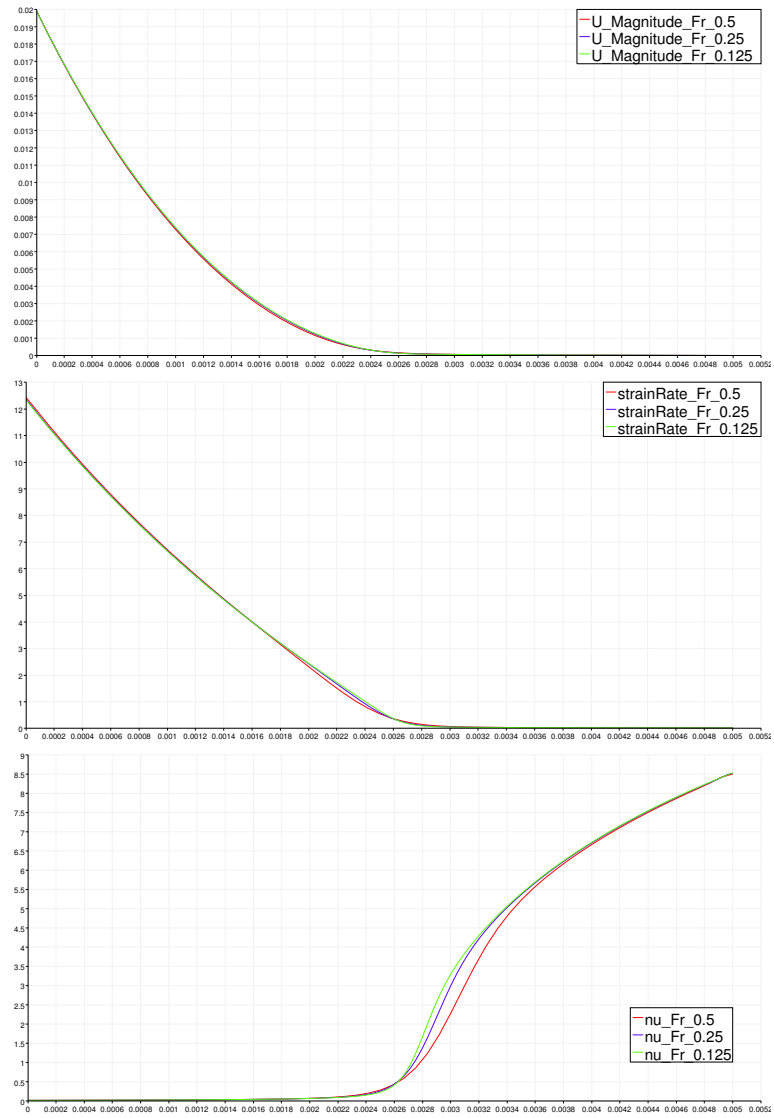


Figure 20: Normal scale

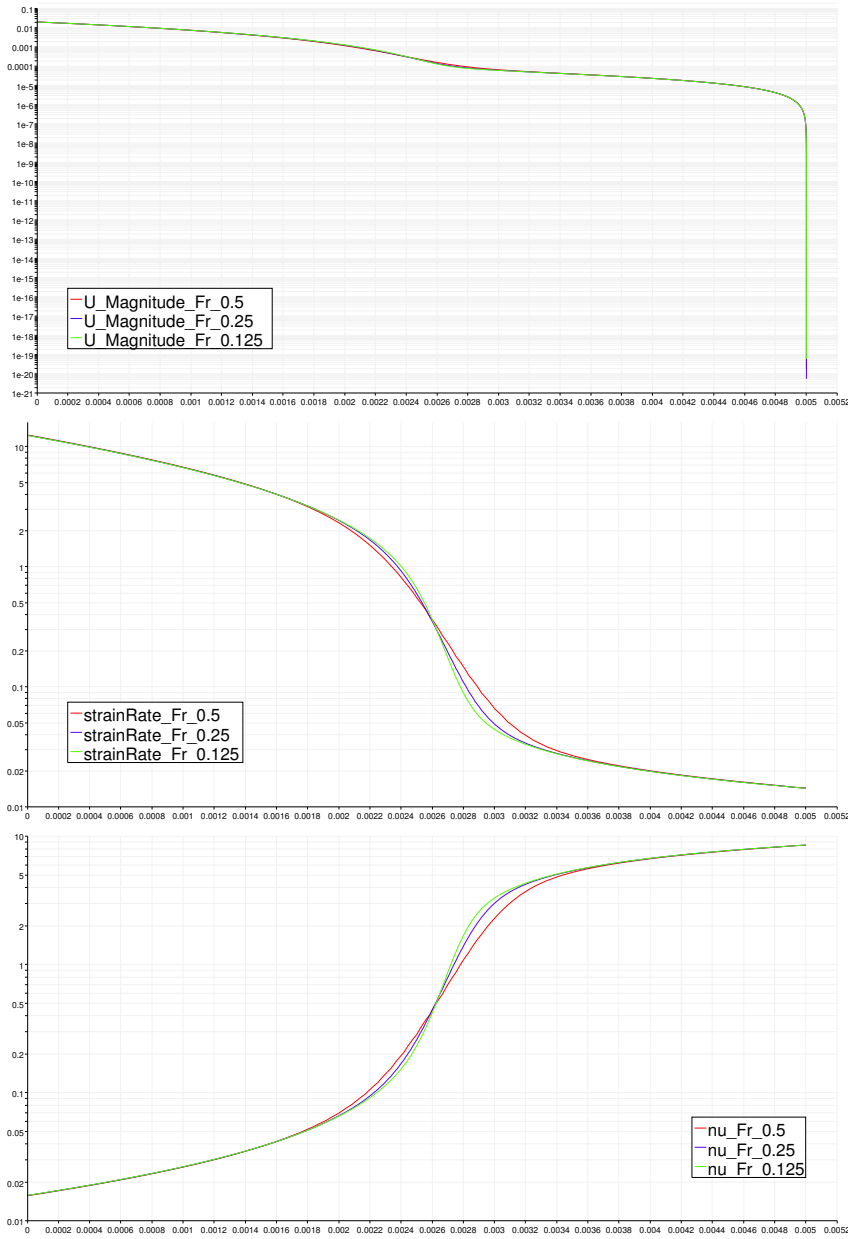


Figure 21: Log scale

## 6.5 Level Comparison

### 6.5.1 Statistical Analysis

We define the error functional  $\xi$  as:

$$\xi_{ij} = \sqrt{\frac{\int_0^{0.005} (L_i - L_j)^2 dx}{\int_0^{0.005} L_i^2 dx}} \times 100,$$

where  $L_i$  and  $L_j$  are two different lineplots. We measure the difference between 3 sets of respective physical parameters - namely velocity, shear rate and viscosity and present the error functional  $\xi$  in a percentage form in a table format with  $i$  and  $j$  corresponding to the rows and columns respectively.

		Do-12	Do-13	Do-14	Do-15	Do-16	Do-17	Fr-2	Fr-1	Fr-0.5	Fr-0.25	Fr-0.125
Do-12	$ u $	-	6.28	7.16	7.31	7.35	7.35	10.28	9.13	8.12	7.61	7.41
	$ \dot{\gamma} $	-	9.13	10.69	11.05	11.14	11.16	6.08	8.75	10.27	10.85	11.06
	$\eta$	-	20.25	24.27	26.13	26.69	26.87	16.22	17.38	23.17	25.69	26.58
Do-13	$ u $	6.56	-	1.59	1.79	1.83	1.84	5.31	3.92	2.68	2.11	1.9
	$ \dot{\gamma} $	9.6	-	3.55	4.26	4.41	4.45	5.34	4.36	4.13	4.27	4.39
	$\eta$	17.24	-	5.85	8.27	8.92	9.1	25.69	8.17	4.82	7.5	8.65
Do-14	$ u $	7.55	1.61	-	0.36	0.4	0.41	4.5	2.89	1.44	0.73	0.48
	$ \dot{\gamma} $	11.36	3.58	-	1.31	1.56	1.62	6.26	3.62	2.07	1.62	1.6
	$\eta$	20.08	5.68	-	3.13	4.04	4.28	29.21	12.49	3.53	2.01	3.49
Do-15	$ u $	7.73	1.81	0.36	-	0.083	0.093	4.4	2.72	1.24	0.48	0.19
	$ \dot{\gamma} $	11.77	4.31	1.31	-	0.45	0.54	6.56	3.68	1.77	0.88	0.61
	$\eta$	21.38	7.94	3.1	-	1	1.27	30.87	14.91	6.26	2.04	0.67
Do-16	$ u $	7.77	1.85	0.4	0.083	-	0.02	4.37	2.69	1.2	0.44	0.14
	$ \dot{\gamma} $	11.87	4.47	1.56	0.45	-	0.16	6.64	3.71	1.76	0.76	0.34
	$\eta$	21.76	8.54	3.98	1	-	0.3	31.31	15.55	7.06	2.9	0.99
Do-17	$ u $	7.78	1.86	0.41	0.093	0.02	-	4.37	2.68	1.19	0.43	0.13
	$ \dot{\gamma} $	11.9	4.51	1.62	0.54	0.16	-	6.66	3.72	1.76	0.75	0.29
	$\eta$	21.88	8.71	4.22	1.26	0.3	-	31.43	15.72	7.27	3.13	1.22

**Table 18:** Level comparison in %

We fix one Dortmund plot on a particular level  $L_i$  and calculate the error functional compared to Freiberg plots  $L_j$ . Then we find the minimum among those comparisons and deduce that the  $L_j$  with the least  $\xi$  is the closest with  $L_i$ .

For Do-L2, the minimum calculation gives (Fr-0.125, Fr-2, Fr-2).

For Do-L3, the minimum calculation gives (Fr-0.125, Fr-0.5, Fr-0.5).

For Do-L4, the minimum calculation gives (Fr-0.125, Fr-0.25/0.125, Fr-0.25).

For Do-L5, the minimum calculation gives (Fr-0.125, Fr-0.125, Fr-0.125).

If we see the physical parameters shear rate and viscosity in particular, we can say that the comparison indeed changes (almost) diagonally in the right block of Table 18 from Do-L2 to Do-L5, which is a strong sign of correlation. If it continues to show similar behavior, we expect that the minimum calculation with Do-L6 should give Fr-0.0625 and with Do-L7 should give Fr-0.03125. However due to the unavailability of the data, the minimum calculation with both Do-L6 and Do-L7 shows Fr-0.125.

Additionally if we look closely the Dortmund lineplots on different level, we can see that they converge on more refinement and practically the difference between level 6 and level 7 is very negligible. On the other hand, the Freiberg lineplots also show the behavior of getting closer to the result of Dortmund level 7. So we can safely assume that Dortmund level 7 result is the most accurate result available and therefore we take it as the reference solution.

Dortmund			Freiburg		
$\xi$	level	CPU	$\xi$	level	CPU
7.78			2.68		
11.9	Do-12	1.5	3.72	Fr-1	53
21.88			15.72		
1.86			1.19		
4.51	Do-13	15	1.76	Fr-0.5	1195
8.71			7.27		
0.41			0.43		
1.62	Do-14	25	0.75	Fr-0.25	16252
4.22			3.13		
0.093			0.13		
0.54	Do-15	154	0.29	Fr-0.125	213700
1.26			1.22		
0.02					
0.16	Do-16	1012			
0.3					

**Table 19:** Level comparison

Now if we look at the sixth block row of Table 3, we can see a striking similarity between the  $\xi$  of Do-L5 and Fr-0.125,

when they are compared with Do-L7. We also represent this particular block in Table 19 and append the respective corresponding CPU time.

### 6.5.2 Dortmund-Freiberg comparison - Part I

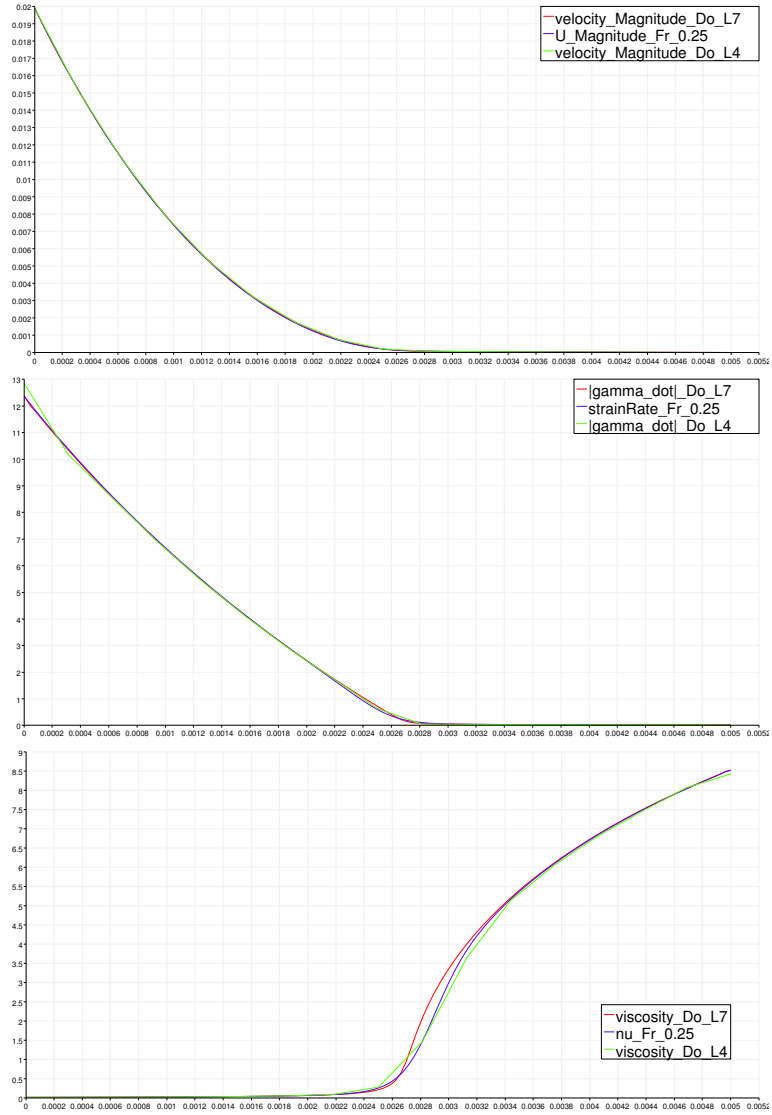


Figure 22: Normal scale

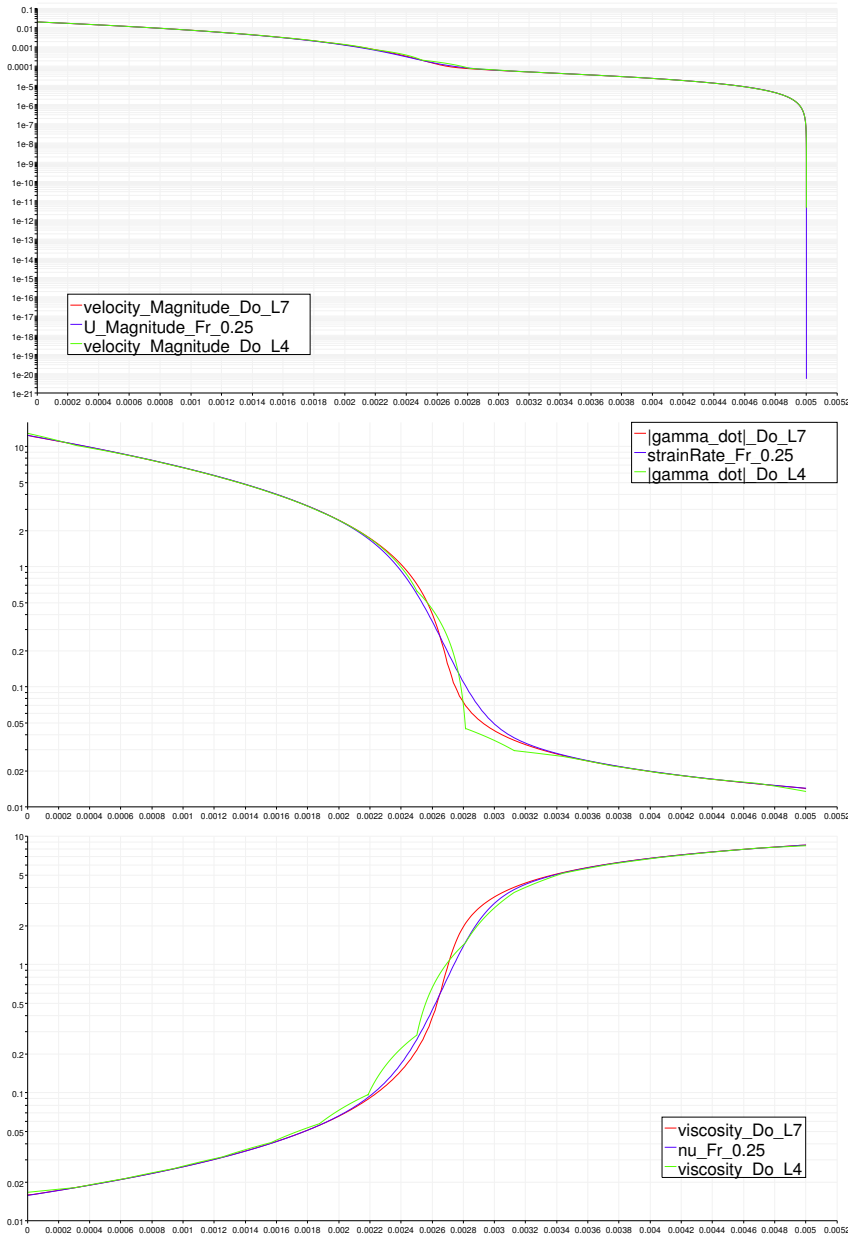


Figure 23: Log scale

### 6.5.3 Dortmund-Freiberg comparison - Part II

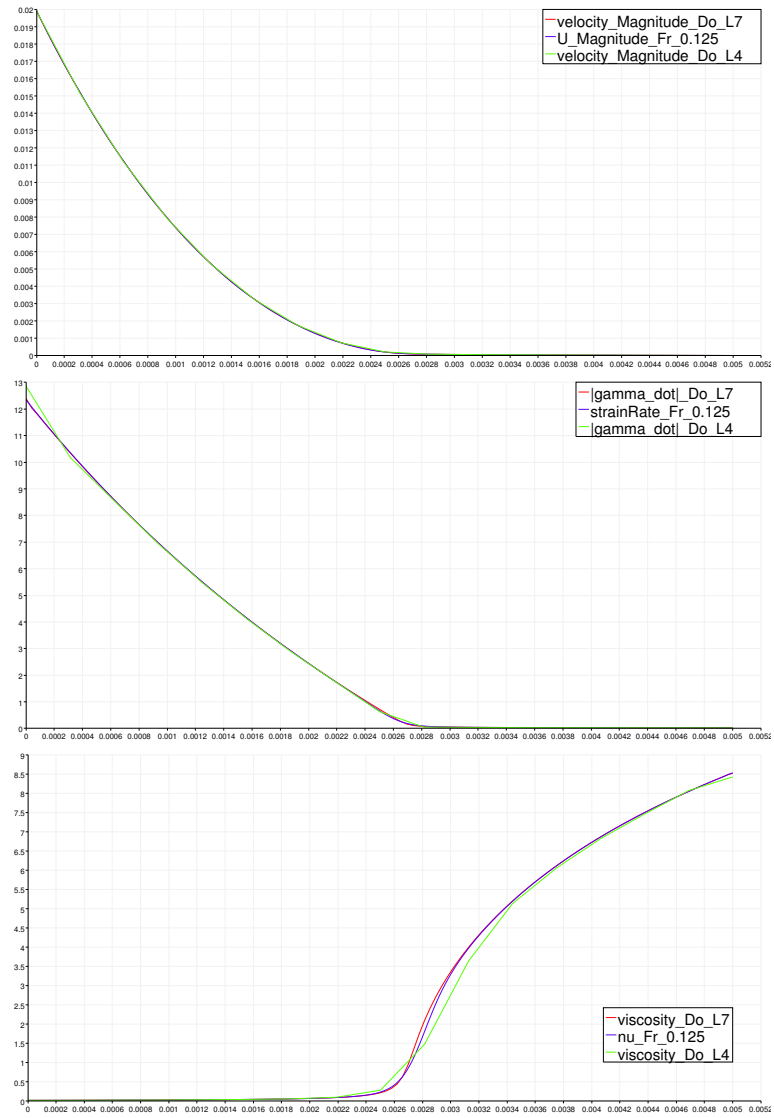


Figure 24: Normal scale

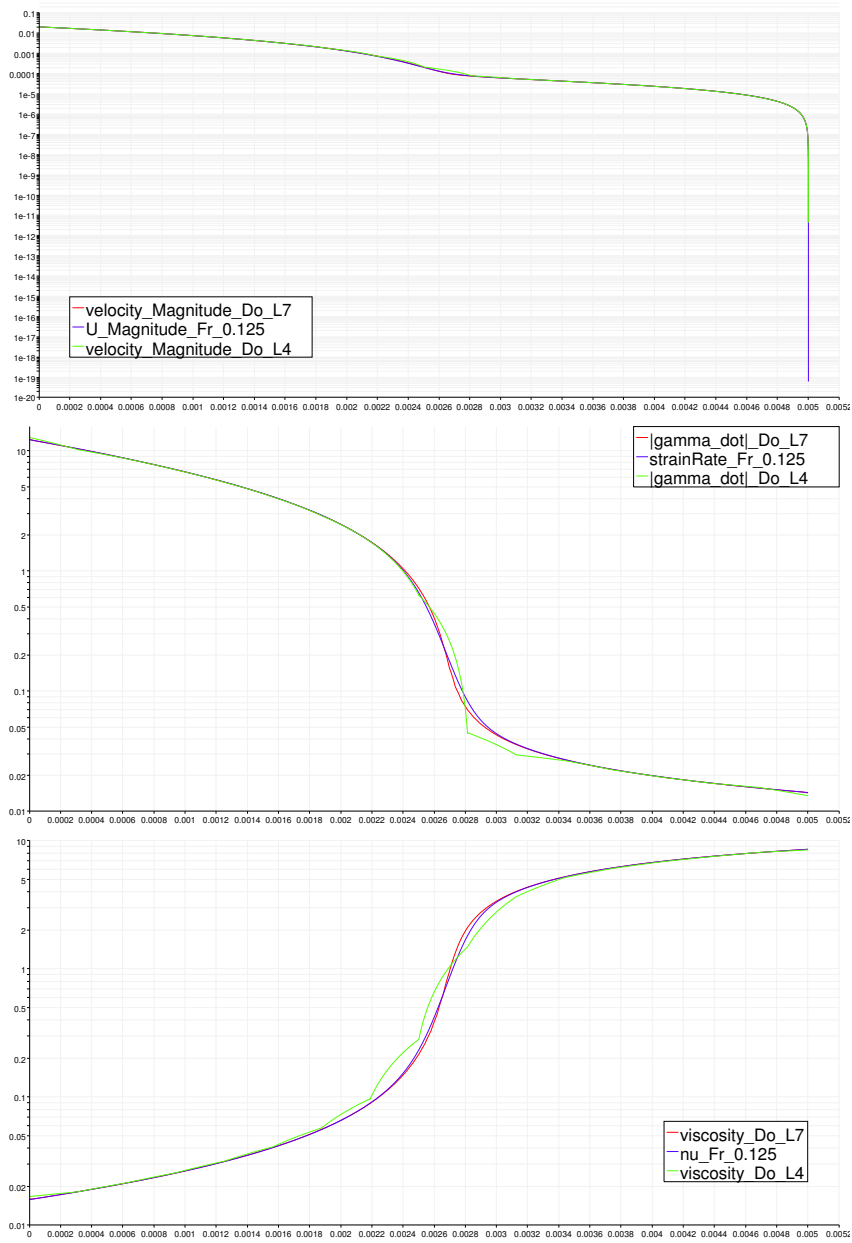


Figure 25: Log scale

We show the variation of the Dortmund level 4 and Freiberg 0.25 compared to Dortmund level 7 in Section 6.5.2 and the variation of the Dortmund level 4 and Freiberg 0.125 compared to Dortmund level 7 in Section 6.5.3. As the corresponding  $\xi$  values for  $|u|$  is minimum among the three physical quantities (Table 19), we can also visually see that the  $|u|$  profiles almost coincide with each other and similarly the variations of  $|\dot{\gamma}|$  profiles are also negligible. Additionally the profiles have been also presented in log scales to capture the small values on the right half of the domain. However as the  $\xi$  values for  $\eta$  is moderately high, we can see the corresponding variations. Moreover as the variations are of similar order, we conclude that Dortmund level 4 results have similar accuracy with respect to Freiberg 0.25 or 0.125 results.

## 6.6 Choice of the Regularization parameter

### 6.6.1 Initial Study

We calculate  $\xi$  consecutive pairwise from the set of  $\epsilon = 1E - 1, 1E - 2, 1E - 3$  and  $1E - 4$  on the same level, where  $L_i$  and  $L_j$  are the the line plots on the same level with different  $\epsilon = 1E - i$  and  $1E - j$ . As  $\epsilon$  of one order of magnitude has an effect of the same order in the viscosity, we can not do a comparative study on it and so we present the results only for the shear rate and velocity magnitude in the following table.

		12	13	14	15	16
$\xi_{21}$	$ u $	5.96	6.17	6.44	6.49	6.49
	$ \dot{\gamma} $	4.56	4.09	4.33	4.39	4.4
$\xi_{32}$	$ u $	0.64	0.58	0.67	0.69	0.69
	$ \dot{\gamma} $	0.46	0.31	0.45	0.5	0.52
$\xi_{43}$	$ u $	0.0405	0.0542	0.0659	0.0687	0.0697
	$ \dot{\gamma} $	0.0235	0.0342	0.0418	0.0502	0.0527

**Table 20:**  $\xi$  comparison in %

We can see in Table 20 that the values for  $\xi_{21}$  are between 4 – 7% and hence we say that the choice of  $\epsilon = 1E - 1$  is not good enough compared to  $\epsilon = 1E - 2$ . Consequently as  $\xi_{32}$  are even less than 1% and the values for  $\xi_{43}$  is almost negligible, we claim that the choice of  $\epsilon = 1E - 2$  is already good enough compared to  $\epsilon = 1E - 3$  keeping in mind the extra computation cost for the lower  $\epsilon$ .

### 6.6.2 Detailed Study

		$\epsilon_1 = 1E - 1$				$\epsilon_2 = 1E - 2$				$\epsilon_3 = 1E - 3$			
		Do-12	Do-13	Do-14	Do-15	Do-12	Do-13	Do-14	Do-15	Do-12	Do-13	Do-14	Do-15
L6, $\epsilon_1$	$ u $	7.56	1.65	0.36	0.07	6.61	5.42	6.13	6.31	6.83	5.97	6.79	6.98
	$ \dot{\gamma} $	11.02	4.31	1.52	0.45	13.94	6.58	4.87	4.57	14.32	6.78	5.31	5.07
L6, $\epsilon_2$	$ u $	12.49	7.52	6.69	6.53	7.77	1.85	0.4	0.08	7.39	1.57	0.55	0.65
	$ \dot{\gamma} $	10.49	5.66	4.5	4.39	11.87	4.47	1.56	0.45	12.16	4.57	1.66	0.68
L6, $\epsilon_3$	$ u $	13.1	8.22	7.4	7.24	8.18	2.34	0.98	0.74	7.77	1.93	0.42	0.08
	$ \dot{\gamma} $	10.58	6	4.96	4.87	11.78	4.51	1.64	0.68	12.06	4.59	1.6	0.47

**Table 21:** Choice of  $\epsilon$

Here we take the result on Level 6 with different  $\epsilon$  as the reference solution and compare the  $\xi$  with the other sets of level and  $\epsilon$ . We fix  $\epsilon$  to be 3 different values, namely  $\epsilon_1 = 1E - 1$ ,  $\epsilon_2 = 1E - 2$  and  $\epsilon_3 = 1E - 3$ . If we take  $\epsilon_1$ , we can see in the first numerical column block that there is not much difference on Level 2 and the error is around 10% for the shear rate. Whereas the same error is around 5%, when we refine the mesh for one level and so we can say that if the tolerance limit is set to be 5 – 10%, the simulation can be done with  $\epsilon_1 = 1E - 1$  on the level 2 or 3. Subsequently if the tolerance limit is lowered to be 1% for more accuracy, then one can reduce the  $\epsilon$  to be  $\epsilon_2 = 1E - 2$  or  $\epsilon_3 = 1E - 3$  and simultaneously the mesh should be refined at least to the level 4. In addition we would like to point out that the combination of coarse mesh and small regularization parameter and the combination of refined mesh and large regularization parameter both result into considerably large error and therefore we conclude that the regularization parameter  $\epsilon$  should be chosen in accordance with the choice of the level.

### 6.6.3 Visual Analysis

Next we represent the visualization with different  $\epsilon$  on the coarsest (L2) and the finest (L6) levels and the representation is done in normal scale and additionally in log scale to demonstrate also the small scale variations.

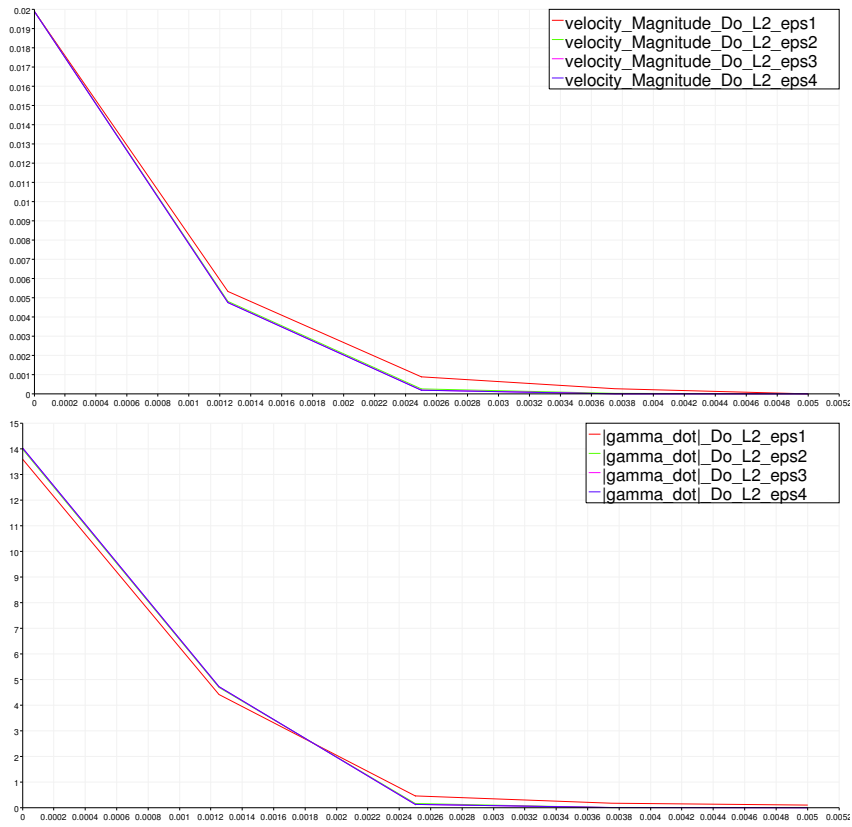


Figure 26: Normal scale on L2

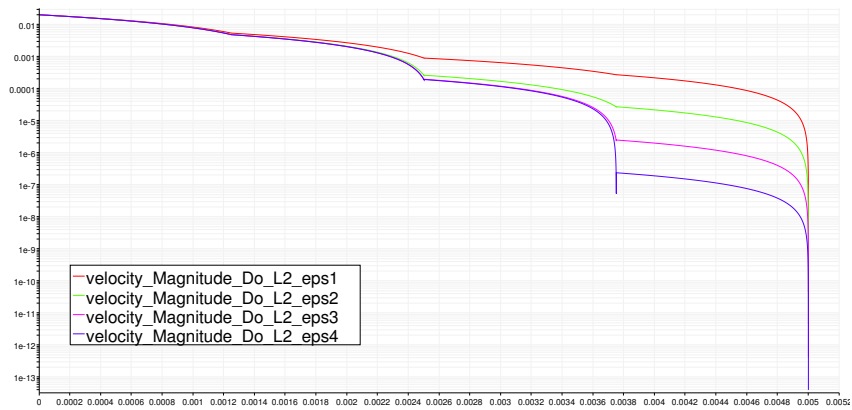


Figure 27: Log scale on L2

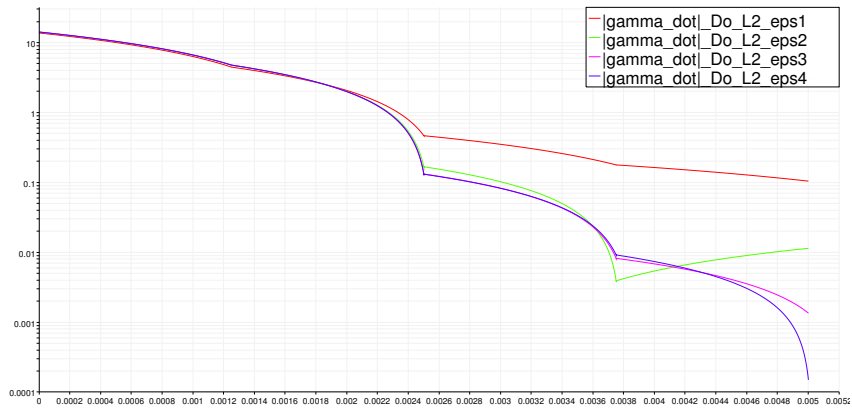


Figure 28: Log scale on L2

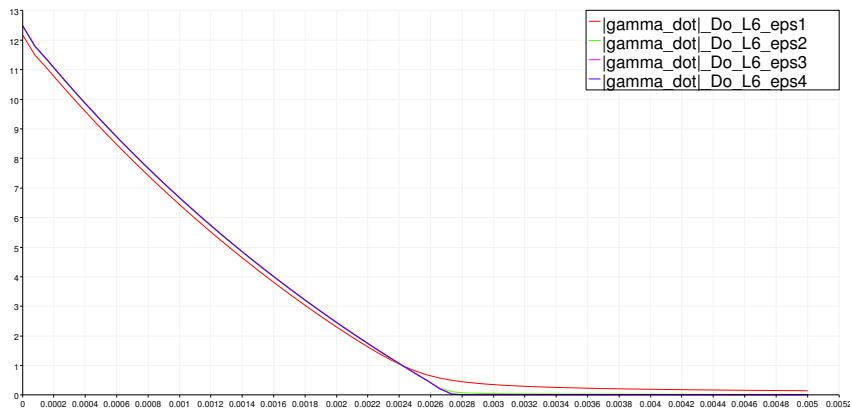
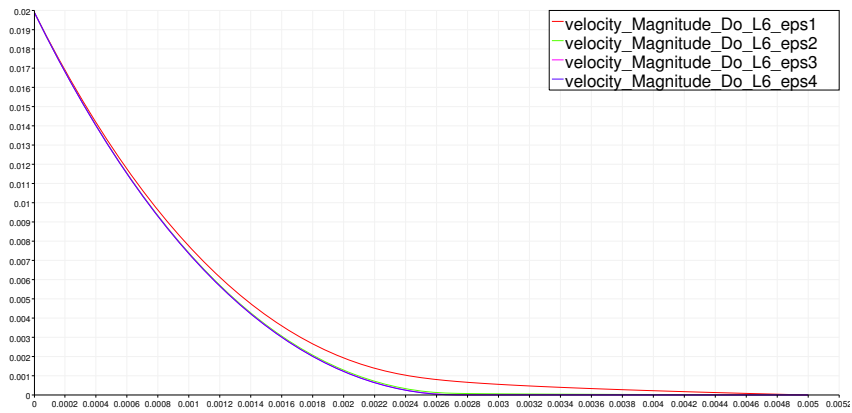
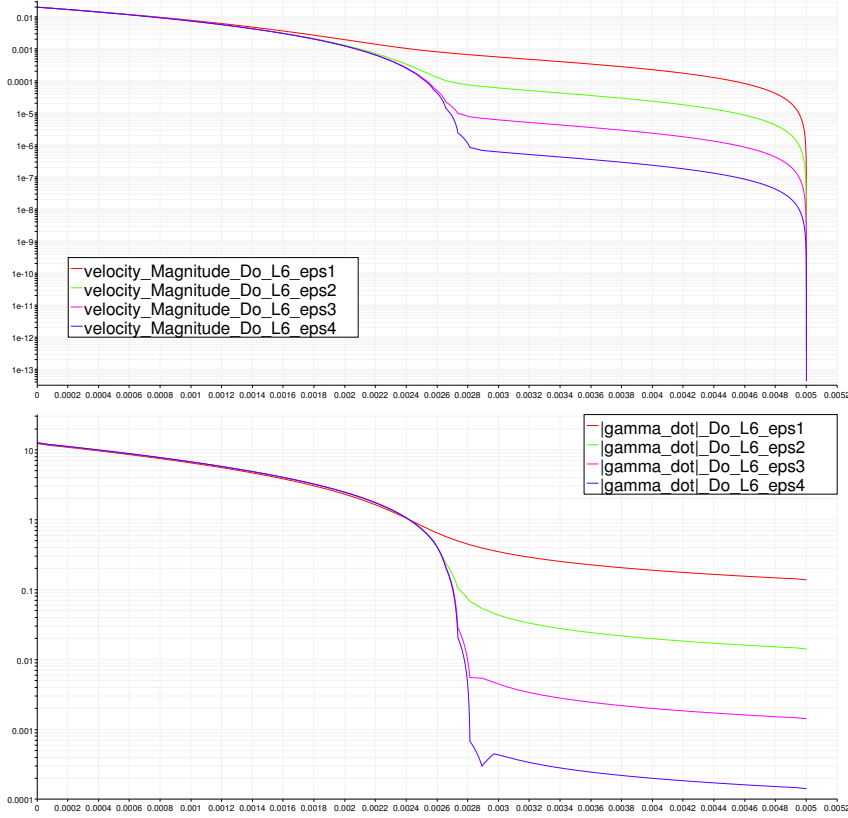


Figure 29: Normal scale on L6



**Figure 30:** Log scale on L6

We can see in Fig. 26-28 that the level 2 cutlines are discrete, while the level 6 cutlines in Fig. 29-30 are more continuous. Moreover the small  $\epsilon$  cutlines tend to cluster among themselves on the normal scale showing the saturation level of the solution. Now if we look closely on the log scale figures (Fig. 27 and 30), we can see that there is hardly any difference between  $\epsilon_1$  plots for  $|u|$  between level 2 and level 6 and so we can say that level 2 has enough resolution for  $\epsilon_1$ . However the level 2 cutline for  $\epsilon_4$  plots has 3 different steady interval (where the derivate is close zero or the cutline is almost parallel to the horizontal axis) and transitions between them is somewhat abrupt. Whereas the level 6 cutline for  $\epsilon_4$  plots has 2 different steady interval and transition between them is also smoother. Since a level 6 solution is obviously more accurate than a level 2 solution, we infer that level 2 lacks enough resolution to capture the detailed aspect of  $\epsilon_4$ . This similar feature is also present on the log scale plots for  $|\dot{\gamma}|$  (Fig. 28 and 30). Hence we can say in the similar way of Section 6.6.2 that a coarse mesh is good enough for large  $\epsilon$  and on the other hand a refined mesh is needed for a small  $\epsilon$  and so the regularization parameter  $\epsilon$  should be chosen in accordance with the choice of the level.



## 7 Summary and Outlook

### 1. Spatial discretization and solver aspects:

The conforming Stokes element  $Q2/P1$  is our candidate for the discretization method due to the involved biquadratic polynomials to a higher order of accuracy. A standard Umfpack method as typical iterative single grid solver with General Vanka preconditioning is applied, where the preconditioner is taken from the library developed in [28]. For this highly nonlinear problem coupling the pressure and velocity even in the viscous term we are applying the continuous Newton method to derive the corresponding continuous Jacobian operators which leads to a rate of convergence independent of mesh refinement. So we avoid the delicate task of choosing the step-length required for a divided difference approach. Then we propose an initial strategy based on the convergence radius, where we apply fixed point for the first few nonlinear iterations and switching to full Newton as soon as we reach some given tolerance. This approach shows that the strategy can be robust with respect to the starting guess. Next we implement a very primitive version of the Adaptive Newton solver, where the weighing parameter  $\delta_n$  is multiplied with a fixed value more (or less) than 1, depending on the value of improvement  $Q_n$  of the residual being less (or more) than 1. Then we work with a piecewise (almost) continuous function, where the incremental factor  $f(Q_n)$  takes varying values over the interval  $Q_n \in (0, \infty)$ . Finally we come up with the final version of our Adaptive Newton method, where  $f(Q_n)$  is smooth and continuous.

2. **Multigrid aspect and improvement:** Initially the Adaptive Newton solver is implemented for the direct solver Umfpack. However the results show that our adaptive strategy also fits in with the multigrid solver and consequently it helps us improving the CPU time for the simulation on the finer meshes. Also as we have mentioned earlier that the choice of  $f(Q_n)$  is experimental, some choices might not be suited for a particular set of problems and hence the characteristic function  $f(x)$  should be modified or improved in certain cases. A couple of examples for such cases will be discussed in section 8.

3. **Other aspects of  $f(Q_n)$ :** Currently our characteristic function  $f(Q_n)$  is used predominantly for nonlinear iterations and in the similar way, a similar set of  $f(Q_n)$  can also be constructed for linear iterations. Moreover the same strategy can be applied for each of the compressible and non-stationary version of the Navier Stokes equation.

4. **Inclusion of temperature in the viscosity function:** There are some kind of fluids, whose viscosity is a function of the temperature  $\theta$ , i.e,  $\eta = \eta(\theta)$ . Our strategy can also be applied to such non-Newtonian fluid. Some example of such fluids are:

$$\begin{aligned} \eta(\theta) &= \eta_0 \exp \frac{E}{R\theta}, && \text{for Arrhenius model} \\ &= \eta_0 \exp \frac{-C_1(\theta - \theta_r)}{C_2 + \theta - \theta_r}, && \text{for Williams-Landel-Ferry model,} \end{aligned}$$

where  $E$  is the activation energy,  $R$  is the universal gas constant in the first model and  $\eta_0$ ,  $C_1$ ,  $C_2$  and  $T_r$  are empiric parameters.

5. **Conclusion:**

We conclude that our finite element methods together with special material laws can be useful tools for the numerical simulation of incompressible granular powder. Although our computer simulation is only two-dimensional, still it is able to capture the complete structure of the flow, i.e. the velocity, the shear rate as well as the viscosity.

The idea of a continuum model for granular materials is of great importance in the food, soil mechanics, and packaging industries. Within these models, some of the characteristics of the flow was successfully captured. Since the simulations of processes, for instance Couette flow, are of extreme importance for these materials, it is indispensable to incorporate the various surrounding boundaries to derive equations of motion for multi-phase flows. The instability for incompressible powder flow could be regularized by allowing for the changes in density of the media ([18], [12]) with an extra coupling of the scalar reaction-convection-diffusion equation for the density. The Schaeffer model was proposed for the static state of the dry granular materials, whereas Tardos and Poliquen models refer to the intermediate regime and subsequently the study can be further extended to the wet granular materials. Moreover the Adaptive Newton strategy can also be used for compressible granular and powder flow models. The derived techniques in this thesis can successfully be adapted to such coupled problems including further physical models, namely viscoelastic, hypoplastic and multiphase flow since at least with respect to an algorithmic view the general structure of this coupling is similar.





## 8 Appendix

### 8.1 Improvement of $f(Q_n)$

As we have mentioned earlier that the choice of the characteristic function  $f(Q_n)$  is experimental, here we will discuss this aspect in details. We present the limitation of a particular choice of  $f(Q_n)$  and discuss the improvements can be made for that. Currently we take the 2D Couette flow as the geometry, use the mathematical formulation prescribed in section 6.2 and present 3 different versions of the characteristic function  $f(Q_n)$  for the adaptivity of  $\delta_n$  as:

$$f_1(Q_n) = 0.2 + \frac{4}{0.7 + \exp(1.5Q_n)}, \quad (8.16)$$

$$f_2(Q_n) = 0.2 + \frac{19.1957}{4.0515 + \exp(3.008Q_n)}, \quad (8.17)$$

$$f_3(Q_n) = 0.2 + \frac{17.694}{8.83 + \exp(2.608Q_n)}. \quad (8.18)$$

#### 8.1.1 Stagnation

Theoretically speaking,  $f(x)$  should be greater than 1 for  $x < 1$  and less than 1 for  $x > 1$  and intuitively an interpolating polynomial can be initial guess. However as a polynomial goes to  $\infty$  or  $-\infty$  for a large value of  $x$ , it makes a polynomial (e.g.  $f(x) = 2 - x$ ) a bad choice and we have to work with some adjustment. So we take  $f_1(x)$  as the working function for the 2D Couette flow geometry and the mathematical formulation prescribed in section 6.2 with the modification of  $\epsilon = 0.001$ . We try to solve the problem on Level 2 and the convergence statistics shows that  $f_1(Q_n = 0.987) = 0.985$  for few iterations, which means that  $\delta_n$  is being decreased even if the solver is going in the right direction. As mentioned earlier, this particular misbehavior can happen due to the imperfect construction of the characteristic function  $f(x)$ , which does not behave exactly like a linear and monotonically decreasing function  $f(x) = 2 - x$  around  $x = 1$ .

Addressing this particular aspect into more details, the improvement  $Q_n$  for this particular problem remains in the interval (0.973, 0.995) from the 25<sup>th</sup> iteration, which results in the confinement of the incremental factor  $f(Q_n)$  in the interval (0.99, 0.977) for the rest of the iterations (Fig. 31). Hence the solver never reaches the Full Newton state and it takes 918 steps to satisfy the convergence criteria (Fig. 32). We conclude that The choice of  $f_1(x)$  is not well suited for the problem and the solver stagnates.

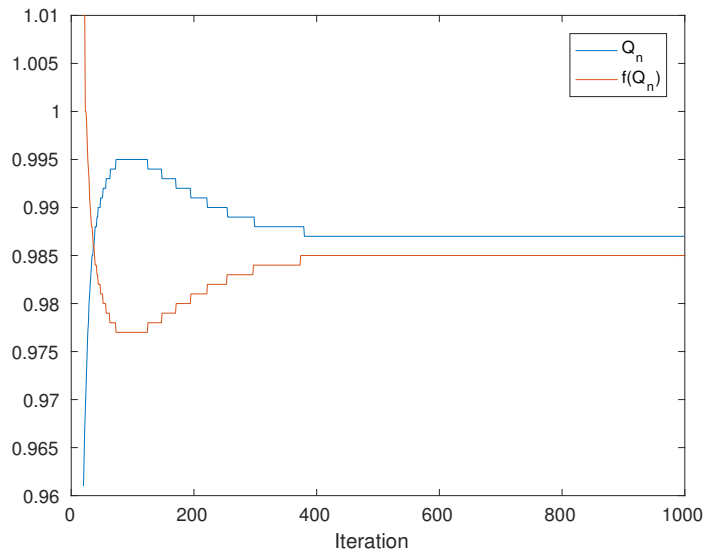


**Figure 31:** Reason for the Stagnation for the strategy  $f_1(Q_n)$

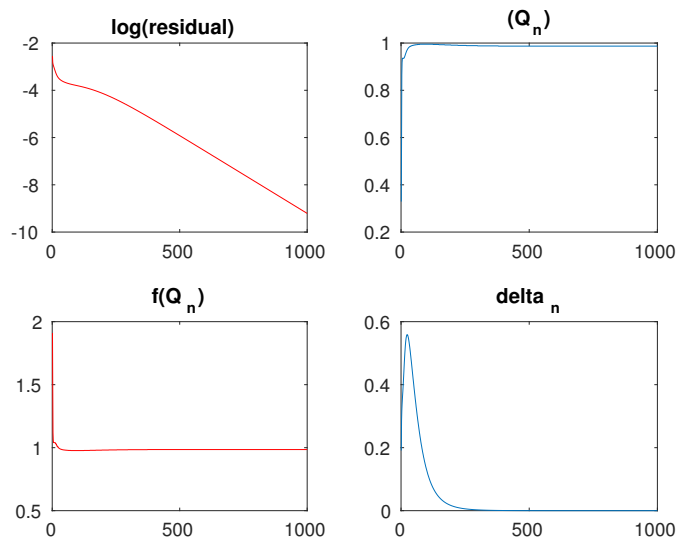


**Figure 32:** Convergence Statistics for the strategy  $f_1(Q_n)$

### 8.1.2 Infinite Loop

Next we change our characteristic function to  $f_2(x)$ . In order to decide the parameter values, we use the restrictions  $f(0) = 4, f(0.9) = 1.2, f(1) = 0.99$  and  $f(\infty) = 0.2$  and express the function as stated in Eq. 8.17. Now we try to solve the same 2D Couette flow geometry with the mathematical formulation prescribed in section 6.2 on Level 3.

However we face a different situation with this setting. It does not show any stagnation, but the set of residual  $Res_n$ , the improvement  $Q_n$  and the incremental factor  $f(Q_n)$  happen in a rhythmic order of 3 steps (Fig. 33). It means that at a certain step, there is a particular residual having a particular improvement from the previous step resulting in a particular incremental factor. Because of this incremental factor, the residual changes to a new value resulting in a new improvement and subsequently a new incremental factor. We can see that the set of  $Res_n, Q_n$  and  $f(Q_n)$  are related to their previous values and for this particular problem, the residual takes the identical same value at every third step initiating a cycle. Subsequently it results in an infinite loop and the solver is unable to converge (Fig. 34).

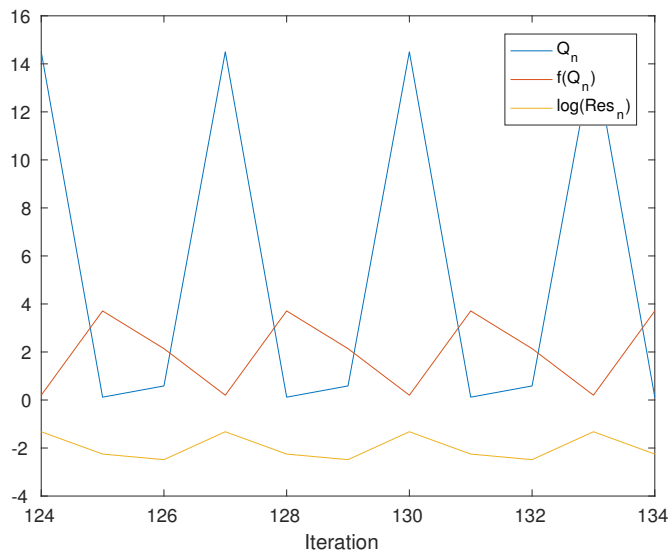


**Figure 33:** Rhythmic behavior of  $\delta_n$  for the strategy  $f_2(Q_n)$

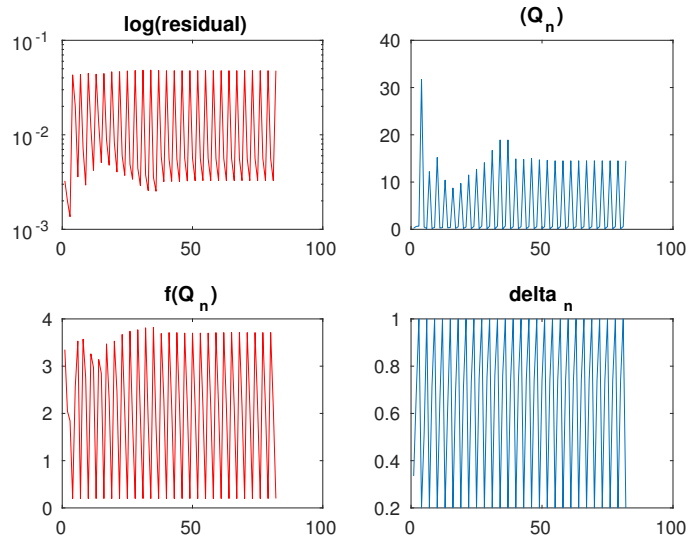


**Figure 34:** Convergence Statistics for the strategy  $f_2(Q_n)$

### 8.1.3 Conclusion

Finally we use the restrictions  $f(0) = 2$ ,  $f(0.6) = 1.5$ ,  $f(1) = 0.99$  and  $f(\infty) = 0.2$  to construct  $f_3(Q_n)$  as shown in Eq. 8.18. Till now we are successful to get convergent results for all the combinations for the levels and  $\epsilon$  for the (modified) Poliquen model in the 2D Couette flow geometry using  $f_3(Q_n)$  and hence we would like to conclude that  $f_3(Q_n)$  is the best choice among the used characteristic functions.

## 8.2 Boundary conditions

The boundary conditions in any incompressible fluid simulation are expressed either in terms of the fluid velocity or the pressure at the boundary, but generally both of them cannot be used at the same boundary since the velocities are influenced by the pressure gradient [25]. For the Navier-Stokes equations with Dirichlet velocity data, the pressure is unique up to a constant which however can be chosen arbitrarily. In contrast, for the flow of the generalized Navier-Stokes equations with pressure dependent viscosity, the choice of fixing the pressure cannot be done by random choice.

### 8.2.1 Wall boundary conditions

The fundamental assumption in fluid mechanics for flow past solids is a 'no-slip' boundary condition, which means that the tangential component of the fluid velocity equals of the solid at the surface. This well-accepted 'no-slip' boundary condition may not be suitable for highly sheared flow, but the error due to the 'no-slip' assumption is relatively small in big systems or if we are more interested in the flow far away from the wall. An alternative and more suitable condition is to apply slip with friction parameter  $\beta$ :

$$u \cdot t + \beta^{-1} n \cdot (2\eta(|\dot{\gamma}|, p)D(u) - pI) \cdot t = 0 \quad \text{on } \Gamma_{wall},$$

where  $n$  and  $t$  are the normal and tangential unit vectors. Moreover, the closing of the equations is required, because the related Dirichlet problem of Navier-Stokes equations is well known to possess no unique pressure solution due to the constraint  $\text{div } u = 0$ . The uniqueness of the solution is assured by fixing the pressure with the choice of mean pressure to be zero which however cannot be taken for the flow with pressure dependent viscosity, namely the Poliquen model, since it leads to negative values of the pressure in some parts of the computational domain. The first remedy is to make the choice of mean pressure positive to assure a positive pressure in all regions of the computational domain. However, the question arises of the physical meaning of any choice for the mean pressure to get the closure of the equations with Dirichlet boundary condition since the mean pressure is part of the viscosity and therefore it significantly influences the global flow behavior.

### 8.2.2 Outflow boundary conditions

Numerical simulations of flow problems usually require the flow out of one or more boundary parts of the computational domain. At such 'outflow' boundaries, there arises the question of what constitutes a good boundary condition. The simplest and most commonly used outflow

condition is that of a 'natural' boundary, see [25] for an overview:

$$2\eta(|\dot{\gamma}|, p)n \cdot D(u) - pn = 0 \quad \text{on } \Gamma_{out} .$$

This boundary condition represents a smooth continuation of the flow through the boundary and occurs in the variational formulation of problem if one does not prescribe any boundary condition for the velocity at the outlet, known in the literature by the name 'natural' or 'do nothing' boundary condition as for the Flow around cylinder benchmark Fig. 15. It must be stressed that the 'do nothing' outflow boundary condition has no physical basis, rather it is a mathematical statement that may or may not provide the desired flow behavior. Particularly 'do nothing' boundary conditions have proven to lead to very satisfactory results in modeling parallel flows [26], but they must always be viewed with suspicion since they contain the hidden condition that the mean pressure is zero across the outflow boundary. In particular, the condition of mean pressure to be zero across the outflow leads to negative values of the pressure, which causes problems for the numerical simulation of flow with pressure dependent viscosity, namely the Poliquen model. As a natural remedy for this situation, one may consider a condition in which the mean pressure across the outflow coincides with the atmospheric pressure, that means  $p_{atm} > 0$ :

$$2\eta(|\dot{\gamma}|, p)n \cdot D(u) - pn = p_{atm}n \quad \text{on } \Gamma_{out} .$$

The above examples suggest that the ability to specify a pressure condition at one or more parts of the computational domain is an important aspect. This can be done in terms of *prescribed pressure drops* with corresponding variational formulations of very general type [25].





## References

- [1] P. Jop, Y. Forterre and O. Pouliquen . *Initiation of granular surface flows in a narrow channel*. Nature 441,727, 2007.
- [2] I. Aranson and L. Tsimring. *Continuum theory of partially fluidized granular flows*. Physical review edition, vol. 65, 061303, 2002.
- [3] M.K. Langroudi, S. Turek, A. Ouazzi and G.I. Tardos. *An investigation of frictional and collisional powder flows using a unified constitutive equation*. Powder Technology 197, 91-101, 2010.
- [4] G.I. Tardos. *A fluid mechanistic approach to slow, frictional flow of powders*. Powder Technology 92 61-74, 1996.
- [5] J. Sun and S. Sundaresan. *A constitutive model with microstructure evolution for flow of rate-independent granular materials*. J. Fluid Mech. vol. 682, pp. 590-616, 2011.
- [6] J. Sun and S. Sundaresan. *Radial hopper flow prediction using a constitutive model with microstructure evolution*. Powder Technology, submitted, 2013.
- [7] T. Weinhart, R. Hartkamp, A. R. Thornton and S. Luding. *Coarse-grained local and objective continuum description of 3D granular flows down an inclined surface*. University of Twente, 2013.
- [8] Ph. Marchal, N. Smirani and L. Choplin. *Rheology of dense-phase vibrated powders and molecular analogies* J. Rheol. 53(1), 1-29, 2008.
- [9] J.T. Jenkins and D. Berzi. *Kinetic theory applied to inclined flows*. Granular Matter, Volume 14, Issue 2, pp 79-84, 2012.
- [10] J.A. Dijksman and M. Hecke. *Granular Flows in Split-Bottom Geometries*. arXiv, 2010, 1003.5620v1, 2010.
- [11] H. Damanik, J. Hron, A. Ouazzi and S. Turek. *Monolithic Newton-multigrid solution techniques for incompressible nonlinear flow models*. International Journal for Numerical Methods in Fluids, Volume 71, Issue 2, pages 208–222, 2011.
- [12] A. Ouazzi, S. Turek and J. Hron. *Finite Element methods for the simulation of incompressible powder flow*. Communications in numerical methods in Engineering, 21:581-596, 2005.

- [13] P. Jop, Y. Forterre and O. Pouliquen. *A constitutive law for dense granular flows*. Nature 441, 727-730, 2006.
- [14] R.M. Nedderman. *Static and Kinematic of Granular Material*. Cambridge Uni. Press, Cambridge, New York, 1992.
- [15] F. Göncü. *Mechanics of Granular Materials: Constitutive Behavior and Pattern Transformation*. Enschede, May 2012.
- [16] P. Gremaud and J.V. Matthews. *On the Computation of Steady Hopper Flows: I, Stress Determination for Coulomb Materials*. Technical report, NCSU-CRSC Tech Report CRSC-TR99-35, 2001.
- [17] D.G. Schaeffer. *Instability in the evolution equation describing incompressible granular flow*. J. of Differential Equations, 66:19–50, 1987.
- [18] G.I.Tardos, S. McNamara, and I. Talu. *Slow and intermediate flow of a frictional bulk powder in the Couette geometry*. Powder Technology, 4686:1–17, 2002.
- [19] F. Lacombe, S. Zapperi and H.J. Herrmann. *Dilatancy and friction in sheared granular media*. Eur. Phys. J. E, 2:181–189, 1986.
- [20] D.G. Schaeffer. *Mathematical Issues in the continuum formulation of slow granular flow*. Springer, 1997.
- [21] A. Ouazzi. and S. Turek. *Numerical Methods and Simulation Techniques for Flow with Shear and Pressure dependent Viscosity*. In Numerical Mathematics and Advanced Applications. Springer, 2003. ENUMATH2003.
- [22] K Bathe. *Proceedings First MIT Conference on Computational Fluid and Solid Mechanics Vol. 2*. J. Editor. Computational Fluid and Solid Mechanics. Elsevier, 2001.
- [23] D. Boffi and L. Gastaldi. *On the quadrilateral Q2-P1 element for the Stokes problem*. Int. J. Numer. Meth. Fluids, 39:1001–1011, 2002.
- [24] S. Turek. and J. Hron. *A monolithic FEM solver for an ALE formulation of fluid–structure interaction with configuration for numerical benchmarking*. In P. Wesseling, E. Onate, and J. Periaux, editors, Books of Abstracts European Conference on Computational Fluid Dynamics, page 176. nm, 2006. Eccomas CFD 2006.

- [25] J.P. Heywood, R. Rannacher and S. Turek. *Artificial boundaries and flux and pressure conditions for incompressible Navier Stokes equations*. Int. J. Numer. Math. Fluids, 22:325–352, 1996.
- [26] S. Turek. *Efficient solvers for incompressible flow problems: An algorithmic and computational approach*. Springer, 1999.
- [27] S. Mandal, A. Ouazzi and S. Turek. *Modified Newton solver for yield stress fluids*, Proceedings of ENUMATH 2015, the 11th European Conference on Numerical Mathematics and Advanced Applications, Springer, 2016.
- [28] R. Bramley and X Wang. *SPLIB: A library of iterative methods for sparse linear systems*. Department of Computer Science, Indiana University, Bloomington, IN, 1997. <http://www.cs.indiana.edu/ftp/bramley/splib.tar.gz>.
- [29] A. Ouazzi. *Finite element simulation of nonlinear fluids with application to granular material and powder*. LS III, TU Dortmund, 2005.
- [30] H. Damanik. *FEM Simulation of Non-isothermal Viscoelastic Fluids*. LS III, TU Dortmund, 2011.
- [31] M. El-Borhamy. *Numerical Simulation For Viscoplastic Fluids Via Finite Element Methods*. LS III, TU Dortmund, 2012.
- [32] S. Turek and FEATFLOW group. *DFG Flow around cylinder benchmark 2D-1, laminar case (Re=20)*. Url: <http://www.featflow.de/en/benchmarks/cfdbenchmarking.html>, TU Dortmund, 2016.
- [33] S. Turek et al. *FEATFLOW - Finite element software for the incompressible Navier-Stokes equations*. User manual, TU Dortmund, 1999.
- [34] L.C. Evans. *Partial Differential Equations*. American Mathematical Society, 2010.
- [35] D. Braess. *Finite Elements: Theory, Fast Solvers, and Applications in Solid Mechanics*. Cambridge University Press, 2007.